

FINAL REPORT
ON EXTENSION TO
STUDY OF HEAT SHIELDING REQUIREMENTS FOR
MANNED MARS LANDING AND RETURN MISSIONS



N66 32717

FACILITY FORM 602

(ACCESSION NUMBER)

115

(PAGES)

CR-68147

(NASA CR OR TMX OR AD NUMBER)

(THRU)

1

(CODE)

33

(CATEGORY)

GPO PRICE \$ _____

CFSTI PRICE(S) \$ _____

Hard copy (HC) 3.00Microfiche (MF) 75

ff 653 July 65

*E

LOCKHEED MISSILES & SPACE COMPANY

A GROUP DIVISION OF LOCKHEED AIRCRAFT CORPORATION
SUNNYVALE, CALIFORNIA

STUDY OF HEAT SHIELDING REQUIREMENTS FOR
MANNED MARS LANDING AND RETURN MISSIONS

by

L. W. Woodruff

W. D. Coleman

L. F. Hearne

September 1965

Work Carried Out Under Modification No. 2 to Contract NAS 2-1798

APPROVED: *L F Hearne*
L. F. Hearne, Head
Superorbital Entry

APPROVED: *D. M. Tellep*
D. M. Tellep, Manager
Launch & Entry
Thermodynamics

FOREWARD

This document comprises the Final Report on a study performed by Lockheed Missiles and Space Co. for the National Aeronautics and Space Administration under Modification No. 2 to Contract NAS 2-1798. The work was performed during the period from 25 February 1965 to 8 June 1965 under the direction of the Ames Research Center, Moffett Field, California.

The principal contributors to the study and their respective areas of investigation were:

L. F. Hearne	Study Leader
W. D. Coleman	Heat Shield Performance
L. W. Gallagher	Computational Methods
W. E. McFadden	Flight Mechanics
L. W. Woodruff	Aerothermal Environment and Shielding Requirements

PRECEDING PAGE BLANK NOT FILMED.

SUMMARY

N66-3 2917

A parametric description of heat shielding requirements for entry into the Earth atmosphere at hyperbolic speed is presented for two lifting vehicles of the biconic configuration class. In addition, detailed predictions of shield material response are provided for several prescribed test environments.

The preceding phases of this study resulted in development of analytical techniques suitable for determination of the hyperbolic entry environment and prediction of shield material behaviour. These basic methods are reviewed and recent refinements are described in the current report. Flight mechanics, fluid dynamics, and fundamental thermodynamic and transport properties data are discussed together with heat transfer and material performance analyses.

Approximately 50 separate cases were studied to obtain parametric results for heat shield weights over the entry velocity range from 36,000 ft/sec to 65,000 ft/sec. Shielding requirements are greatest and relatively insensitive to entry velocity in the overshoot entry mode. Significant weight penalty is associated with the use of higher lift to increase entry-corridor width. As compared with vehicle geometries previously considered, the slender biconic configurations require appreciably greater shielding than do blunter configurations. The environmental uncertainty most affecting the predicted shielding requirements is boundary layer transition. Radiative heat transfer is unimportant even at the highest velocities considered. The extent of blunting of the initially sharp noses during entry is small and should cause no adverse thermal affect.

Author

PRECEDING PAGE BLANK NOT FILMED.

CONTENTS

Section	Page
FOREWORD	iii
SUMMARY	v
ILLUSTRATIONS	ix
TABLES	xi
1 INTRODUCTION	1-1
1.1 Study Objectives	1-1
1.2 Technical Approach	1-2
1.3 Plan of Report	1-3
2 MATERIALS PERFORMANCE	2-1
2.1 Nylon Phenolic Ablation Phenomena	2-1
2.1.1 Theoretical Performance Model	2-1
2.1.2 Performance Computation Techniques	2-6
2.2 Material Response Predictions	2-8
2.3 Comparison of Prediction With Data	2-14
2.4 Summary	2-16
References	2-18
Notation	2-19
3 HEAT SHIELDING REQUIREMENTS	3-1
3.1 Vehicle Performance	3-1
3.1.1 Vehicle Description	3-1
3.1.2 Entry Flight Mechanics	3-2
3.2 Aerothermal Environment	3-3
3.2.1 Shock-Layer Flow	3-4
3.2.2 Radiative Heat Transfer	3-7
3.2.3 Convective Heat Transfer	3-8
3.3 Shield Requirements Evaluation	3-16
3.3.1 General Approach	3-17
3.3.2 Results	3-20

~~PROCEEDING FROM THE~~

Section	Page
3.4 Nose Blunting Evaluation	3-25
3.4.1 Aerothermal Environment	3-26
3.4.2 Material Thermal Response	3-28
3.4.3 Extent of Nose Blunting	3-29
3.4.4 Influence of Nose Blunting	3-32
References	3-34
Notation	3-36
Appendix 3A, Comparison of Methods for Evaluating Convective Heat Transfer	3-39
4 CONCLUSIONS AND RECOMMENDATIONS	4-1
4.1 Conclusions	4-1
4.2 Recommendations	4-4

ILLUSTRATIONS

Figure		Page
2-1	Equilibrium Composition of the Gaseous Pyrolysis Products of Nylon Phenolic	2-27
2-2	Gas Enthalpy of the Pyrolysis Products of Nylon Phenolic	2-28
2-3	Evaluation of Surface Reaction Chemistry on Quasi-Steady Mass Transfer	2-29
2-4	Nylon Phenolic Thermophysical Properties	2-30
2-5	Nylon Phenolic Surface Temperature Histories	2-31
2-6	Nylon Phenolic Ablation History	2-32
2-7	Nylon Phenolic Internal Temperature Response, Case I	2-33
2-8	Nylon Phenolic Internal Temperature Response, Case II	2-34
2-9	Nylon Phenolic Internal Temperature Response, Case III	2-35
3-1	Vehicle Characteristics	3-46
3-2	Typical Entry Trajectory	3-47
3-3	Pullout Characteristics	3-48
3-4	Cold Wall Convective Heat Flux History	3-49
3-5	Cold Wall Convective Heat Flux History	3-50
3-6	Location of Boundary Layer Transition Point	3-51
3-7	Influence of Cone Angle on Radiation at Time of Pullout	3-52
3-8	Material Degradation History	3-53
3-9	Material Degradation History	3-54
3-10	Heat Shield Thickness Distribution	3-55
3-11	Heat Shield Thickness Distribution	3-56
3-12	Forebody Heat Shielding Requirements, $R_{e_c} = 5 \times 10^6$	3-57
3-13	Forebody Heat Shielding Requirements, $R_{e_c} = 1 \times 10^6$	3-58

Figure		Page
3-14	Forebody Heat Shielding Requirements, $R_{e_c} = 2 \times 10^5$	3-59
3-15	Influence of Transition Uncertainty on Forebody Heat Shielding Requirements	3-60
3-16	Influence of Critical Reynolds Number on Forebody Heat Shielding Requirements	3-61
3-17	Comparison of Shielding Requirements for Several Entry Vehicle Configurations	3-62
3-18	Stagnation Point Heating History	3-63
3-19	Nose Radius History	3-64
3-20	Influence of Entry Velocity on the Nose Bluntness of a 28.5 deg Cone	3-65
3-21	Influence of Entry Velocity on the Nose Bluntness of a 26 deg Cone	3-66
3-22	Influence of Nose Bluntness on Radiation to a Conical Surface	3-67
3-23	Laminar Heat Transfer Distribution Factor, 24.3 deg Cone Angle	3-68
3-24	Turbulent Heat Transfer Distribution Factor, 24.3 deg Cone Angle	3-69
3-25	Laminar Heat Transfer to Sharp Cones	3-70
3-26	Average Turbulent Stanton Number for Sharp Cones	3-71

TABLES

Table		Page
2.1	Nylon Phenolic Thermophysical and Thermochemical Properties	2-21
2.2	Description of Nylon Phenolic Environmental Test Conditions	2-22
2.3	Summary of Nylon Phenolic Response Predictions	2-23
2.4	Evaluation of Surface Reaction Chemistry on Quasi-Steady Ablation Performance	2-24
2.5	Experimental Results of Ablation Tests on High Density Nylon Phenolic	2-25
2.6	Comparison of Experimental Data and Theoretical Predictions	2-26
3.1	Heat Shield Weight Requirements Summary	3-43

Section 1 INTRODUCTION

A Mars trip, which may be an early objective of a manned planetary exploration program, may involve hyperbolic approach speed upon Earth return. Atmospheric braking appears to be an attractive means of accomplishing the Earth landing. However, entry at the anticipated approach velocities will subject vehicles to extreme thermal environments. The associated heat shielding requirements will be of major importance in selecting an optimum mission course.

1.1 STUDY OBJECTIVES

The purposes of this study are, first, to define the thermal protection required for entering the Earth atmosphere at hyperbolic speed and, second, to further qualify a theoretical model for the performance of charring heat shield materials. The results are expected to aid in the evaluation of independently derived data, to enable identification of problems for future research, and to provide a broader basis for directing design optimization studies.

The scope of the study and guidelines for its conduct were established by NASA-Ames. Two vehicles of fixed weight and volume, both being members of the biconic configuration class, are examined in evaluation of heat shielding requirements. High density nylon phenolic is the heat shield material studied. Entry velocities ranging from 36,000 ft/sec to 65,000 ft/sec are considered. The influence of entry corridor position is determined with a 10g maximum deceleration constraint on the trajectory. Trim altitudes are fixed for constant L/D with roll modulation being employed to achieve trajectory control. The extent and influence of nose blunting during re-entry is determined, and the effects of uncertainty in the boundary layer transition criterion are examined quantitatively.

1.2 TECHNICAL APPROACH

The current work was preceded by a comprehensive study of heat shielding requirements for a variety of possible vehicle configurations. The results are reported in Reference 1.1. In that study, a major portion of the effort was devoted to the formulation of analysis procedures, computation of basic data, and evaluation of uncertainties. The resulting developments have been utilized extensively in the present effort. These developments included generation of high temperature thermodynamic properties for air and selection of an emissivity model from the several disparate sets of data. A number of alternate methods of evaluating shock layer radiation accounting for the energy loss effect were formulated. Techniques for describing the effects of the mass transpiration, boundary layer transition, and shock-curvature-induced vorticity phenomena on convective heat transfer were developed. A theoretical model for predicting the thermophysical behaviour of heat shielding materials was extended for application in the hyperbolic entry situation.

In the current study, molecular transport properties of air have been reviewed and an improved model selected. A first-order means of accounting for radiative decay effects on convection was formulated and mass transpiration effects have been re-examined to refine heat transfer predictions.

An attempt has been made to place the proper emphasis on all aspects of the problem and to employ the most rigorous techniques possible within the scope of the study. All major computations were therefore coded for digital computer solution and an efficient information flow process was developed. In order to correctly establish the effects of the parameters and uncertainties, point analysis procedures were utilized. In particular, detailed time histories of the environment and shield response were computed in each case at a number of body stations sufficient to permit accurate evaluation of total shield weight. A schedule of cases was selected to define shield weights over the complete entry velocity range of interest for both overshoot and undershoot trajectories.

1.3 PLAN OF REPORT

The major results of the study are contained in the subsequent sections under the following main headings

- o Materials Performance
- o Heat Shielding Requirements

The first of these reviews the theory utilized to describe the behaviour of the heat shielding material and presents predicted performance of test samples in prescribed environments. Procedures for description of the aerothermal environment are given together with end results for heat shield weight in the second. Study conclusions and recommendations are presented in a final section.

REFERENCES

- 1.1 "Study of Heat Shielding Requirements for Manned Mars Landing and Return Missions", Report No. 4-74-64-1, Lockheed Missiles and Space Co., December 1964.

Section 2.0

MATERIALS PERFORMANCE

A theoretical performance model for charring organics which rigorously accounts for the various significant energy transfer mechanisms was derived by Kratsch, Hearne, and McChesney in Reference 2.1. In addition, the reference contains rate constants, and thermophysical and thermochemical data required in implementation of the model for nylon phenolic. The results of this study have been applied in the current work to obtain material response predictions.

In this section, the adopted ablation theory is briefly outlined. Computer codes used in the study are described together with their respective assumptions and approximations. The ablation model is applied to describe material response of nylon phenolic when subjected to a series of specified environmental conditions. A major limit assumption in the theoretical performance model is then replaced with the opposing limit; the resulting effects of material performance is demonstrated. Finally, predictions are compared with data.

2.1 NYLON-PHENOLIC ABLATION PHENOMENA

2.1.1 Theoretical Performance Model

At elevated temperatures (in the range from about 1000 to 1500°F), nylon-phenolic virgin polymers pyrolyze in a reaction layer fragmenting into high-molecular-weight gaseous products that leave a solid carbon residue. The carbon char supports high surface temperatures and the pyrolysis gases, during transit through the char to the surface, absorb heat by virtue of their temperature rise and associated chemical cracking. A continuous variation of the solid density occurs in the reaction layer as dictated by pyrolysis kinetics. If extreme temperatures are encountered, further reduction in density occurs near the surface. This reduction is the result of erosive reactions of the effluent gases with the carbon char and of direct sublimation of the char.

Upon exit at the surface, the transpiring gases perturb both the composition and temperature distribution of the boundary layer. Boundary layer edge (air) species react with the surface char causing recession of the surface and affecting heat transfer.

In order to describe the extent of material consumption quantitatively, a definition of the kinetics of the pyrolysis reaction is required. The thermophysical properties of the virgin plastic, the partially degraded plastic, and of the char material must be specified. A detailed description of the gaseous pyrolysis products must be obtained. Finally, the energy and mass transfer processes must be mathematically coupled.

The pyrolysis of nylon phenolic is a rate-limited process. The phenolic resin evolves complex hydrocarbon gases during decomposition and leaves a carbon residue. The nylon fabric decomposes almost completely to gases. The weight fraction of the composite remaining as carbon char after pyrolysis is 25 percent. Reference 2.1 indicates that the kinetics of the pyrolysis reaction are adequately represented by an Arrhenius-type law for the rate of density change. The three condensed-phase reactions of importance (phenolic undergoes two kinetic reactions in pyrolysis) are quantitatively described by analysis of the thermogravimetric data.

The pyrolysis gases are assumed to be in local thermal equilibrium with the char. Their composition is defined in Reference 2.1 by imposing the condition of chemical equilibrium. The elemental mass fractions of the gas are determined from the molecular structure of nylon ($C_6H_{11}O_1N_1$) and phenolic ($C_6H_6O_1$) and from the carbon-char weight fraction. Molecular species concentrations are determined by solution of the chemical equilibrium equations for a multicomponent mixture of perfect gases. A typical set of results is shown in Figure 2-1. The mass fraction of the pyrolysis products is given as a function of temperature at 1 atm. pressure. In the temperature range where the gas is formed by pyrolysis of the virgin material (1500 to 2000°F

approximately), the gas consists largely of high molecular weight hydrocarbons. Dehydrogenation of these gases occurs with increasing temperature. At extreme temperatures, cyano (CN), atomic hydrogen, and carbon vapor species appear.

The definition of the equilibrium composition of the pyrolysis gases enables computation of the thermodynamic properties of the mixture. The results of Reference 2.1 for the enthalpy of the gaseous pyrolysis products are shown in Figure 2-2. The enthalpy is initially low because of the predominance of species with negative heats of formation. The enthalpy increases rapidly with increasing temperature as a result of the endothermic composition changes of the mixture. It should be noted from the data of Figure 2-2 that the gas in transit through the char may absorb an amount of heat of the order of 10,000 BTU/lb.

To describe the surface erosion phenomena, Reference 2.1 follows Lees' treatment as presented in Reference 2.2. The extent of surface-combustion reactions and their effect on convective heat transfer are determined by assuming the Lewis-Semenov and Prandtl numbers to be unity. The further assumption is introduced that the pyrolysis gases act as an inert diluent upon injection into the boundary layer. Both reaction-rate limited and diffusion-controlled oxidation are treated. Nitrogen reactions with the char are determined by imposing a chemical equilibrium constraint on species concentrations (pyrolysis gases excluded) at the surface. The char erosion rate is then governed by the following relations,

Reaction-rate limited:

$$\frac{\dot{m}_c}{h} = \frac{3/4 [\tilde{K}_0 e^{-K_{O_2, w} (1 + \frac{\dot{m}_g}{h})}]}{1 + 3/4 K_{O_2, w}} \quad (2.1)$$

Diffusion controlled:

$$\frac{\dot{m}_c}{h} = \frac{3/4 \tilde{K}_{O,e} + 6/13 K_{CN}}{1 - \frac{1}{f_c} \frac{6/13 K_{CN}}{3/4 \tilde{K}_{O,e} + 6/13 K_{CN}}} \quad (2.2)$$

where f_c is the weight fraction of the residual char. The oxygen concentration at the wall in the reaction-rate-limited case is determined by imposing a kinetic equation describing reaction rates

$$\dot{m}_c = k_0 e^{-E/RT_w} (K_{O_2,w} P_c)^n \quad (2.3)$$

where the rate constants adopted are

$$\begin{aligned} k_0 &= 1.74 \times 10^5 \text{ LB}_m / \text{FT}^2 \text{ SEC} - \text{ATM}^{1/2} \\ E/R &= 36,200 \text{ }^\circ\text{R} \\ n &= 1/2 \end{aligned}$$

In the diffusion-limited case, reaction rates are sufficiently high so that molecular oxygen disappears at the wall. Surface temperatures may become sufficiently high so that nitrogen-carbon reaction occur. The nitrogen concentration at the wall is obtained from a chemical equilibrium calculation with char-gas mass transfer ratio a parameter.

The net heat transfer to the surface in both regimes is given by

$$-k \left(\frac{\partial T}{\partial y} \right)_{y=0} = h \left[H_0 - \left(1 + \frac{\dot{m}_g + \dot{m}_c}{h} \right) H_w + \frac{\dot{m}_g}{h} H_g + \frac{\dot{m}_c}{h} H_c \right] + q_r - \epsilon \sigma T_w^4 \quad (2.4)$$

where

$$H_w = \sum_j K_{j,w} H_{j,w}$$

The rate of evolution of gaseous pyrolysis products, $\frac{\dot{m}_g}{h}$, is obtained by solution of the conduction equation. Reference 2.1 describes in detail the solution of the coupled mass-transfer and heat-transfer equations.

A major assumption in the adopted ablation model is that the pyrolysis gas composition is frozen during injection into the boundary layer. That is, combustion of the pyrolysis gases will not occur. The assumption will be satisfied provided that kinetics of the neglected reactions are slow. The resulting effect on shield surface erosion predictions may be considered as representing an upper bound. All of the boundary layer oxygen which diffuses to the wall (in the diffusion-controlled regime) reacts to form carbon monoxide. This idealization has enabled satisfactory correlation of both air-arc test data and ballistic missile flight test data as indicated in References 2.1 and 2.3.

However, it is desirable to examine the effect on material response when the "inert" pyrolysis gas assumption is removed. A method for accomplishing this is reported in Reference 2.4 where complete gas-surface equilibrium is assumed. Reaction rates are treated as being infinitely fast. The pyrolysis gases react with the air species thus consuming free oxygen which would otherwise be available for reaction with the carbon char. The net effect is to reduce surface erosion rate.

A comparison of the two methods is presented in Figure 2.3 for nylon-phenolic at a pressure of one atmosphere. The parameter plotted is the ratio of ablation mass flux to the blowing convection coefficient for the quasi-steady erosion situation. For the case of heterogeneous surface reactions, the parameter is invariant up to a temperature of 4500°R, reflecting only oxygen combustion. Thereafter, the cyano reaction at the char surface is of consequence effecting an increase in the mass transfer parameter at the higher wall temperatures. The gas-surface equilibrium method is the lower one as a result of the reduced wall oxygen concentration. It is noted that although the mass transfer parameter differs by a factor of two between the methods, the surface recession rates will not differ in this amount because of the dependence of the blowing heat transfer coefficient on the mass injection rate. Surface erosion rates are compared using the two approaches in a subsequent section.

The nylon phenolic properties data necessary for prediction of material response are presented in Table 2.1 and Figure 2-2 and 2-4. The thermo-physical properties were obtained as part of an extensive laboratory program. The attractiveness of nylon-phenolic as a heat-shielding material is reflected in its low virgin plastic thermal conductivity and its high pyrolysis gas enthalpy level.

2.1.2 Performance Computation Techniques

The description of heat shield temperature response and extent of ablation is accomplished by solution of the coupled shield conduction and boundary layer transport equations. The methods of solution which have been used in the current work are coded for high-speed digital computer calculations and were described in detail in Reference 2.5. Their essential features will be reviewed here.

CHIRP (Charring In Re-Inforced Plastics)

CHIRP is a finite difference formulation of the conduction equation which yields the temperature response and extent of degradation in the general transient situation. All terms of the conduction equation are accounted for in the formulation and variable thermophysical properties are accommodated in the calculations. Kinetics of the pyrolysis reaction are determined by solution of the pertinent rate equations. The dependency of pyrolysis gas enthalpies on temperature and pressure is determined by use of a double interpolation scheme.

The conduction equation is solved by an explicit finite difference procedure, utilizing a forward time derivative and a central space derivative in a lumped parameter system. The space co-ordinate is not transformed. Relatively fine spacing is required to accurately represent the physical phenomena because of the rapid spatial variation of properties in the moving pyrolysis zone. Since stability criteria dictate the use of a small time

interval, the fine spacing required to obtain a solution of reasonable accuracy may result in a time interval which is prohibitively small. To avoid this difficulty, nodes in the pyrolysis zone are subdivided. In the computation, a lumped nodal capacitance is retained to yield a maximum time integration interval while the pyrolysis course and properties are determined at the subnodes to yield a solution of maximum accuracy.

Quasi-Steady Solution

The quasi-steady condition, which exists in the limit as time goes to infinity and the constant temperature surface of a semi-infinite slab recedes at constant rate, implies a fixed temperature distribution as measured from the receding surface. Thus, the assumption of quasi-steady behavior is a valid approximation when the rate of change of the thermally affected zone is small relative to the surface recession rate. This condition is satisfied under transient heating conditions during periods of very high heating and also for constant heating after the initial transient.

In the quasi-steady situation, the conduction equation may be decoupled from the boundary layer transport equation thereby simplifying the calculation of ablation rates. Given the environmental conditions, wall temperature and surface recession rates may be uniquely solved for by use of the surface energy balance and mass transfer equations.

Transient Solution

This program provides an approximate means for rapidly computing the response of char-forming materials to transient heating. The basic results generated are time histories of surface temperature, surface recession, and char layer thickness. The formulation enables evaluation of surface erosion in the reaction rate-controlled, diffusion-limited, and sublimation regimes.

The approximation is made that the capacitance term (solid material energy

absorption) in the conduction equation is small relative to the convection term (pyrolysis gas energy absorption). This enables a direct integration of the conduction equation. When appropriate boundary conditions are applied, relations are obtained sufficient to describe surface recession and char growth rates in terms of the environmental conditions and material parameters.

2.2 MATERIAL RESPONSE PREDICTIONS

The charring organic ablation model described in the previous section is applied to predict material response of 50-50 by weight nylon-phenolic when subjected to three sets of environmental conditions. Surface erosion histories were obtained by use of the TRANSIENT program. These histories formed a boundary condition for subsequent CHIRP solutions which produced detailed internal temperature and degradation data.

Environmental Conditions

Test conditions are tabulated in Table 2.2. The three cases are seen to provide substantial variations in the parameters most affecting extent of ablation. For example, surface recession rates in the diffusion-controlled regime are directly dependent on the blowing value of the heat transfer coefficient and, to a lesser extent, on the non-blowing value. For the conditions shown, the non-blowing convection coefficient for cases 1 and 3 are, respectively, 15 and 4 times greater than for case 2. Thus, significant differences in shield erosion rates may be expected. The effect of the wide variation in stagnation enthalpy and heating rates will be manifested by surface temperature and degradation depths.

Predicted Results

Surface temperature histories are shown in Figure 2-5. The levels are sufficiently high so that with the reaction kinetics model adopted (see Equation 2.3), char oxidation is predicted to be essentially diffusion-controlled

after the initial transient temperature rise. (Reaction rates are predicted to be relatively fast in comparison with diffusion rates.) Cyanogen production which becomes prominent at temperatures greater than 4500°R will not occur for the conditions considered.

The swift rise in wall temperature at the early times is attributable to the low virgin material thermal conductivity. Most of the initial heat input is stored in a small thickness near the surface. The degree of attainment of the steady ablation condition may be inferred from the rate of surface temperature change. (Surface temperature would be constant for steady ablation.) The results indicate that this condition is reached for case 1 while case 3 appears to approach it at the later times. The continuing rise in temperature for case 2 may be interpreted as the indication of a transient situation throughout the heating period.

Surface recession and char growth histories are depicted in Figure 2-6. In these and the remainder of the results, the char-layer-virgin material interface has been arbitrarily defined as the plane at which the temperature is 1200°F. At this temperature the density is near that of the residual char. In reality, a pyrolysis zone in which significant weight loss has occurred exists between the temperature limits of approximately 900 to 1200°F but it is generally physically thin.

The conclusions drawn from the preceding examination of surface temperature histories are substantiated by this data. That is, the erosion condition for case 1 is seen to be quasi-steady. A constant char layer thickness is reached early in the exposure period and maintained throughout. The high convective coefficient results in a rapid rate of oxygen diffusion to the surface and a correspondingly high rate of char consumption. The surface moves at a relatively high velocity into the material and results in a thin char layer.

The ablation history for case 3 is also seen to approach the quasi-steady

situation near the end of the run. The char layer build-up is somewhat greater than for case 1 owing to the lower rate of surface recession.

The material behavior for case 2 is observed to be distinct from the other two. A relatively thick char and small rates of surface erosion are predicted because of the environmental conditions peculiar to this case; a high stagnation enthalpy in combination with a low convection coefficient yields sizeable energy transfer to the surface while limiting the amount of oxygen diffusion to the surface. Towards the end of the heating period, the char layer thickness is growing nearly linearly with time. Under these heating conditions, a very long exposure time would be required before the steady ablation situation would be attained.

Figures 2-7 through 2-9 contain internal temperature response predictions at various depths. For case 1, Figure 2-7, the high surface recession rates are exhibited by the time required for a point in the material to go from initial to surface temperature, this value being on the order of five seconds. For this particular case, the temperature histories for five seconds past the cessation of heating are shown. Because of their rapid decrease below the pyrolysis temperature, it may be concluded that very little mass loss occurs during this period.

The rates of temperature rise for cases 2 and 3 are seen to be much less severe. Predictions were carried out for models of different length for each of the cases, however, no backface temperature rises are predicted under any of the heating conditions.

Table 2.3 contains a summary of the response predictions. Listed is information concerning the modes of surface heating, the manner in which this heating is accommodated, and ablation rate data. Referring first to case 1, it may be seen that the net heat input to the surface (\bar{q}_n) is only slightly greater than one-half the cold wall heating rate, thus demonstrating one of the advantages of charring ablators. The majority of the reduction is due to

the strong effect of mass transpiration on the convective heating. Because of the high surface recession rate for this condition, a substantial combustive heat flux results (\bar{q}_c), being nearly one-fourth of the net heat input to the surface. The energy is accommodated in three ways: In pyrolyzing the virgin material (\bar{q}_p), in raising the temperature and in chemical cracking of the pyrolysis gases (\bar{q}_g), and in raising the enthalpy of the solid (\bar{q}_s). The sensible and chemical enthalpy rise of the pyrolysis gases accounts for the majority of the net heat input. For these environmental conditions, the gases absorb 4300 BTU per pound in their transit through the char layer. Approximately one-eighth of the net heat input is absorbed during degradation of the virgin polymers. The attractiveness of the ablative heat shield concept is again reflected in the heat storage term (\bar{q}_s). This value is only one-tenth of the cold wall heating rate.

A comparison of the final values of surface recession and char layer-virgin material interface velocities is an indication of the attainment of quasi-steady conditions while a comparison of their averages would imply over what relative portion of the heating period steady conditions existed. For case 1, this comparison shows that steady-state ablation existed at the end of the exposure period as well as over the majority of the run. Final erosion distance is an order of magnitude greater than the final char thickness. The total weight loss is predicted to be nearly 3 lbs/ft².

The cold wall heating rates for cases 2 and 3 were of the same order so that a comparison of their results is appropriate. The net heating rate for case 3 is double that of case 2. An examination of the heating conditions furnishes an explanation. The mass loss rate for case 2 reduces the non-blowing convective coefficient by more than 60 percent. For case 3, with its higher non-blowing heat transfer coefficient, the mass loss rate for this condition, even though greater than for case 1, reduces the convective coefficient by only 30 percent. For the higher stagnation enthalpy situation blowing is more influential in reducing the net heat input to the surface. This fact plus the greater combustive heating rate for case 3 leads to the higher net

heating rate.

The division of the actual energy transferred to the material among the several energy absorbing mechanisms is approximately the same for cases 2 and 3. As in case 1, it is seen that the energy absorbed by the pyrolysis gases predominates.

An examination of the surface and interface velocities for the two situations reveals that the case 2 ablation condition is a transient one. Char thickness continually changes with time. Case 3, approaches the quasi-steady ablation condition; i.e., the surface recession and char penetration velocities are very nearly equal so that the char thickness is essentially invariant with time.

The total mass losses are of the same order in spite of the variation in the net heating rates. The greater char layer thickness for case 2, and the associated higher density loss in the char zone, compensates for its lower surface recession.

Effect of Surface Reaction Assumptions

Two limit assumptions for the chemical behaviour of the pyrolysis gases upon injection into the boundary layer have previously been discussed. These are: (1) The pyrolysis gases do not enter into reactions with the carbon surface, the air species, or the products of carbon-air specie reactions and (2) The pyrolysis gases react infinitely fast resulting in complete gas-surface equilibrium. The first assumption has been utilized in the preceding material response predictions and will be utilized throughout Section 3. The effect of this assumption on material ablation performance predictions will now be examined.

Quasi-steady ablation values of wall temperature and surface recession rates have been predicted for the three environmental conditions previously

described in Table 2.2. In each case, results were obtained for the two limit assumptions. They are compared in Table 2.4. (Also included in Table 2.4 are data from the transient solutions which used the frozen pyrolysis gas composition idealization. From a comparison of the transient and quasi-steady predictions it is obvious that quasi-steady conditions were essentially attained in case 1, approached by case 3, and unachieved in case 2. The comparison of transient and quasi-steady solutions for surface temperature, in particular, shows that ablation behaviour in case 2 is far from quasi-steady.)

Two trends are immediately apparent from the results of Table 2.4. Application of the gas-surface equilibrium model yields lower surface recession rates and higher wall temperatures. As mentioned previously, the oxygen at the surface which is available for erosive reaction with the char is reduced because of its consumption in reaction with the pyrolysis gases. Thus the surface recession rate is reduced and the mass transpiration effect decreased. Heating is increased by the exothermic combustion of pyrolysis gases. The increased combustion heat transfer and reduced rate of material consumption require greater heat absorption per pound of material removed and hence the surface temperature is greater than with the heterogeneous surface reaction model.

Although the two models provide extreme limits on the actual gas-phase-reaction-kinetics, they do not yield widely different results. For example, in case 1, the assumption of complete equilibrium yields surface erosion rates 30 percent smaller and surface temperatures 20 percent greater than does the frozen pyrolysis gas assumption. Theoretical identification of the more realistic model is not possible without the acquisition of extensive reaction rate data and solution of the complex reacting-boundary-layer equations. However, the relative merits of the two models may be examined by comparison of predictions with measurements of gross material performance.

2.3 COMPARISON OF PREDICTION AND DATA

Subsequent to completion of the theoretical predictions of sample response, experimental data on the ablation of nylon phenolic was provided to IMSC by NASA for the three environmental conditions previously described. A direct comparison of the theoretical predictions and experimental measurements of material performance is presented here in assessment of validity of the theory.

Experimental Data

The experiments were conducted in arc-heated air streams with the flow impinging on hemispherical models. In each case, convection was the only significant heating mechanism. The results are given, together with the test conditions, in Table 2.5. The cold wall convective heating rates and surface pressures were measured with instrumented, non-ablating models and the total enthalpies were determined by the equilibrium sonic flow method. The ablation data were obtained by measuring sample thickness, char depth and sample weight of a removable central core before and after heating. (The char depth as used here is the thickness of the completely degraded material. The pyrolysis zone in which partial degradation evidenced by material discoloration occurs is excluded.) Surface temperatures were obtained by pyrometric techniques and are based on an assumed surface emissivity of 0.85. Several models were tested at conditions 1 and 3. Each was run for a different time duration which yielded a gross description of the transient ablation history. The surface erosion and char penetration rates given in Table 2.5 for these cases were obtained at NASA by plotting thickness results as a function of test duration and then evaluating the slope of the curves in the linear region (after the initial transient.) Only one model was tested at condition 2. The tabulated rates for this case are average values for the time period of the test. Reference 2.6 provides a comprehensive description of the experimental techniques, ablation measurements, and data interpretation.

Data Comparisons

The experimental data on ablation performance are compared in Table 2.6 with the two limit theoretical predictions of Section 2.2. The results identified as Theory 1 are obtained using the inert pyrolysis gas model. The rate values correspond to time averages over the test period as derived from results of the transient response calculations. Theory 2 corresponds to the complete chemical equilibrium model and the tabulated rates are those computed for quasi-steady ablation. (As discussed in Section 2.2, quasi-steady ablation behaviour is not achieved for the environmental conditions of case 2. Therefore the comparison of Theory 2 with data is not made for case 2.)

The comparisons of Table 2.6 when considered as a whole substantiate the validity of the general thermochemical performance model. The variation of ablation performance with test conditions is correctly predicted and the magnitudes are in fair agreement. The two limit assumptions on the kinetics of pyrolysis gas reactions with air yield results bracketing the experimental data on surface recession rates. When pyrolysis gas reactions with air are neglected, the comparisons indicate that the rate of surface recession is slightly overpredicted. Predicted surface temperatures are significantly lower than observed, however. The assumption of complete chemical equilibrium yields temperatures in good agreement with the measured values, but predicted erosion rates are slightly low. These comparisons do not clearly demonstrate which limit assumption on pyrolysis gas kinetics is the superior one. Apparently neither enables highly accurate prediction of both surface temperatures and ablation rates. Several possible explanations may be advanced for the discrepancies. Foremost of these is inaccuracy in experimental data. For example, systematic error in surface temperature readings may offer an explanation for the differences between measured and theory 1 values. A second possibly significant error source is the neglect of mechanical erosion. Some evidence exists indicating this may be an appreciable contributor to surface recession. If such does occur, it would explain the slightly low recession rates predicted using Theory 2.

It must be concluded that further and more detailed comparisons of theory and experiment are required to resolve the pyrolysis gas reaction kinetics question. Of the two reaction models examined, the one neglecting reactions between pyrolysis gases and air species is currently favored. This model yields the more conservative predictions for extent of material ablation. In previous ground test and flight test data correlation applications, it has yielded results for internal temperature histories and course of ablation which are in good agreement with measurements (References 2.1 and 2.3).

2.4 SUMMARY

The theoretical performance model developed by Kratsch, Hearne and McChesney for prediction of the performance of charring materials has been applied to describe material performance in three distinct environmental situations. In review of the model, it accounts in the general transient situation for

- o chemical erosion of the surface in both the reaction rate-limited and diffusion controlled regimes
- o reaction rate-limited pyrolysis of the virgin material
- o heat absorption by virgin material, partially pyrolyzed solid material, and residual char
- o heat absorption in the pyrolysis reaction
- o heat absorption by pyrolysis gases during their movement through the char layer
- o heat liberation or absorption by chemical reactions at the surface

The following assumptions and approximations are incorporated in the model.

- o no mechanical erosion of material
- o boundary layer diffusion rates correspond to those for a binary mixture with Lewis and Prandtl numbers of unity
- o no pyrolysis gas/air reactions
- o pyrolysis gases in local thermal equilibrium with char
- o pyrolysis gas mixture in chemical equilibrium
- o homogeneous material

The influence of the major assumption that pyrolysis gas/air reactions do not occur within the boundary layer has been examined. It is shown that the assumption yields maximum surface erosion rates, but minimum surface temperatures. The opposite limit assumption of complete chemical equilibrium within the boundary layer was introduced to obtain a second set of results which with the first would be expected to bracket the actual material response.

The two limit assumptions yield results which are not markedly different. Comparison of the predictions with experimental data tends to substantiate the assumption of an equilibrium boundary layer when the possibility of slight mechanical erosion is admitted. However, the opposite limit assumption is favored for design analysis application since it is the more conservative one and since it has provided results in reasonable agreement with experiment in previous data correlations.

REFERENCES

- 2.1 K. M. Kratsch, L. F. Hearne, and H. R. McChesney, "Theory for the Thermophysical Performance of Charring Organic Heat Shield Composites", 803099, Lockheed Missiles and Space Co., 18 Oct. 1963.
- 2.2 L. Lees, "Convective Heat Transfer with Mass Addition and Chemical Reactions", Third AGARD Combustion and Propulsion Colloquium, May 1958.
- 2.3 L. F. Hearne, W. D. Coleman, and S. R. Foiles, "Flight Test Corroboration for the Thermophysical Behavior of Char-Forming Organic Polymers", Paper presented at 6th U. S. Navy Symposium on Aeroballistics.
- 2.4 R. A. Rindal, D. T. Flood, and R. M. Kendall, "Analytical and Experimental Study of Ablation Material for Rocket-Engine Application", Vidya Report No. 136, 17 March 1964.
- 2.5 "Study of Heat Shielding Requirements for Manned Mars Landing and Return Missions", LMSC 4-74-64-1, December 1964.
- 2.6 John H. Lundell, Roy M. Wakefield, and Jerold W. Jones, "Experimental Investigation of a Charring Ablative Material Exposed to Combined Convective and Radiative Heating in Oxidizing and Non-Oxidizing Environments", Paper presented at AIAA Entry Technology Conference, Williamsburg and Hampton, Virginia, October 12-14, 1964.

NOTATION

E	Activation energy
H	Total enthalpy
h	Convection coefficient
K_j	Concentration by mass of molecular specie j
K_i	Concentration by mass of elemental specie i
k	Thermal conductivity
k_o	Reaction rate constant
\dot{m}	Mass rate of char erosion
\dot{m}_g	Mass rate of pyrolysis gas production
n	Reaction order
P_e	Static pressure
q_r	Radiation heat flux
R	Gas constant, 1.987 BTU/mole $^{\circ}R$
y	Distance normal to surface
ϵ	Surface emissivity
σ	Stefan-Boltzmann constant

SUBSCRIPTS

c	Char
g	Pyrolysis gas
w	Wall

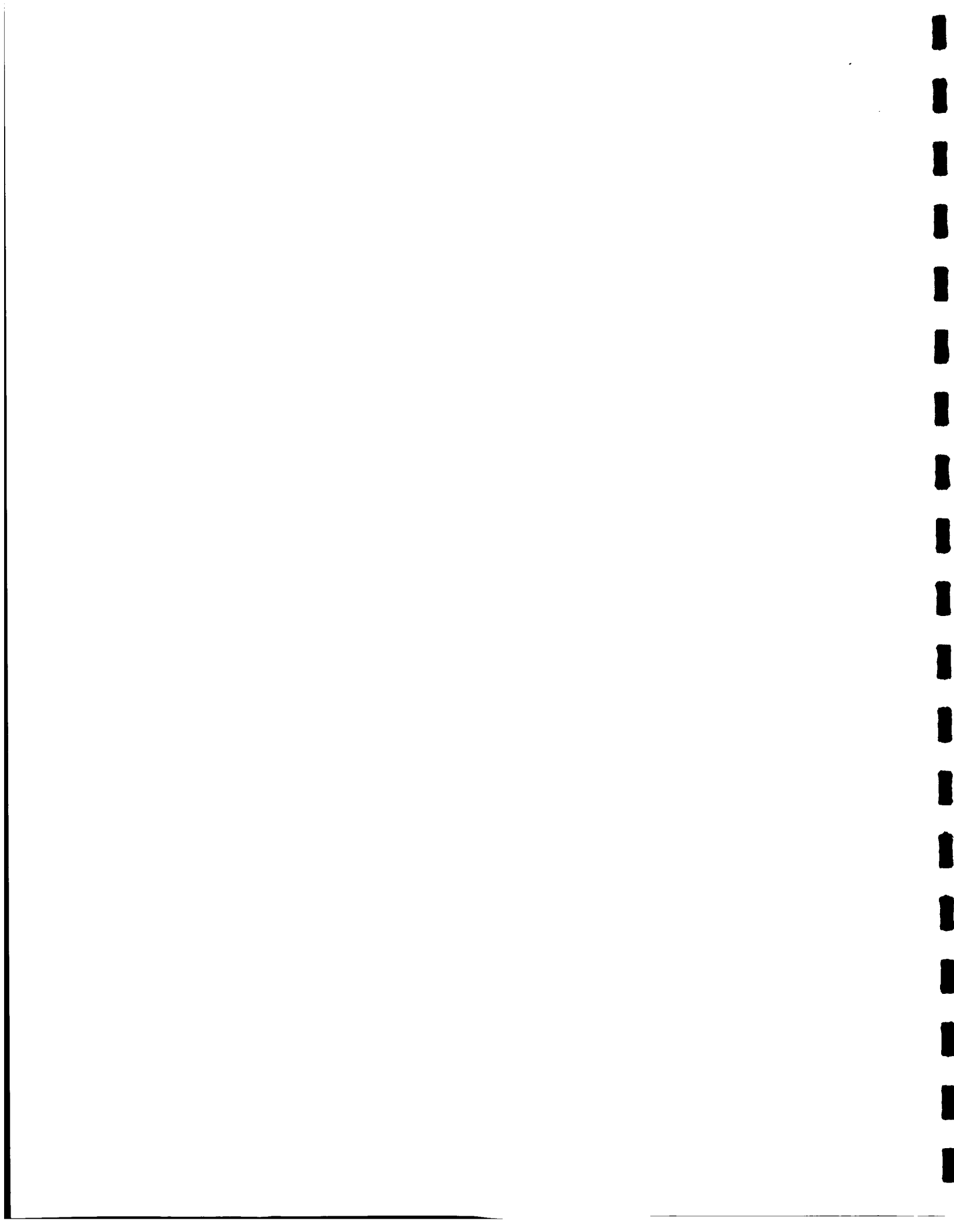


TABLE 2.1
 NYLON-PHENOLIC THERMOPHYSICAL AND THERMOCHEMICAL PROPERTIES

QUANTITY	VALUE
Virgin Material Density	75.0 LB/FT ³
Char Density	18.7 LB/FT ³
Surface Emissivity (Virgin Material)	0.8
Surface Emissivity (Char)	0.6
Heat of Formation (O°R)	-1263 BTU/LB
Specific Rate Constant (k _o)	7.89 x 10 ¹² (SEC ⁻¹)
Activation Energy (E/R)	45,000 (°R)
Reaction Order (n)	2.0

TABLE 2.2
DESCRIPTION OF NYLON-PHENOLIC ENVIRONMENTAL TEST CONDITIONS

CASE	STAGNATION ENTHALPY (BTU/LB)	COLD WALL HEATING RATE (BTU/FT ² -SEC)	STAGNATION PRESSURE (ATM)	DURATION OF HEATING (SEC)
I	4,000	800	2.620	30
II	10,000	134	.021	60
III	3,080	162	.045	25

TABLE 2.3

SUMMARY OF NYLON PHENOLIC RESPONSE PREDICTIONS

CASE	T _{sf}	ENERGY TRANSFER DATA										ABLATION DATA									
		\bar{q}_{cw}	$\bar{q}_{hw_{nb}}$	\bar{q}_{hw_b}	\bar{q}_c	\bar{q}_n	\bar{q}_p	\bar{q}_g	\bar{q}_s	\bar{m}_{pg}	\bar{m}_c	\bar{V}_s	V_{sf}	\bar{V}_c	V_{cf}	ΔS	ΔC	ΔW			
	(°R)	(Btu/ft ² sec)										(in/sec)								(lbs/ft ²)	
I	3860	800	640.0	392.0	99.0	421.7	54.4	283.5	83.8	.07660	.02300	.01470	.01491	.01635	.01491	.4567	.0337	2.99			
II	2870	134	129.9	54.5	4.2	47.7	7.8	28.3	11.6	.01168	.00101	.00065	.00085	.00249	.00186	.0392	.1104	.76			
III	2700	162	135.6	86.6	19.2	93.8	15.3	56.1	22.4	.02240	.00466	.00299	.00392	.00478	.00409	.0748	.0448	.68			

NOTE: Bar denotes average value over duration of heating.

Subscript f denotes value immediately prior to end of heating.

T_s	- surface temperature	\dot{q}_s	- sensible enthalpy rise of solid ($\dot{q}_n = \dot{q}_p + \dot{q}_g + \dot{q}_s$)
\dot{q}_{cw}	- cold wall convective heating rate	\dot{m}_{pg}	- pyrolysis gas production rate
\dot{q}_{hwnb}	- hot wall convective heating rate without blowing	\dot{m}_c	- char removal rate
\dot{q}_{hwb}	- hot wall convective heating rate with blowing	V_s	- surface recession velocity
\dot{q}_c	- char combustion heating rate	V_c	- char layer-virgin material interface velocity
\dot{q}_n	- net heating rate ($\dot{q}_n = \dot{q}_{hwb} + \dot{q}_c - \epsilon \sigma T_s^4$)	ΔS	- total surface recession
\dot{q}_p	- energy absorbed in pyrolyzing virgin material	ΔC	- final char layer thickness
\dot{q}_g	- energy absorbed by pyrolysis gases	ΔW	- total mass loss

TABLE 2.4

EVALUATION OF SURFACE REACTION CHEMISTRY ON QUASI-STEADY ABLATION PERFORMANCE

CASE	TRANSIENT PREDICTIONS*		QUASI-STEADY PREDICTIONS			
	HETEROGENEOUS AIR-SURFACE REACTIONS ONLY		HETEROGENEOUS AIR-SURFACE REACTIONS ONLY		COMPLETE GAS-SURFACE EQUILIBRIUM	
	SURF. TEMP. °R	SURF. EROS. RATE IN/SEC	SURF. TEMP. °R	SURF. EROS. RATE IN/SEC	SURF. TEMP. °R	SURF. EROS. RATE IN/SEC
I	3860	.01491	3860	.01500	5020	.00985
II	2870	.00085	3550	.00100	4000	.000545
III	2700	.00392	2730	.00396	3875	.00210

* Value Predicted Immediately Prior to End of Heating

TABLE 2.5
EXPERIMENTAL RESULTS OF ABLATION TESTS ON HIGH DENSITY NYLON PHENOLIC

CASE	TEST CONDITIONS				TEST RESULTS				
	q_{c_w} Btu/ft ² sec	h_T Btu/lb	p_s atm	Time sec	\dot{m}_t lb/ft ² sec	V_s in/sec	V_c in/sec	V_p in/sec	T_s °R
I	800	4000	2.62	30	-	.0144	.0144	-	5080
II	134	10000	0.021	60	.0152	.000564	-	.00386	3870
III	162	3080	0.045	25	.0257	.00236	.0044	.00565	4170

\dot{m}_t - mass loss rate
 V_s - surface recession velocity
 V_c - char penetration velocity
 V_p - pyrolysis zone penetration velocity
 T_s - surface temperature

TABLE 2.6

COMPARISON OF EXPERIMENTAL DATA AND THEORETICAL PREDICTIONS

CASE	1	2	3	AVERAGE DEVIATION PERCENT
V_s (in/sec)	Measured	.0114	.00236	N.A.
	Theory 1	.0147	.00299	14.9
	Theory 2	.00985	.00210	-21.3
V_c (in/sec)	Measured	.0144	.00440	N.A.
	Theory 1	.0163	.00478	10.9
\dot{m}_t (lb/ft ² sec)	Measured	-	.0152	N.A.
	Theory 1	-	.0127	- 5.1
T_s (°R)	Measured	5080	4170	N.A.
	Theory 1	3860	2700	-28.4
	Theory 2	5020	3875	- 4.1

Theory 1 assumes pyrolysis gases to be chemically inert within boundary layer

Theory 2 assumes complete chemical equilibrium at the ablator surface

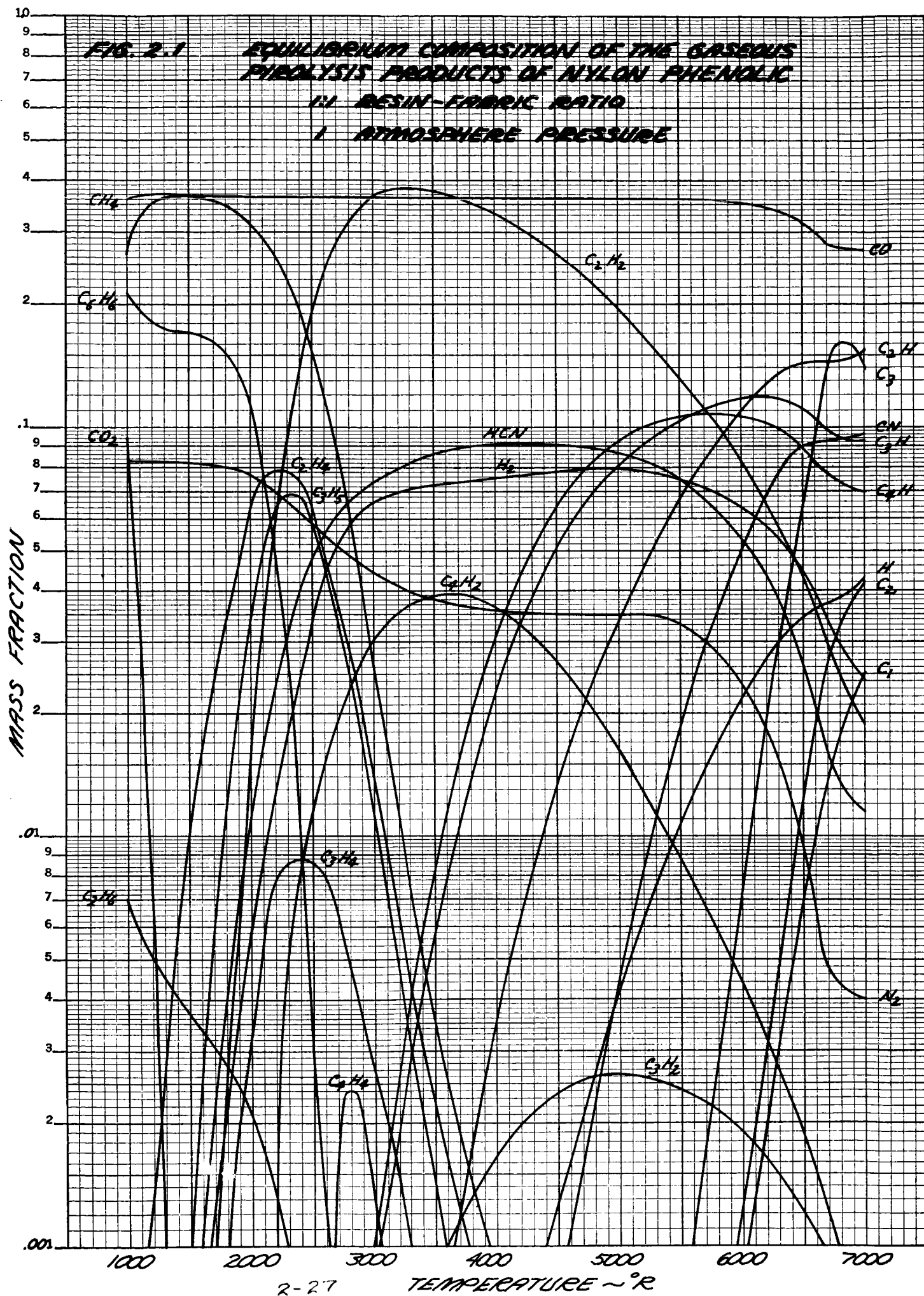
 V_s - surface recession velocity V_c - char penetration velocity \dot{m}_t - mass loss rate T_s - surface temperature

FIG. 2.1

EQUILIBRIUM COMPOSITION OF THE GASEOUS
PYROLYSIS PRODUCTS OF NYLON PHENOLIC

1:1 RESIN-FABRIC RATIO

1 ATMOSPHERE PRESSURE



**FIG. 2.2 GAS ENTHALPY OF THE PYROLYSIS
PRODUCTS OF NYLON PHENOLIC
1:1 RESIN-FABRIC RATIO**

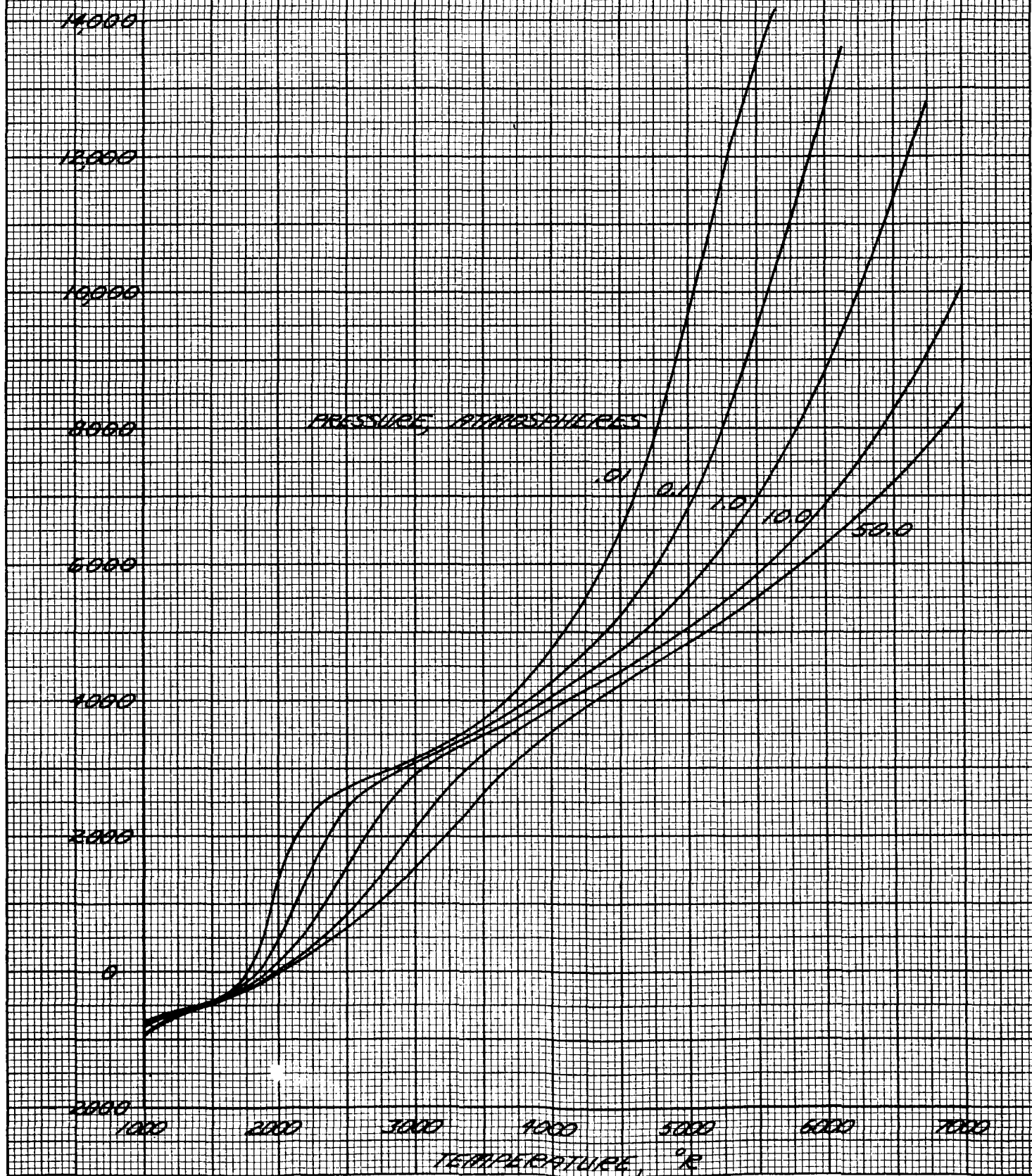


FIGURE 2-3
 EVALUATION OF SURFACE REACTION CHEMISTRY
 ON QUASI-STEADY MASS TRANSFER

WATERGAS: 10% H₂, 90% CO
 PRESSURE: 1.0 ATMOSPHERE

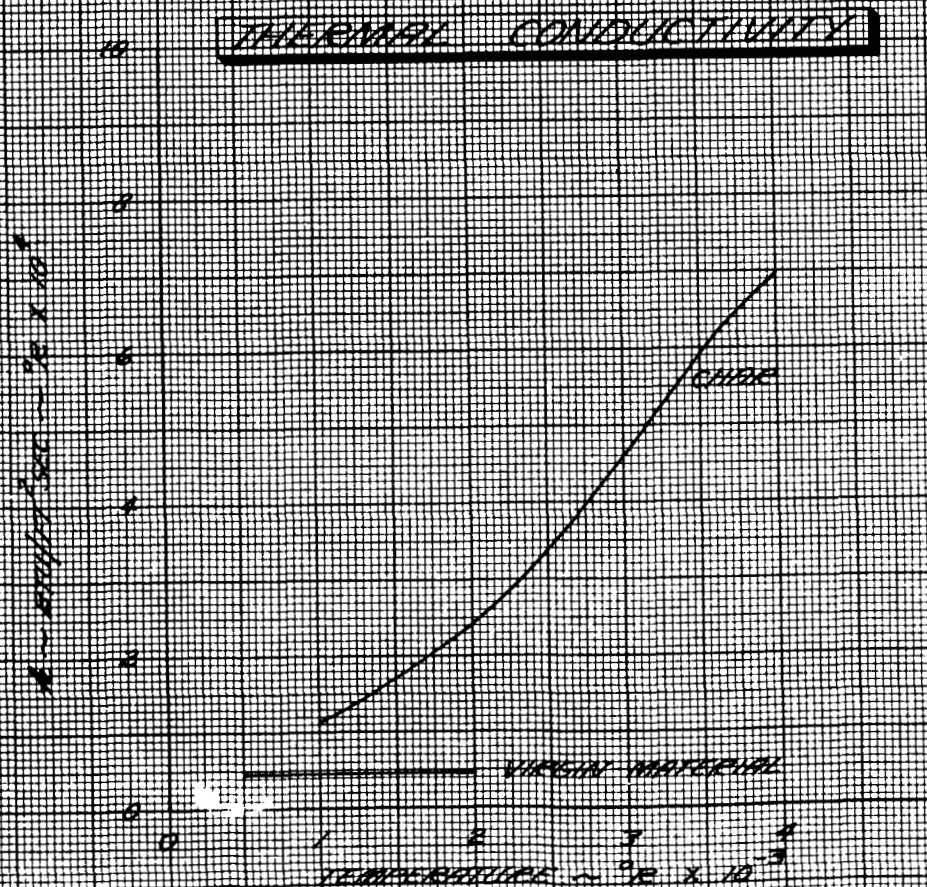
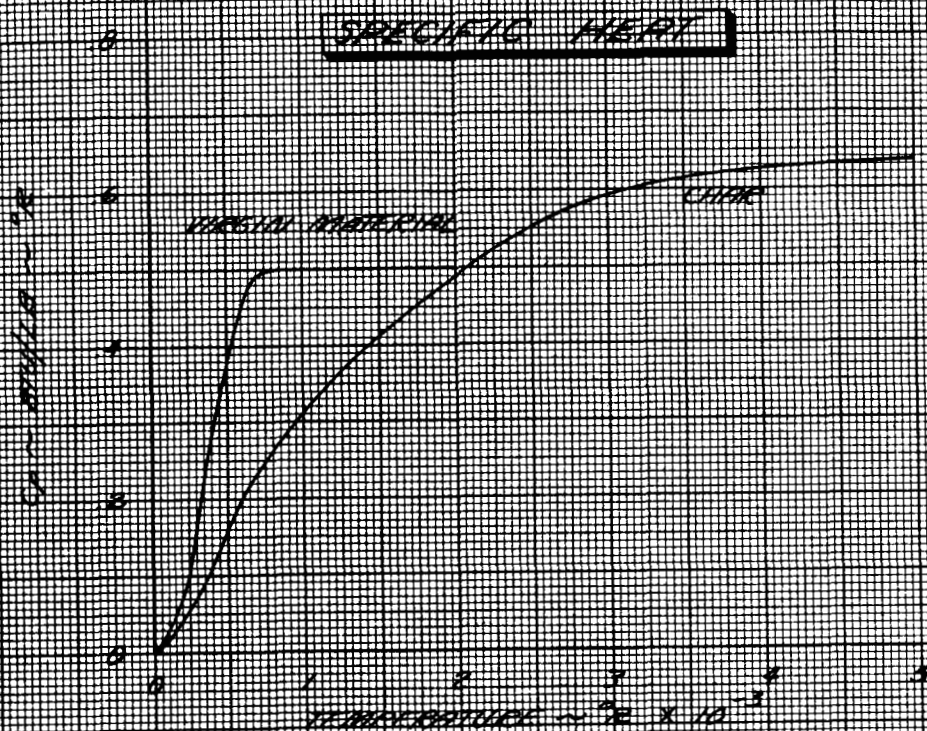
WATERGAS: 10% H₂, 90% CO
 REACTIONS ONLY

COMPLETE GAS SURFACE
 EQUILIBRIUM

SURFACE TEMPERATURE ~ 2000°K

$(\text{Gr})_{\text{eff}} / \rho_{\text{eff}} \sim \text{MASS TRANSFER PARAMETER}$

FIGURE 2-4
 NYLON-PHENOLIC THERMOPHYSICAL PROPERTIES



PREPARED BY MM
DATE _____
CHECKED BY _____

LOCKHEED MISSILES & SPACE COMPANY
A GROUP DIVISION OF LOCKHEED AIRCRAFT CORPORATION

PAGE _____
MODEL _____
REPORT NO. _____

FIGURE 2-5
NYLON-PHENOLIC SURFACE TEMPERATURE HISTORIES

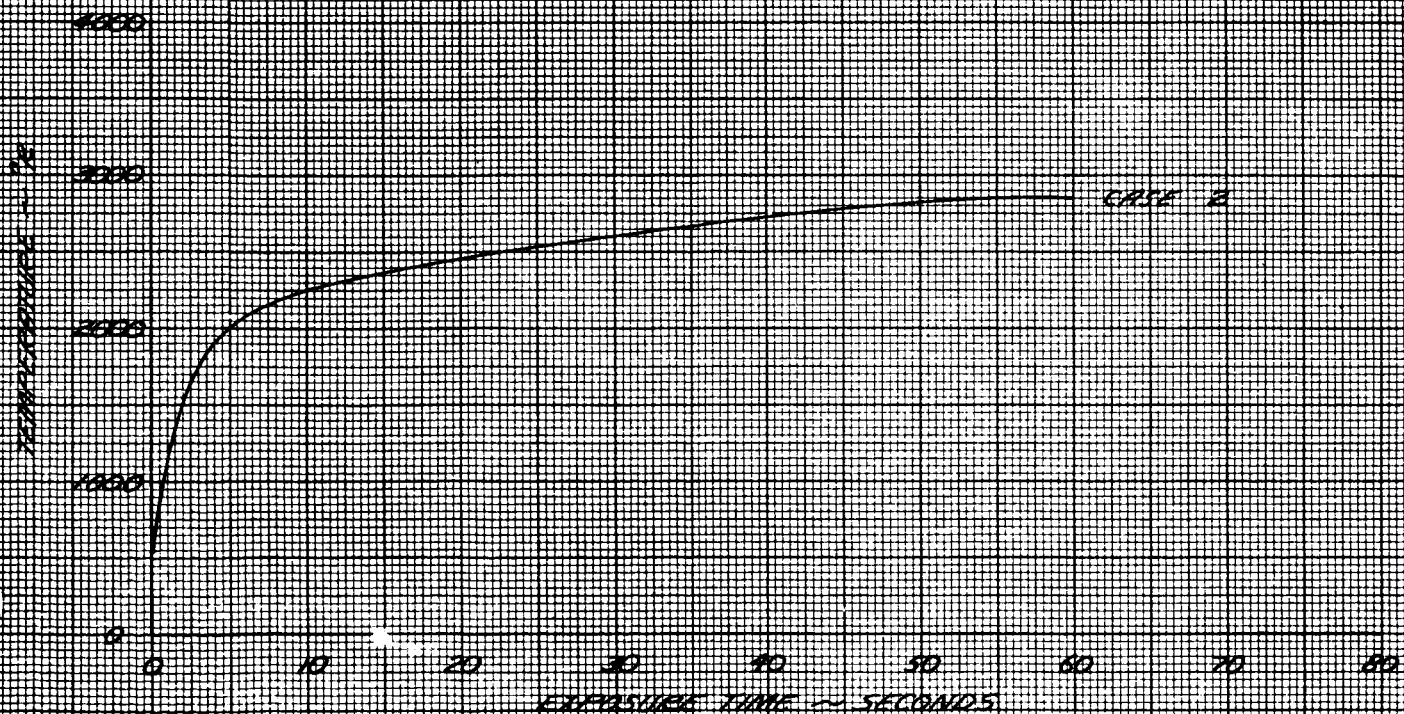
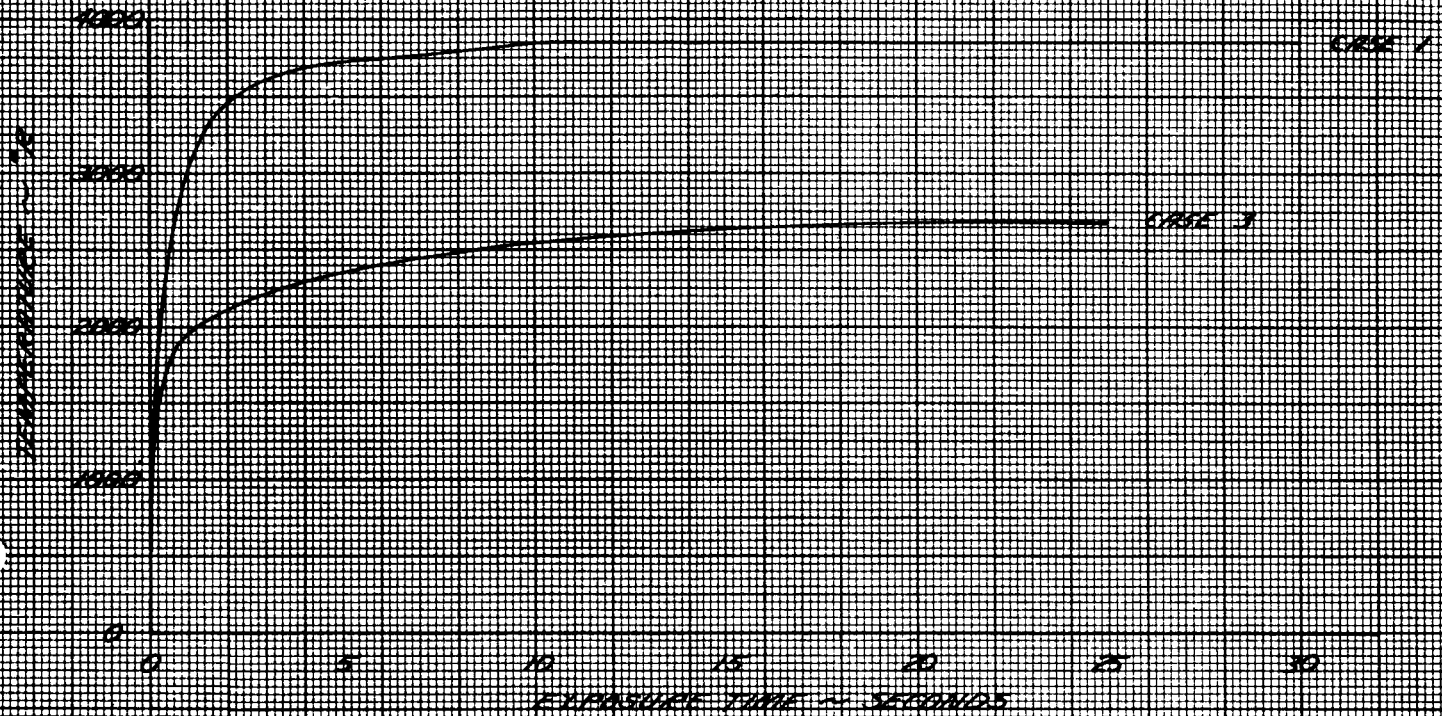


FIGURE 3-6
NYLON PHENOLIC ABLATION HISTORY

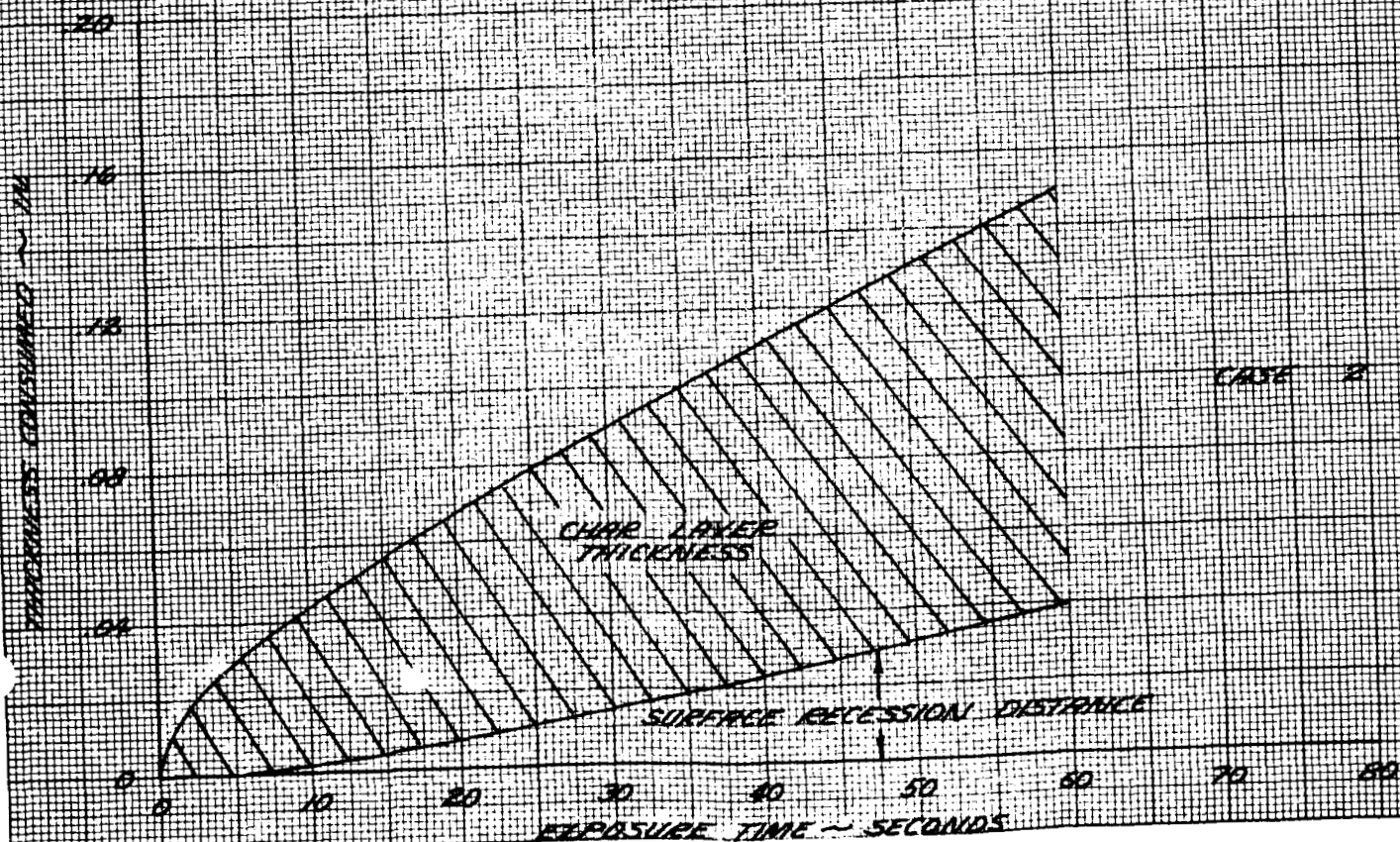
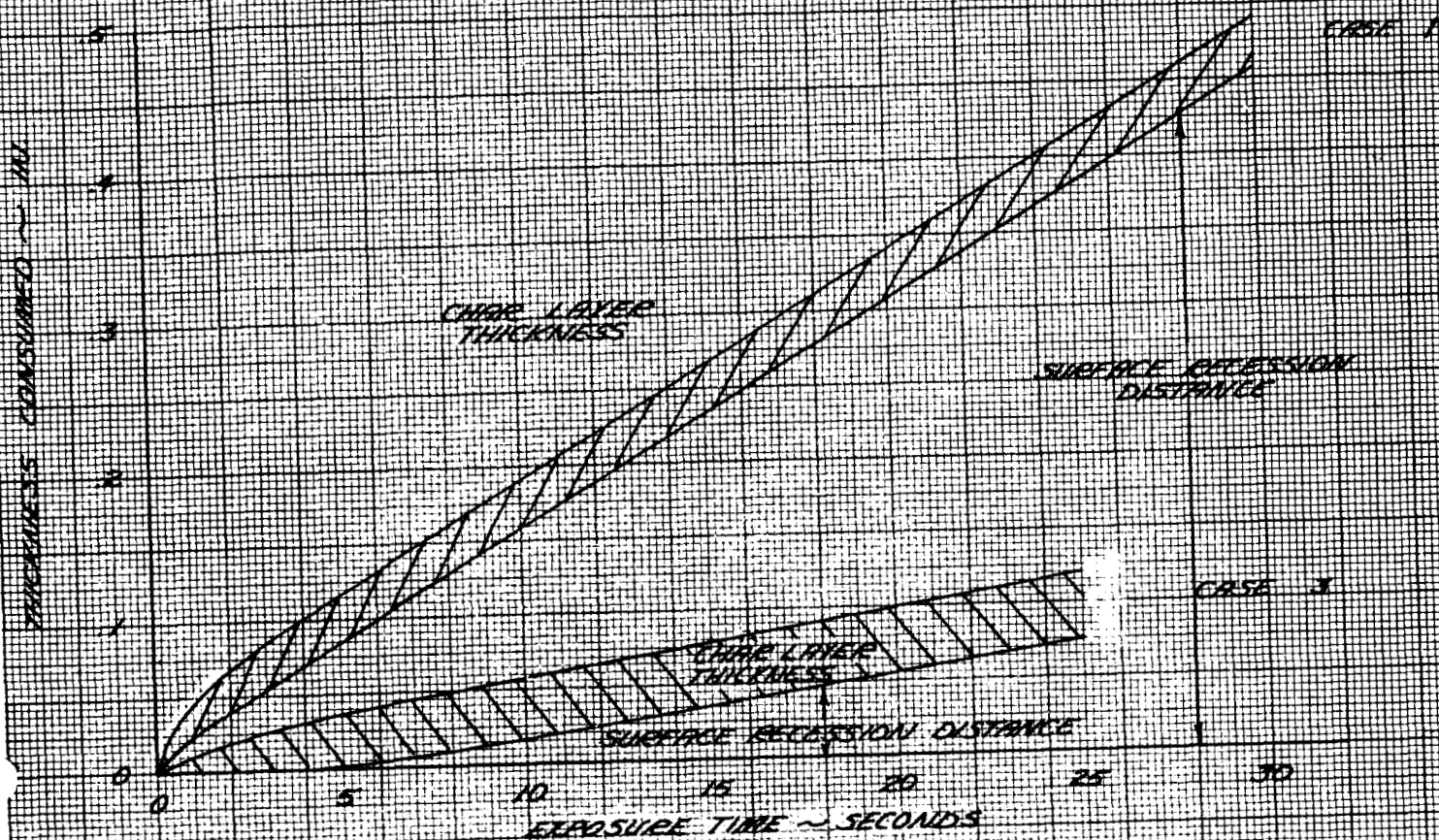


FIGURE 2-7
 AXIOM-PHENOLIC INTERNAL TEMPERATURE RESPONSE
 CASE 1

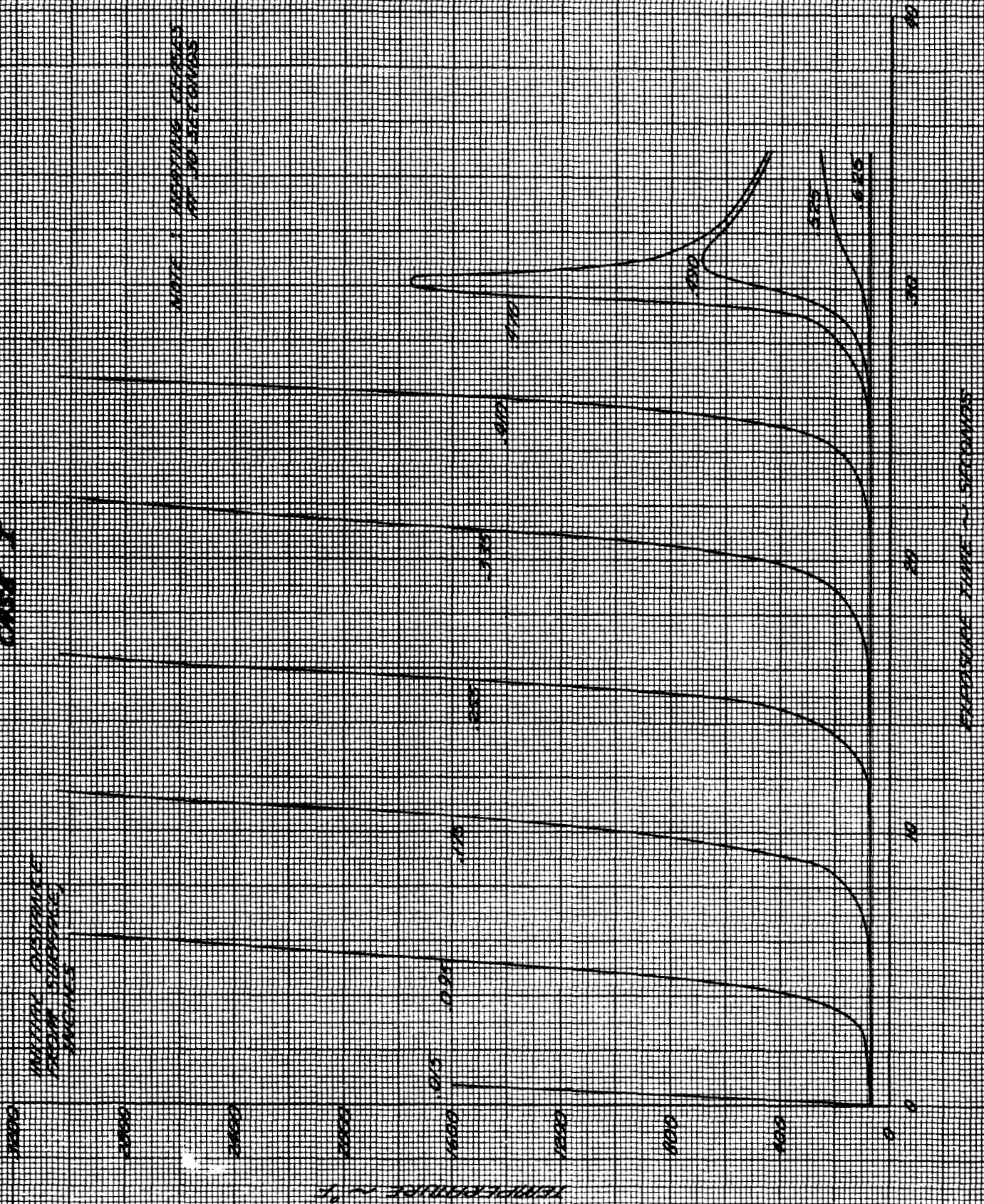


FIGURE 1-1
 NIION-PHENOLIC INTERNAL TEMPERATURE RESPONSE
 CASE II

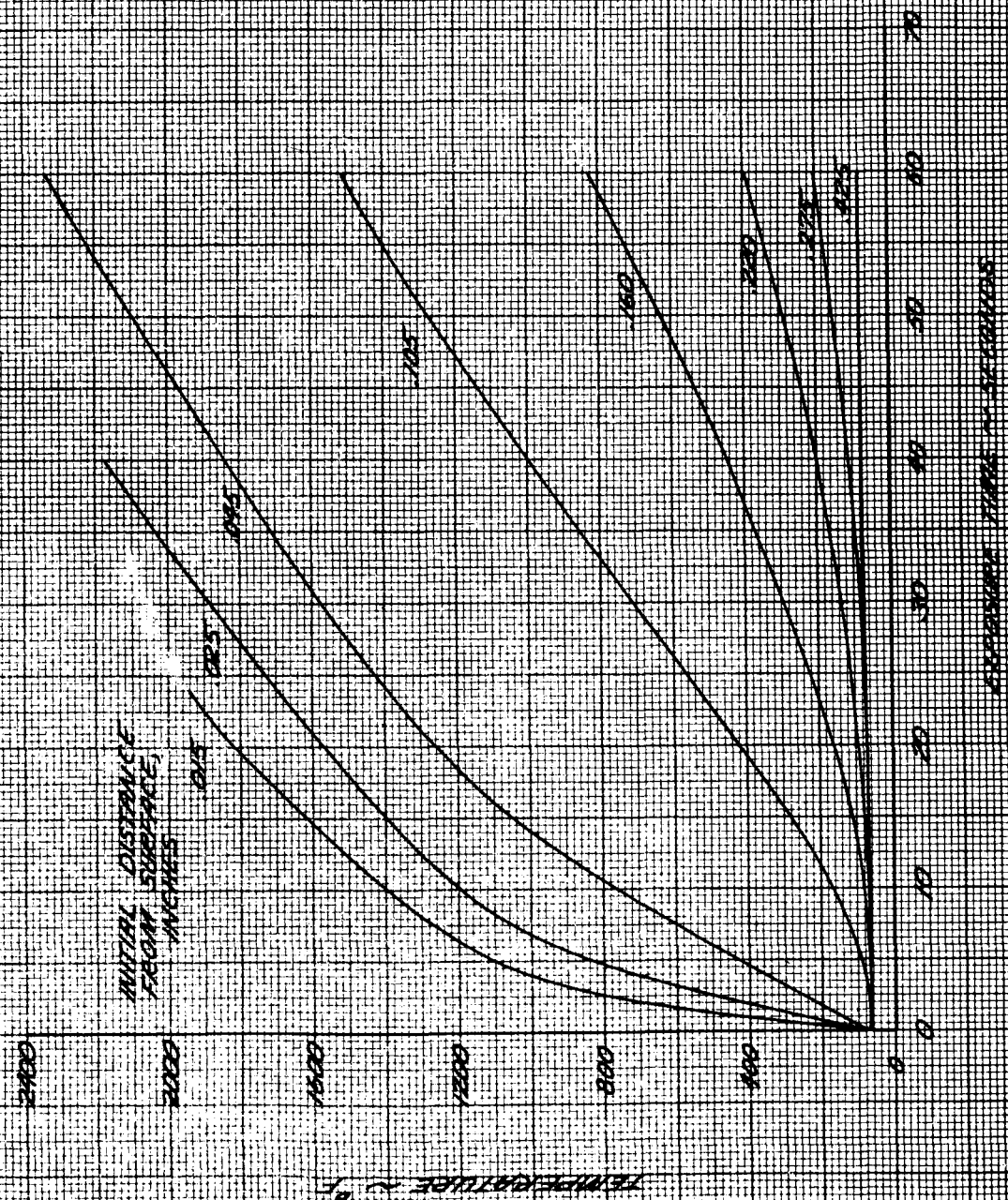
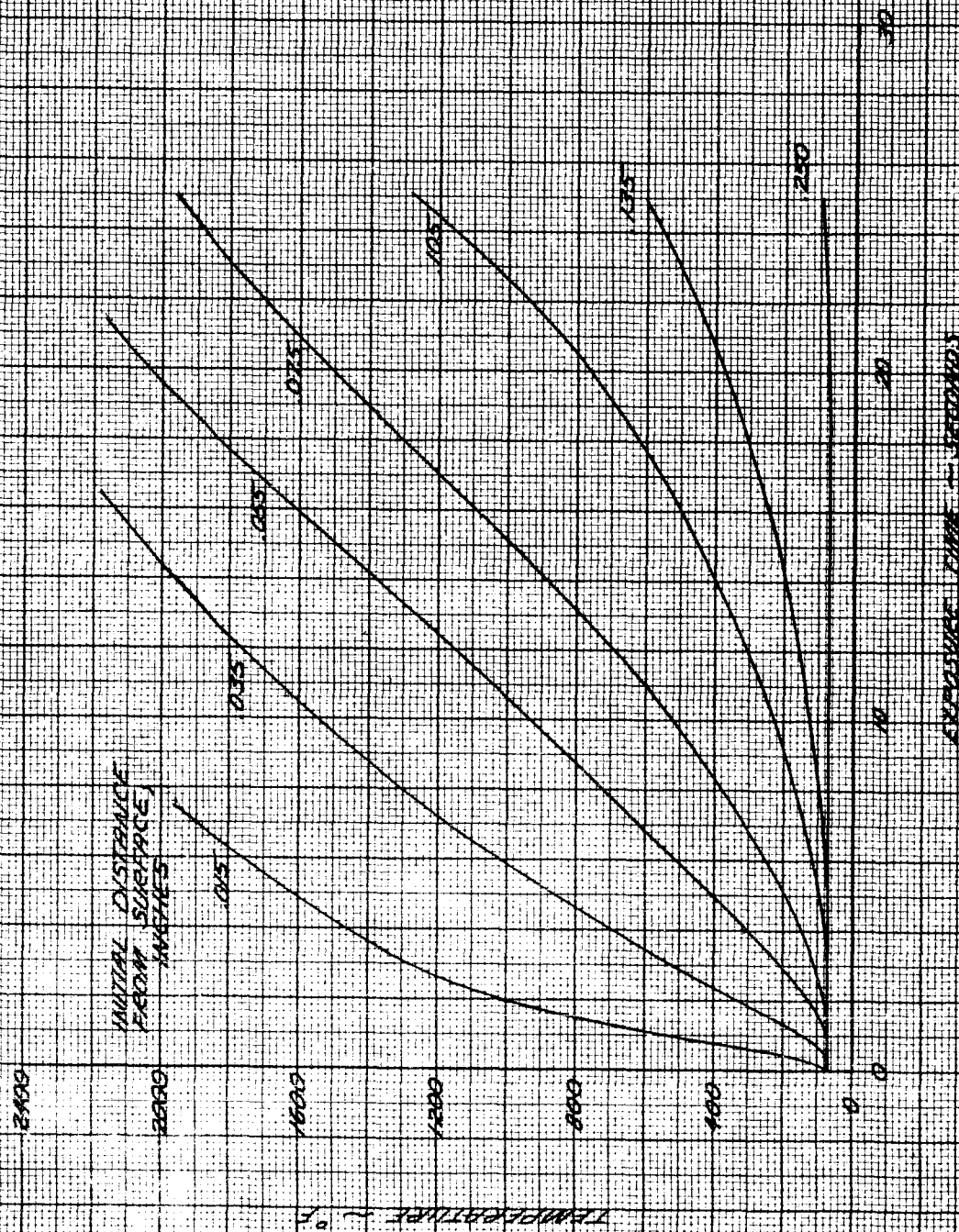


FIGURE 2-9
 NYLON-PHENOLIC INTERNAL TEMPERATURE RESPONSE
 CASE III



Section 3

HEAT SHIELDING REQUIREMENTS

Thermal protection requirements for superorbital entry into the earth's atmosphere are described in this section for two lifting vehicles of the biconic configuration class. The results demonstrate the influence of both entry velocity and corridor position on shield weight. They further show the heat-shield design penalties associated with uncertainties encountered in prediction of the environment. Finally, they indicate the extent and effects of nose shape change.

Required in acquisition of the shield weights were definition of vehicle flight performance, the aerothermal environment, and the shield material transient response. The basic techniques used in each of these analysis areas are related and representative results are presented.

3.1 VEHICLE PERFORMANCE

This section describes the entry performance of the two biconic vehicles. First, the physical and aerodynamic characteristics of the reentry modules are indicated. Then the entry trajectory model adopted for the study is discussed and a typical trajectory is presented. A more comprehensive discussion of the methods which have been used in determining the vehicle performance may be found in Reference 3.1.

3.1.1 Vehicle Description

The two configurations to be considered are members of the biconic class. The forebodies are sharp, right-circular cones raked-off at an angle to provide the desired lift. The afterbodies are right elliptic cones. In flight, the forebody axis of symmetry is aligned with the relative wind vector. The

weight and volume of both vehicles are specified to be 10,000 lb and 1000 ft³, respectively. In the following discussions the vehicles will be distinguished by their forebody half-cone angles which are 28.5° and 26°. The lift to drag ratio and ballistic coefficient have been determined to be 0.5 and 122, respectively, for the 28.5° vehicle and 0.75 and 172, respectively for the 26° vehicle. The vehicle characteristics are summarized in Figure 3.1.

3.1.2 Entry Flight Mechanics

A trajectory model, characterized by constant-altitude deceleration subsequent to pullout, was adopted for this study. The characteristics of the trajectory model are illustrated in Figure 3-2 in terms of the altitude-velocity profile for the 28.5° vehicle entering at 57,000 ft/sec. From the reentry point, at 400,000 feet altitude, the pullout maneuver is negotiated with fixed roll angle. Roll programming is utilized subsequent to pullout to maintain constant altitude during which period the major portion of the deceleration is accomplished. When the roll attitude reaches zero degrees (maximum positive lift), the final descent begins along an equilibrium glide path.

Trajectories were computed for the two limiting reentry situations, i.e., entry along the upper and lower boundaries of the reentry corridor. These are referred to as the overshoot and undershoot trajectories respectively.

In the overshoot trajectory the vehicle enters with maximum negative lift reaching a zero flight path angle (pullout) when the lift force just balances the centripetal force. In the undershoot trajectory, the vehicle enters with full positive lift experiencing a 10g maximum resultant acceleration.

The character of the entry trajectory is grossly defined by the conditions at pullout. Since the major portion of heating occurs near pullout and in addition since surface Reynolds number is a maximum (for the constant altitude portion), the pullout trajectory conditions establish the important environmental regimes. The altitude and velocity at pullout for the fourteen tra-

jectories used in the present study are presented in Figure 3-3. It is seen that the dependence of pullout altitude on corridor position decreases significantly as the velocity is increased. Whereas pullout altitude may vary over a 60,000 ft range for entry at 36,000 ft/sec, the difference in pullout altitude between the overshoot and undershoot trajectories is only 10,000 ft at the highest entry velocities. The pullout altitude range is somewhat greater for the 26 deg cone than for the 28.5 deg cone as a consequence of lift/drag ratio differences. In the undershoot trajectory, the 26 deg cone descends to lower altitude during the pullout maneuver because of its greater ballistic coefficient. The two cones pullout at very nearly the same altitude in the overshoot trajectory since their lift-loading coefficients (W/C_{LA}) are about equal.

Pullout for these trajectories is generally accomplished in the altitude range where boundary layer transition might be expected. Figure 3-3 also shows the altitude velocity combinations for maximum surface Reynolds numbers (corresponding to the most rearward point on the conical forebody) of 5×10^6 and 1×10^6 . Some turbulent flow would occur in almost all entry situations if transition occurred at a Reynolds number of 1×10^6 . On the other hand, if boundary layer transition is assumed to occur at a Reynolds number of 5×10^6 , laminar flow would be predicted in all instances except for undershoot entry of the 26° vehicle at entry velocities below about 50,000 ft/sec. A Reynolds number of 5×10^6 was taken in this study as the maximum value for boundary layer transition. In order to determine the benefits obtained by maintaining a laminar boundary layer by increasing the pullout altitude, two additional trajectories were computed for the 26 deg cone; the entry velocities for these trajectories were approximately 35,000 ft/sec and 50,000 ft/sec.

3.2 AEROTHERMAL ENVIRONMENT

The heating rate experienced by an Earth entry vehicle is the result of a number of complex, coupled phenomena. Normally, the extremely high heating rates obtained from shock layer radiation and dissociated and ionized boundary

layer convection are associated with the stagnation region of blunt bodies. The case of a cone entering at speeds of the order of 50,000 ft/sec presents a situation where these so-called blunt body effects are present on a surface where the shock layer velocity is high and pressure is essentially constant. The cone problem is mathematically simpler than that for an axisymmetric stagnation point. However, there is somewhat less experimental information available on cone heat transfer at these speeds.

This section summarizes the methods used to determine the convective and radiative heat flux distributions for sharp cones traveling at superorbital speeds. Relations are presented which determine the shock layer radiation and convective heating accounting for the non-adiabatic nature of the inviscid, conical flow field. Boundary layer transition and mass injection effects on convection are treated. Transport property correlations are discussed.

In evaluating the thermal environment it is assumed that both the inviscid and viscous portions of the shock layer are in thermodynamic equilibrium.

The thermodynamic properties used in this study and the methods involved in obtaining them are presented in Reference 3.1. The thermodynamic state relations at high temperatures were defined using a free energy minimization IBM 7094 program assuming thermochemical equilibrium. The adopted emissivity model is a composite of the results of Nardone, Breene, et. al. (Reference 3.2) and Armstrong, et. al. (Reference 3.3) and represents an upper bound to the available computations. Transport properties are derived from Reference 3.4.

3.2.1 Shock-Layer Flow

Conditions Behind the Shock

The conditions immediately behind a conical shock are obtained from the usual oblique shock relations. The shock enthalpy, pressure, and velocity are

$$\rho = \frac{39.65}{ZT} \quad (3.7)$$

Conditions At The Boundary Layer Edge

Evaluation of the convective heat flux requires specification of the boundary layer edge conditions. The non-adiabatic character of the shock layer results in coupling of the inviscid and viscous flow fields. A reasonable approximation is to assume that the boundary layer edge pressure and velocity are unaffected by the radiation losses and are the same as obtained on the cone surface for inviscid, incompressible flow.

From Reference 3.5 the pressure is given by,

$$p_e = p_\infty + \frac{\rho_\infty u_\infty^2 \sin^2 \left(1 - \frac{3}{4} \epsilon\right)}{2116 q_c} \quad (3.8)$$

and the velocity is evaluated from Bernouilli's equation and Equations 3.2, 3.3 and 3.8,

$$u_e = u_\infty \left\{ 1 - \left(1 - \frac{\epsilon^2}{2}\right) \sin^2 \theta_s \right\}^{1/2} \quad (3.9)$$

In Reference 3.1 the enthalpy distribution through a conical, radiating, shock layer was derived. Assuming the boundary layer thickness is small in comparison to the shock layer thickness, the local boundary layer edge enthalpy is given by,

$$\frac{H_e}{H_s} = \left[1 + 2 \Gamma_c (\beta - 1) \right]^{\frac{-1}{\beta - 1}} \quad (3.10)$$

determined from the following equations,

$$H_S = H_\infty + \frac{U_\infty^2 \sin^2 \theta_s (1 - \epsilon^2)}{2 J g_c} \quad (3.1)$$

$$P_S = P_\infty + \frac{\rho_\infty U_\infty^2 \sin^2 \theta_s (1 - \epsilon)}{2.16 J_c} \quad (3.2)$$

$$U_S = U_\infty \left\{ 1 - (1 - \epsilon^2) \sin^2 \theta_s \right\} \quad (3.3)$$

where the density ratio is defined by,

$$\epsilon = \rho_\infty / \rho_S \quad (3.4)$$

The free stream density and pressure are known as a function of altitude. For hypervelocity speeds the shock layer is relatively thin and the assumption of a constant density shock layer is applicable. The cone solution given in Reference 3.5 yields the following equation for the shock angle,

$$\theta_s = \theta_c + \frac{\epsilon}{2} \tan \theta_s \quad (3.5)$$

The shock conditions are now determined by the simultaneous solution of Equations 3.1, 3.2, 3.4, 3.5 and the following state relations:

$$\begin{aligned} T &= f(H, P) \\ Z &= f(H, P) \end{aligned} \quad (3.6)$$

where the ratio of total radiation loss from an isothermal shock layer to the normal enthalpy flux is given by,

$$\Gamma_c = \frac{4 q_a}{\rho_\infty \left(u_\infty \sin \theta_s \right)^3 \left(\sqrt{q_c} \right)} \quad (3.11)$$

The adiabatic shock layer radiation towards the body is evaluated from the following expressions,

$$q_a = I_s \frac{\Delta a}{s} (s) \quad (3.12)$$

and the adiabatic shock-layer stand-off distance is given by Equation 3.4, or

$$\frac{\Delta a}{s} = \frac{1}{2} \epsilon \tan \theta_s \quad (3.13)$$

The radiation intensity per unit volume and the radiation power law exponent may be found in Reference 3.1 as a function of shock layer enthalpy and pressure,

$$I_s = f(H_s, P_s) \quad (3.14)$$

$$\beta = f(H_s, P_s) \quad (3.15)$$

3.2.2 Radiative Heat Transfer

As mentioned previously the methods of Reference 3.1 are used to define the shock layer radiation for a sharp cone. The non-adiabatic radiation flux to a conical surface is given by,

$$q_{sw}/q_a = \frac{1}{2 \Gamma_c^2 (\beta-1)} \left[\frac{1}{\beta-2} + q - \left(\frac{\beta-1}{\beta-2} \right) q^{\left(\frac{\beta-2}{\beta-1} \right)} \right] \quad (3.16)$$

where

$$q = 1 + 2 \Gamma_c (\beta-1)$$

The parameters \bar{c} , q_a and β are evaluated using Equations 3.11 through 3.15. The main assumptions employed in obtaining these relations are:

1) the radiative flux to the vehicle surface is due to shock-heated gas under thermodynamic and chemical equilibrium and 2) the shock layer is physically as well as optically thin. The consequences of neglecting non-equilibrium radiation, and radiation from the ablation products and of assuming the gas to be non-absorbing and gray are discussed in detail in Reference 3.1. In the present situation where the shock layer is thin and the heat flux is relatively low as compared to blunt body heating, boundary layer radiation may become significant. However, an investigation of the complex thermal and concentration boundary layers was not possible within the scope of this study.

3.2.3 Convective Heat Transfer

Determination of the convective heat transfer is complicated by the coupled nature of convection, radiation and ablation. As a first order approximation the radiation is accounted for by including radiation decay in evaluation of the boundary layer edge enthalpy, Equation 10. Ablation of the heat shield enters into the problem through the wall enthalpy, mass injection, surface erosion, and shape change. Shape change is not considered in the present study except with regard to nose blunting. The influence of wall enthalpy and mass injection are included by an iterative simultaneous solution of the analytical models for ablation and convection.

Flat plate incompressible solutions provide the foundation for the present predictions. These basic relations are first described and then corrections for compressibility, dissociation, conical geometry, and mass transpiration are introduced.

Basic Relations

The convective heat flux without surface mass injection is given by

$$q = h_0 (H_r - H_w) \quad (3.17)$$

The recovery enthalpy is defined as

$$H_r \equiv H_e + (r.f.) \frac{u_e^2}{2g_c J} \quad (3.18)$$

Where the laminar and turbulent recovery factors are given by \sqrt{Pr} and $\sqrt[3]{Pr}$ respectively and are approximately 0.84 and 0.89.

Solutions for the flat plate, incompressible heat transfer coefficient are given by the Blasius solution for laminar flow

$$h_{L0} = 0.332 \rho_e u_e Pr^{-2/3} Re_x^{-1/2} \quad (3.19)$$

and by the Colburn-Reynolds analogy relation for turbulent flow

$$h_{T0} = 0.0296 \rho_e u_e Pr^{-2/3} Re_{x'}^{-1/5} \quad (3.20)$$

where x' is the effective leading edge distance for turbulent flow.

Compressibility and Dissociation Correction

It has been well substantiated that the solutions for incompressible, undissociated, flow are applicable for the case of variable properties if the local thermodynamic properties are evaluated at an appropriate reference enthalpy which is defined by,

$$H^* = 0.22 H_r + 0.28 H_e + 0.5 H_w \quad (3.21)$$

At the temperatures of interest the air will be essentially a binary mixture of air atoms and molecules. The diffusion of these atoms towards the relatively cool surface with their subsequent recombination will tend to increase the con-

vective heat flux. Methods to account for this effect, such as using either a Lewis number correction term or by using total properties (properties which include both the molecular and chemical transport mechanisms) with the conventional heat transfer relations, have been proposed. However, it can be inferred from the results of Reference 3.6, that the aforementioned corrections are unnecessary when computing zero pressure gradient, laminar heat transfer when the boundary layer is in thermodynamic equilibrium. This conclusion for the case of a flat plate was based on a comparison of the heat transfer obtained from Equation 3.19 using frozen properties evaluated at the reference enthalpy with the results obtained from an exact similarity solution of the binary, reacting, boundary layer equations. The two methods yielded essentially identical results up to stagnation enthalpies corresponding to 29,000 ft/sec. The thermodynamic properties used in this investigation were those of Reference 3.7. In Reference 3.8 it was suggested that the diffusion phenomenon in a turbulent boundary layer would have the same relative effect on turbulent heating as on laminar heating. The basis for this supposition was that the influence of diffusion and chemical reaction on the boundary layer characteristics would be localized in the laminar sublayer. Experimental information presented in Reference 3.8 tended to substantiate their theory. Therefore, it appears that specific corrections for the influence of binary diffusion on laminar and turbulent heating need not be included at least up to ionization enthalpies.

Cone Correction

Since for identical free stream conditions the boundary layer at any point on a cone is somewhat thinner than the boundary layer on a flat plate, the flat plate coefficient must be modified. Transformation of the rotationally-symmetric boundary layer equations shows that the conditions within the boundary layer are identical at such locations on the flat plate and on the cone surface for which the cone Reynolds number is equal to three times that for a flat plate for laminar flow and twice for turbulent flow. Therefore, Equations 3.19 and 3.20 apply for a cone if the constants are multiplied

by $(3)^{1/2}$ and $(2)^{1/5}$ for laminar and turbulent flow, respectively.

The final equations for the non-blowing values of the laminar and turbulent heat transfer coefficient may now be expressed as:

Laminar:

$$h_{L0} = 0.575 C_L P_S^{-2/3} \left(\frac{\rho_S U_S U_e}{S} \right)^{1/2} \quad (3.22)$$

where the compressibility factor is given by,

$$C_L = \left(\frac{P_{rS}}{P_r^*} \right) \left(\rho^* \mu^* / \rho_S \mu_S \right)^{1/2} \quad (3.23)$$

Turbulent:

$$h_{T0} = 0.0340 C_T \left(\frac{S'}{S} \right)^{-1/5} \left(P_{rS} \right)^{-2/3} \left(\rho_S U_e \right)^{0.8} \left(\frac{\mu_S}{S} \right)^{.2} \quad (3.24)$$

where the turbulent compressibility factor is given by,

$$C_T = \left(\frac{P_{rS}}{P_r^*} \right)^{2/3} \left(\frac{\rho^*}{\rho_S} \right)^{.8} \left(\frac{\mu^*}{\mu_S} \right)^{.2} \quad (3.25)$$

The recovery factor is specified as 0.84 for laminar flow and 0.89 for turbulent flow.

Further verification of the convective heating methods used in the presented study is presented in the Appendix. Up to the onset of ionization, Equations 3.22 and 3.24 are shown to yield results which are in good agreement with those obtained from two recent studies concerning convective heating to cones at hypervelocity speeds.

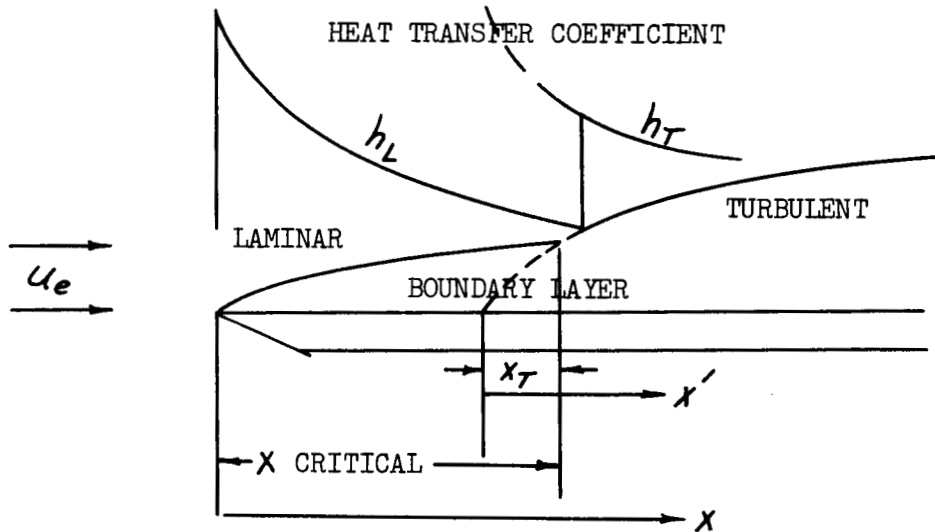
Transition

Transition from laminar to turbulent flow is a phenomenon which is not clearly

understood. It will be assumed here that a critical Reynolds number, based on boundary layer edge conditions and wetted length, can be used to specify the location on the surface where an abrupt transition from laminar to turbulent heating levels occurs. Critical values ranging from 2×10^5 to 5×10^6 will be considered.

Equation 3-20, for predicting turbulent heat transfer, is based on the assumption that turbulent flow exists at or very close to the leading edge. The equation should be corrected to account for the initial laminar run. An effective starting length for the turbulent boundary layer is therefore used. The following simple analysis will be used to obtain a first order approximation to the effective starting length.

Considering the boundary layer on a flat plate, the model is pictured below.



The effective length for turbulent flow is defined as x' where

$$x' = x - (x_c - x_T) \quad (3.26)$$

Since the transition Reynolds number, $Re_{critical}$, is presumed known,

$$x_c = \frac{Re_c}{Re U_e / \mu_e} \quad (3.27)$$

The length, x_T , can be prescribed if it is assumed that at the critical position the laminar momentum thickness equals the turbulent momentum thickness,

$$\theta_{L_{x_c}} = \theta_{T_{x_T}} \quad (3.28)$$

where the momentum thickness is defined by,

$$\theta \equiv \int_0^{\infty} \frac{\rho u}{\rho_e u_e} \left(1 - \frac{u}{u_e} \right) dy \quad (3.29)$$

It should be noted that any number of criteria of this type could be specified, all leading to slightly different results; for example, continuity of boundary layer thickness, energy thickness, or displacement thickness could be used. None of these methods has been shown to be superior or even valid. Continuity of momentum thickness is arbitrarily selected. For incompressible flow, Equation 3.28 can be expressed as,

$$0.664 \left(\frac{\mu}{\rho u_e} \right)^{1/2} x_c^{1/2} = 0.036 \left(\frac{\mu}{\rho u_e} \right)^{1/5} x_T^{4/5} \quad (3.30)$$

or solving for x_T ,

$$x_T = 38.2 \left(\frac{\mu}{\rho u_e} \right)^{3/8} x_c^{5/8} \quad (3.31)$$

Essentially the same equation is obtained for a cone by correcting the surface distance by $(3)^{1/2}$ and $(2)^{1/5}$, for laminar and turbulent flow, respectively. Evaluation of the properties at the reference enthalpy permits this relation to be applied to boundary layers with variable properties. Combining Equations 3.26 and 3.31 yields the following expression for the effective length for turbulent flow:

$$\frac{s'}{s} = 1 - \frac{s_c}{s} \left\{ 1 - 38 \left(\frac{\mu^*}{\rho^* u_e s_c} \right)^{3/8} \right\} \quad (3.32)$$

where

$$S_c = \frac{Re_c}{Re U_e / \mu_e} \quad (3.33)$$

In view of the considerable uncertainty in this method, it makes little difference if the reference conditions are replaced by the boundary layer edge conditions. Then, Equation 3.32 can be written as,

$$\frac{S'}{S} = 1 - \frac{S_c}{S} \left\{ 1 - 38 (Re_c)^{-3/8} \right\} \quad (3.34)$$

Mass Transfer Cooling

A considerable amount of information has become available recently concerning the influence of mass injection into the boundary layer on skin friction and convective heating. The phenomenon is of such complexity as to preclude the use of a relatively simple closed form relation for accurately predicting the reduction in convective heating for all possible environmental situations. In Reference 3.9 a comprehensive review of the available information was presented. This information was used to generate approximate relations for determining the effects of blowing on laminar and turbulent heating to stagnation and zero pressure gradient regions. Their expressions are particularly well substantiated for the situation of zero pressure gradient flow. (In applying the results of Reference 3.9 the specific heat ratio (ablation products to air) is approximated by the inverse of the molecular weight ratio.)

The heat transfer coefficient with mass injection for zero pressure gradient flow is then evaluated from Equations 3.35 and 3.36,

Laminar:

$$\text{for } \frac{\dot{m}}{h_0} \left(\frac{M_a}{M_c} \right)^{0.45} < 2.34$$

$$\left(h/h_0 \right)_L = 1 - 0.833 \frac{\dot{m}}{h_0} \left(\frac{M_a}{M_c} \right)^{0.45} + 0.178 \left\{ \frac{\dot{m}}{h_0} \left(\frac{M_a}{M_c} \right)^{0.45} \right\}^2 \quad (3.35)$$

$$\text{for } \frac{\dot{m}}{h_0} \left(\frac{M_a}{M_c} \right)^{0.45} > 2.34$$

$$\left(h/h_0 \right)_L = 0.02$$

Turbulent:

$$\left(h/h_0 \right)_T = \left[1 + \frac{1}{10} \frac{M_a}{M_c} \frac{\dot{m}}{h_0} \right]^{-4} \quad (3.36)$$

For the case of a charring ablator the surface mass flux is the sum of that derived from internal pyrolysis, \dot{m}_p and from char layer combustion, \dot{m}_c . The average molecular weight of the coolant or injectant is then given by

$$M_c = \frac{\frac{\dot{m}_p}{M_p} + \frac{\dot{m}_c}{M_c}}{\frac{\dot{m}_p}{M_p} + \frac{\dot{m}_c}{M_c}} \quad (3.37)$$

For nylon phenolic

$$M_p \approx 14$$

$$M_c \approx 27$$

Transport Properties

Essential to evaluation of the convective heating is an accurate knowledge of the transport properties of high temperature air. The thermodynamic properties of air have been determined accurately, but the transport properties present a problem because the interaction potentials are not well known. In the present study power law approximations of the transport properties predicted by Peng and Pindroh (Reference 3.4) were used. Their results were recommended for use in the critical review of Reference 3.10.

Both the viscosity and the Prandtl number are essentially independent of pressure for enthalpies less than 20,000 Btu/lb and pressures greater than 10^{-2} atmosphere. Hence, the transport properties may be expressed solely in terms of temperature. Correlation of the viscosity data yields the

following equation:

$$\mu = 1.85 \times 10^{-5} \left(\frac{T}{10^3} \right)^{.74} \text{ LB/FT-SEC} \quad (3.38)$$

Mathematical computations in evaluating the convective heating are considerably simplified if the density-viscosity products of Equations 3.23 and 3.25 are expressed analytically in terms of enthalpy. Correlation of the density-viscosity product at various pressure levels yields,

$$(\rho\mu)_p \propto H^{-0.32} \quad (3.39)$$

and

$$\left(\rho^{1/5} \mu^{1/5} \right)_p \propto H^{-0.51} \quad (3.40)$$

Since the pressure is essentially constant across the shock layer, Equations 3-23 and 3.25 may be rewritten as,

$$C_L = \left(\frac{P_{TS}}{P_T^*} \right)^{2/3} \left(\frac{H_S}{H^*} \right)^{.16} \quad (3.41)$$

$$C_T = \left(\frac{P_{TS}}{P_T^*} \right)^{2/3} \left(\frac{H_S}{H^*} \right)^{.57} \quad (3.42)$$

Equations 3.41 and 3.42 are sufficiently accurate for engineering purposes up to the onset of ionization (approximately 20,000 Btu/lb at 10^{-2} atm).

3.3 SHIELD REQUIREMENTS EVALUATION

The analysis procedures and fundamental data described in the foregoing sections have been applied to determine the aerothermal environment and subsequently the heat shielding requirements for the two biconic vehicles. The final results quantitatively indicate the influence of entry conditions, cone angle or ballistic coefficient and transition Reynolds number on shield weights for sharp cones entering the Earth's atmosphere at superorbital

velocities. The influence of additional mission parameters on heat shield weights may be qualitatively estimated from the results previously reported (Reference 3.1).

This section first describes the basic approach taken in analysis of heat shielding requirements. The computational procedure utilized in definition of the thermal environment and associated heat shield response is then indicated, and an example of the detailed information obtained in the process is given. The final results for heat shield weights are presented together with sufficient environmental information to explain behavioral trends.

3.3.1 General Approach

Study Cases

In this study two biconic configurations of fixed volume and weight were to be investigated for a range of entry velocities of both the undershoot and overshoot trajectories. The effects of transition criteria and air emissivity uncertainties were to be determined. It was also required that if during any trajectory the local Reynolds number exceeded 5×10^6 an additional calculation should be performed along a trajectory having a maximum Reynolds number of 5×10^6 . This requirement resulted in two additional trajectories. Early in the program it was determined that radiation constituted an insignificant factor in the evaluation of shield response. Therefore, emphasis has been given to the determination of the influence of entry condition and transition criteria on heat shield weight. The following table lists the cases considered in this study.

		STUDY CASES					
VEHICLE (HALF CONE ANGLE)		28.5			26°		
CRITICAL REYNOLDS NO.		2x10 ⁵	1x10 ⁶	5x10 ⁶	2x10 ⁵	1x10 ⁶	5x10 ⁶
ENTRY VELOCITY Ft/sec	CORRIDOR POSITION						
36,000	Upper Boundary	x	x	x	x	x	x
50,000	Upper Boundary	x	x	x	x	x	x
57,000	Upper Boundary	x	x	x	x	x	x
65,000	Upper Boundary				x	x	x
36,000	Lower Boundary	x	x	x	x	x	x
50,000	Lower Boundary	x	x	x	x	x	x
57,000	Lower Boundary	x	x	x	x	x	x
65,000	Lower Boundary				x	x	x
36,000	$R_{e_c} = 5 \times 10^6$ at P/O				x	x	x
50,000	$R_{e_c} = 5 \times 10^6$ at P/O				x	x	x

Each study case requires a detailed point-analysis of the aerothermal and material response of the vehicle throughout the trajectory. To insure an accurate description of the entire forebody all computations were performed at ten stations on the body.

Analysis Procedure

The analytical models for determining the aerothermal environment and shield thermal response have been indicated previously in Sections 3.2 and 2.0 respectively. In evaluation of heat shielding requirements these models represent the most rigorous techniques possible commensurate with the scope of this study. Their application required a high degree of automation. The relevant analytical expressions have been coded for use in two programs, ENVIRONMENT and TRANSIENT. While TRANSIENT is essentially the same program as used in the previous study (Reference 3.1), ENVIRONMENT is completely new. To reduce computer time the two programs have been coupled to form a single ENVIRONMENT-

TRANSIENT program.

With the selection of an entry case, trajectory and vehicle parameters are fed directly to ENVIRONMENT. This program then calculates instantaneous shock layer conditions, non-adiabatic radiation, local Reynolds numbers, and normalized values for the laminar and turbulent heat transfer parameters. (The heat transfer coefficients are normalized with respect to distance and the compressibility factor.)

The approximate technique of the TRANSIENT program yields results of good engineering accuracy for the heat shield thermal degradation history as indicated in Section 2. In the coupled program the results of ENVIRONMENT are automatically available to TRANSIENT which then computes instantaneous and total values for the surface recession, char thickness, and net heating. Several new features have been incorporated into this program as a consequence of the improved aerothermal environment determination. For example, a history of the critical distance, defined by the position where the local Reynolds equals the critical Reynolds number, is generated. This critical distance determines the effective starting length for turbulent flow.

Since the TRANSIENT program essentially uncouples the surface-recession and char-development problems from the virgin-material heat-conduction problem, additional methods must be employed to determine the thickness of shield material necessary for insulation of the substructure. As discussed in Section 2 the rigorous CHIRP formulation of the conduction equation may be used to accurately describe transient temperature response. Solutions generated by this program, however, require rather lengthy computation times. Fortunately, a considerable amount of information on insulation thicknesses using this program was obtained in the previous study (Reference 3.1). Extension of the results of the M1 and M2 vehicles to the present vehicles was considered to be warranted considering the similarity between the cone environmental conditions. Interpolation of the M1 and M2 results with respect to cone angle, entry conditions, and heating level yielded insulation

thicknesses for the present study cases.

Afterbody shield response also requires a rigorous CHIRP solution. Unfortunately, the afterbody environment is ill defined. Discussion of the methods involved in defining the afterbody heating may be found in Reference 3.1. Because of these uncertainties, recourse has again been made to the previous study. Extension of the M1 and M2 afterbody shield thickness to the present vehicles was made in the same manner as for forebody insulation thickness. It is expected that the afterbody radiation will be significantly lower for the case of a sharp cone, as compared to blunted cones, due to the lower static temperatures in the shock layer. Accordingly, the shield thicknesses obtained from the M1 and M2 vehicles are reduced slightly for the higher velocity cases in an attempt to correct for the reduced radiation. The possible errors incurred in prediction of afterbody shield thickness are considered relatively small in comparison to the total heat shielding requirements.

In all shield requirements computations a substructure having a thermal capacitance of $0.5 \text{ Btu/}^{\circ}\text{F}$ has been assumed. A maximum allowable temperature for the substructure of 500°F has been prescribed. A nominal value of 70°F has been taken for the temperature of the heat shield at time of entry. Shield thicknesses have been computed for a nylon-phenolic composite (equal proportions of nylon and phenolic by weight) having a density of 75 lbm/ft^3 .

3.3.2 Results

The aerothermal environment, material thermal response, and heat shield weights have been determined for both biconic vehicles for various entry conditions and transition Reynolds numbers. The specific situations studied and the resulting forebody and afterbody weights are given in Table 3-1. In this section these results are discussed with respect to the contributing environmental conditions. First, typical aerothermal results are examined as an aid in understanding the trends to be pointed out subsequently. Second, examples of material degradation

histories and distributions are presented to illustrate the environment-material response relationship. Finally, forebody heat shield weights are examined with respect to the influence of 1) cone angle, 2) entry conditions, and 3) transition criteria. Comparison of the total vehicle weights is also made with the vehicles considered in Reference 3-1.

Information Generated

The aerothermal environment and material thermal response for a typical case will be described here. The case which is considered is entry of the 28.5° vehicle along the overshoot trajectory at a velocity of 57,000 ft/sec. The entry trajectory is described in Figure 3-2. The environment associated with this entry case is of intermediate severity relative to the spectrum of cases considered.

The convective and radiative heat transfer histories for two values of the critical Reynolds number are described in Figures 3-4 and 3-5 for the 5 ft. station on the conical forebody. The corresponding history of the critical distance (location where local Reynolds number equals the transition Reynolds number) is shown in Figure 3-6. For the 5 ft. station the flow is laminar throughout the trajectory for a transition Reynolds number of 5×10^6 while for a value of 2×10^5 the flow at the 5 ft. position is turbulent for all but the first 45 seconds. Transition substantially increases the thermal load as evidenced by the increase in peak cold wall heating from 660 Btu/ft² sec to 2000 Btu/ft² sec for transition Reynolds numbers of 5×10^6 and 2×10^5 , respectively. This large increase is partly attributable to the effective turbulent starting length moving back from the tip. Including the influence of blowing tends to increase the significance of transition. The greater efficiency of mass injection into the laminar boundary layer accounts for this effect.

Figure 3-4 indicates that convection is by far the predominant heat transfer mechanism for the stated situation. A similar result was obtained in all

other cases. Radiation is insignificant for the complete range of entry conditions due to the small cone angles of the vehicles investigated in this study. The strong influence of cone angle on radiation is illustrated in Figure 3-7. These results, which were obtained in Reference 3.11, indicate that for entry velocities less than 65,000 ft/sec, the radiation is significant only for cone angles greater than 30° .

Material degradation histories derived from the two previously discussed thermal environment histories are shown in Figures 3-8 and 3-9. The insets describe the surface temperature histories. Surface recession rate resulting from chemical reaction of the char with air species is substantially higher for the case of turbulent flow as depicted in Figure 3-8. This is attributable to diffusion rates of air reactants to the surface being relatively higher (due in part to the transpiration effect). With increased heating rates and attendant high surface recession rate, high temperature gradients are required to conduct the heat into the interior; consequently higher surface temperature and a thinner char layer are obtained. For laminar flow, surface temperature is significantly lower and the char layer is relatively thick.

Typical results for the required heat shield thicknesses are presented in Figures 3-10 and 3-11. The variation over the surface of the depth of material degradation reflects the variation of convective heat flux levels, but is not directly related due to the rather complex behavior of nylon phenolic. For a critical Reynolds number of 2×10^5 , transition was found to occur essentially one foot back of the tip with a subsequent increase in total surface recession. Total surface recession for laminar flow is of the order of one-tenth that obtained with turbulent heating. Conversely, laminar heating results in slightly increased insulation and char thicknesses relative to turbulent flow. (The "insulation thickness" is the amount of virgin material remaining at the end of the heating period which is required to maintain the substructure below the allowable temperature of 500°F .) Char and insulation thicknesses do not vary markedly over the forebody when the flow regime is fixed, but they do constitute a substantial portion of the total. As might

be expected total shield thickness are larger for turbulent flow; at the 10 ft. station the thickness is 1.7 inches for turbulent flow and .85 inches for laminar.

Shielding Requirements

The forebody and afterbody shield weights for all situations considered are summarized in Table 3-1. As a result of the uncertainties associated with the afterbody weights the emphasis is placed on describing the forebody shielding requirements. The influence of entry conditions and transition criterion on the forebody weights is quantitatively defined. Finally, total vehicle shield weights are compared with those obtained in the previous study (Reference 3.1).

Variation of forebody shield weight with entry velocity for both the undershoot and overshoot trajectories is shown in Figures 3-12, 3-13 and 3-14 for transition Reynolds numbers of 5×10^6 , 1×10^6 and 2×10^5 , respectively. Thermal protection requirements are seen to increase slowly and almost linearly with entry velocity for all cases. This relatively weak dependence on entry velocity is attributable in part to 1) the lack of radiation and 2) the increased blocking of convective heating by the ablation gases at the higher velocities.

For similar entry conditions and transition criteria the 26° vehicle required the greater shielding for the situations studied. This is primarily a result of the increased re-entry time (or heating period length) which arises with increase in lift to drag ratio.

The influence of corridor position on shield requirements is somewhat more complex. A change in corridor position affects not only the duration of heating but also the occurrence of turbulent flow. The degree to which transition is influenced by entry velocity and corridor position can be inferred from Figure 3-3. If a critical Reynolds number of 5×10^6 is used the boundary

layer on the vehicle will be entirely laminar for most of the entry conditions studied. Conversely, if a value of 2×10^5 is selected turbulent flow will dominate. In these two situations, trajectory duration is the controlling factor as evidenced by Figures 3-12 and 3-14 where re-entry along the overshoot trajectory requires the greater thermal protection. Specification of a critical Reynolds number of 1×10^6 results in an overlap between the degree and length of heating. For example, consider the 26° vehicle at a pull-out velocity of 35,000 ft/sec. The boundary layer is essentially laminar over the entire forebody at pull-out for the overshoot trajectory, while for the undershoot trajectory approximately the last 20% of the forebody is turbulent. This interrelationship of corridor position and transition is evidenced in the heat shielding requirements shown in Figure 3-13. For entry velocities in excess of 40,000 ft/sec the shield weights are greater for the undershoot trajectory as the effect of turbulent heating predominates over the longer heating pulse associated with the overshoot trajectory.

The influence of transition uncertainty on forebody heat shielding requirements is summarized in Figures 3-15 and 3-16. The increase in required weight occurring with reduction of the assumed critical Reynolds number from 5×10^6 to 1×10^6 is large; shield weights are increased roughly by a factor of 2. Further reduction in the Reynolds number below 1×10^6 is not as damaging since turbulent heating is already the dominant mechanism for a majority of the cases. Exceptions to this occur for the lower entry velocities along the overshoot trajectory where laminar flow may persist at critical Reynolds numbers of 2×10^5 .

A comparison of the shielding requirements for the two biconic vehicles with those for the configurations considered in the previous study (Reference 3.1) is presented as a function of entry velocity in Figure 3-17. The transition Reynolds number for the biconic vehicles was selected as 5×10^6 , while for the other vehicles the value is approximately 2×10^5 . In each case, vehicle volume and weight are taken as 1000 ft³ and 10,000 lb. The band for each configuration indicates the possible variation arising from movement within

the entry corridor. Shield weights for the 28.5° vehicle slightly exceed those obtained for the M1 configuration whereas shielding requirements for the 26° vehicle are about 20 per cent higher. Shield weights for the M2 configuration are substantially larger than for the biconic vehicles, reflecting the effect of turbulent heating on the conical section. A more conservative transition criterion, such as a critical Reynolds number of 2×10^5 , would tend to make the two biconic vehicles comparable to the M2 configuration. The two biconic vehicles investigated in the present study appear to be attractive for velocities in excess of 57,000 fps, particular if the transition Reynolds number is greater than 5×10^6 .

3.4 NOSE BLUNTING EVALUATION

The heat shield weights for the two configurations of interest have been determined under the assumption that the nose tip remains sharp. In reality, some degree of nose blunting will occur with consequent perturbation of cone heating levels and shield material thickness requirements. In order to determine the error introduced by the sharp tip assumption, the extent of nose blunting has been quantitatively evaluated and the influence on the cone heating and material requirements has been indicated.

The approximate procedure used for determining the course of nose tip ablation is described in the following section. Stagnation point radiative and convective heating are evaluated for either of two limit tip geometries, hemispherical or flat faced. Tip radius variation with time is determined neglecting recession of the conical surface. Rate of material erosion is calculated using the quasi-steady ablation formulae described in Reference 3.1. A detailed point-analysis procedure is used in evaluating the history of the nose tip radius throughout the re-entry trajectory. Due to the complexity of the problem and the large number of computations required the pertinent relations describing environment and material response were programmed for digital computer application.

Histories of the nose tip radii, assuming both hemispherical and flat geometries, were obtained for both of the biconic vehicles over the 12 primary trajectories discussed in Section 3.1. These results will be discussed following an explanation of the evaluation procedure. Finally the influence of nose bluntness on cone heating and heat shield requirements will be assessed.

3.4.1 Aerothermal Environment

The environmental conditions to which even fixed geometry blunt vehicles are subjected are complex. Evaluation of the blunt nose heating requires describing both the radiative and convective heating distributions, accounting for the interaction between the modes of heating and the ablation mechanism. Several rather severe approximations are introduced to make the analyses more tractable. The conical surface is assumed fixed and the nose shape is approximated by either of two limit configurations, hemispherical or flat faced. The advantages in such restrictions are obvious: (1) nose radius is a function of the stagnation point recession only and (2) the aerothermal environment is relatively well defined for these two geometries.

Physically, the nose geometry will be neither flat or spherical. The actual shape will have a transient behavior governed by the interrelationship between the aerothermal environment and surface configuration. The problem is of such complexity as to preclude a quantitative analysis of the geometrical response. For example, the rapid decay associated with convective and radiative heating distributions on a hemisphere would indicate that a considerable flattening would occur. Conversely, the heating experienced by the conical surface near the nose-cone intersection, particularly in the case of a flat nose, has a tendency to round the nose. The simplest recourse is to treat the two limit configurations, hemispherical and flat faced, separately.

Evaluation of the aerothermal environment is therefore reduced to describing the stagnation point convective and radiative heating for the two limit tip

geometries. The definition of the high temperature properties of air was discussed in Section 3.2. Similarly, the cone relations for determining the conditions behind the shock are valid for the stagnation region if the shock angle is set equal to 90° . In this section the procedures used in calculating the stagnation point convective and radiative heat transfer are discussed.

Hemispherical Nose

The convective and radiative heating to a spherical stagnation region is evaluated using the methods described in Reference 3.1. In particular, the adiabatic shock layer radiation towards the body is determined using the expression

$$q_a = I_s \Delta a \quad (3.43)$$

and the shock layer stand-off distance is given by the constant density solution of Reference 3.5:

$$\frac{\Delta a}{R_{eff}} = \frac{\epsilon}{1 + \sqrt{\frac{4}{3}} \epsilon - \epsilon} \quad (3.44)$$

The effective radius is equal to the nose radius when considering a spherical nose. The non-adiabatic radiation flux, as derived in Reference 3.1 for the stagnation region, is given by Equation 3.45,

$$q_{sw}/q_a = \int_0^1 \left[1 - \Gamma_{SN}(\beta-1) \ln \eta \right]^{-\frac{\beta}{\beta-1}} d\eta \quad (3.45)$$

where the dimensionless shock layer distance is defined by

$$\eta = y_a / \Delta a \quad (3.46)$$

and the ratio of total radiation loss from an isothermal shock layer to the normal flux is given by

$$\Gamma_{SN} = \frac{4 q_a}{\rho_\infty u_\infty^3} \quad (3.47)$$

The radiation intensity per unit volume and the radiation power law exponent are found as a function of shock layer enthalpy and pressure in Reference 3.1.

The stagnation point convective coefficient is calculated from the expression,

$$h_0 = 2.2 \rho_\infty^{0.5} \left(\frac{u_\infty}{10^4} \right)^{1.19} \left(\frac{1}{u_\infty} \frac{du_e}{ds} \right)^{1/2} \quad (3.48)$$

where $\frac{1}{u_\infty} \frac{du_e}{ds} = \left[(2-\epsilon)(\epsilon) \right]^{1/2} R_{eff}^{-1}$ (3.49)

which is a modified form of the Hoshizaki equation.

Flat Faced Nose

The aerothermal environment for a flat-faced stagnation region differs considerably from that experienced by a spherical nose. The shock stand-off distance is significantly larger for the flat configuration. Conversely, the stagnation region velocity gradient is reduced. Consequently, radiation will be increased and convection reduced relative to the spherical nose.

The incompressible inviscid flow around various bodies of revolution was considered by Vinokur in References 3.12 and 3.13. Results included shock layer stand-off distance and velocity gradients for both spherical and flat faced stagnation regions. The flat face results are adequately correlated by use of an effective nose radius in Equation 3.44 and 3.49

$$R_{eff} = 7.0 R_{FLAT NOSE} \quad (3.50)$$

Shock stand-off distances and velocity gradients calculated using the above definition differ by no more than 6% from those given by Vinokur.

3.4.2 Material Thermal Response

The model adopted for describing the surface recession history at the tip

was the quasi-steady ablation model defined in Section 2.0. The assumption of quasi-steady material behavior affords substantial reduction of machine time as compared to the more rigorous solutions. Since the major nose geometry change will occur during the period of peak heating when the rate of change of the thermally effected zone is small relative to the rate of surface recession, the assumption of quasi-steady behavior is a valid approximation.

3.4.3 Extent of Nose Blunting

The aforementioned analysis techniques have been applied to determine the extent of nose blunting in all cases for which cone shielding requirements were evaluated.

This section first describes the numerical procedure utilized in evaluating nose bluntness histories. Examples of environmental conditions and the resulting nose radius histories are then presented and, finally, all nose blunting results are summarized.

Numerical Procedure

The general approach utilized in describing the time dependent nose radius is straight forward. Since the cone surface is fixed and nose geometry is constant the nose radius is uniquely related to the surface recession history by the following expressions:

1. Flat Faced Nose

$$R_{FN} = \tan \theta_c \int_0^{\tau} \dot{s}_0 d\tau \quad (3.51)$$

2. Spherical Nose

$$R_{SN} = \frac{\int_0^{\tau} \dot{s}_0 d\tau}{\frac{1}{\sin \theta_c} - 1} \quad (3.52)$$

Given the appropriate trajectory information it is only necessary to describe the forebody half cone angle, nose geometry and an initial value for the nose radius. The trajectory is divided up into small time increments. Holding the radius constant over each time step, the aerothermal environment and associated material response are evaluated. Integrating the surface recession rate over the time step yields a new value for the nose radius. This procedure is then repeated for the next time step. A high degree of accuracy in such a method requires both a small initial radius and a small time step. To handle the numerous computations in a point analysis technique of this type requires a high degree of automation. Accordingly, the above procedure has been programmed for digital computer application.

Prior to computing all nose radius histories, the influence of initial radius and time step were evaluated. Calculation of the spherical nose history for the 28.5° vehicle entering at 57,000 ft/sec along the overshoot trajectory was used as a test case. The initial nose radius was varied from 10^{-2} to 10^{-4} ft. with time steps of .1 sec. and 5 sec. In all cases the nose radii converged to essentially the identical value by the time of peak heating, approximately 80 sec. In the remaining cases values of 10^{-4} ft. and 5 sec. were selected for the initial radius and time step, respectively.

Information Generated

In evaluating the extent of nose blunting it is useful to indicate the associated aerothermal environment. The stagnation point heating histories and nose radii response for a typical case are presented here as an aid in understanding the trends to be pointed out subsequently. The case which is considered is entry of the 28.5° vehicle along the overshoot trajectory at a velocity of 57,000 ft/sec. Both nose geometries are considered.

Stagnation point heating histories are shown in Figure 3-18. It is apparent that as a result of the small nose radius, convective heating is initiated almost as soon as entry commences. (The convective heating is initially

overestimated since continuum flow equations, rather than free molecular relations, are used throughout). The cold wall convection then increases rapidly until the increased nose bluntness causes it to peak prematurely (see Figure 3.4) by about 20 seconds. The spherical nose with its steeper velocity gradient has a substantially higher convective flux relative to the flat geometry. Conversely, the flat nose experiences a larger radiative flux due to a thicker shock layer. Although convection appears to dominate, including the influence of mass injection results in convective and radiative fluxes of comparable magnitude.

The associated nose radius histories are presented in Figure 3-19. Assuming a spherical geometry, a radius of 2.55 inches is achieved in 200 sec. while for the flat faced nose the radius is 1.1 inches. Associated values for the total surface recession are 2.8 inches and 2.0 inches for spherical and flat face geometries, respectively. The indication is that convection exerts a slightly greater influence on the course of blunting at this entry velocity.

Nose Bluntness

The results obtained in investigating the extent of nose blunting are summarized in Table 3-1 and in Figures 3-20 and 3-21. Nose radii for a time of 200 sec. after entry are presented as a function of entry velocity. (At 200 sec., the bulk of the entry heat load has been accepted and hence further surface recession will be relatively small. The calculations were not continued beyond 200 seconds since the quasi-steady ablation assumption becomes poor at low heating levels.) Results for the two corridor positions and both tip geometries are shown. There appears to be only a weak dependence of nose radius on corridor position; the nose radius for the undershoot trajectory with its higher heating rates is generally larger. For entry velocities less than 57,000 ft/sec convection is the dominant mode of heating as evidenced by the almost linear dependence of radius on entry velocity. At velocities in excess of 57,000 ft/sec radiation rapidly dominates and nose radii increase accordingly. Increasing entry velocity from 57,000 ft/sec to 65,000 ft/sec

results in an increase in the flat nose radius from roughly 2 inches to 12 inches while the spherical radius increases from about 3 inches to 6 inches. Evidently, the influence of tip geometry and entry velocity on bluntness are especially significant at the higher entry velocities.

3.4.4 Influence of Nose Blunting

As a consequence of nose tip blunting there will be a perturbation of the cone environment and heat shield response. Conical surfaces downstream of the nose may be expected to experience an increased radiative flux as a result of the local shock layer being partly fed from the bow-shock wave. The character of the boundary layer is also altered as it entrains the vortical layer emanating from the curved shock wave. The intent here is to assess the effect that blunting has on the previously described material requirements for sharp cones.

The influence of nose radius on the cone thermal environment can be inferred from Figures 3-22, 3-23 and 3-24. Figure 3-22 was obtained from Reference 3.11 and depicts the relationship between nose radius and radiation distribution. For the environmental conditions investigated, the influence of bluntness on cone radiation is restricted to the first 20% of the forebody for radii less than one foot. This effect can be expected to persist slightly further downstream for more slender cones, such as those investigated in this study. A similar conclusion is reached when considering the effect of vorticity. The laminar and turbulent heat transfer distribution factors (local to stagnation heat transfer coefficient ratio) are shown in Figures 3-23 and 3-24 respectively, as a function of the "vorticity parameter" defined in Reference 3.1. It is of interest to indicate the magnitude of the vorticity parameter for the present study. As an example, consider the 28.5° vehicle entering at 57,000 ft/sec along the overshoot trajectory. At approximately the time of peak heating, values of the laminar and turbulent vorticity parameters for a 3 inch radius sphere are .036 and .63, respectively. Consequently the convective heating will essentially decay to its sharp cone value in about the first 20 inches.

With the exception of the 65,000 ft/sec entry case, the blunting of the cone vehicles will be restricted to a radius of roughly 3 inches during the major portion of the heating period. Nose radii, the order of 6 inches, might be expected for 65,000 ft/sec entry at about the time of peak heating. It is apparent from the previous discussion that blunting of this degree will have little effect on the cone thermal environment and associated material requirements. Perturbations in heating rates will in general be restricted to only the initial portion of the forebody. Therefore, the previously determined heat shield weights are applicable even under the conditions of nose blunting.

REFERENCES

- 3.1 "Study of Heat Shielding Requirements for Manned Mars Landing and Return Missions - Final Report," IMSC 4-74-64-1, Dec. 1964.
- 3.2 Nardone, M., Breene, R. G., Zeldin, S. and Riethof, T. R., "Radiance of Species in High Temperature Air," Space Science Laboratory, General Electric Co., R63SD3, 1963.
- 3.3 Armstrong, B., Buttrey, D., Sartori, L., Siegert, A. J. F. and Weisner, J., "Radiative Properties of High Temperature Gases," AFSWC-TR-61-72, Lockheed Missiles and Space Co., 1961.
- 3.4 Peng, T. C., and Pindroh, A. L., "An Improved Calculation of Gas Properties at High Temperatures: Air," Document No. D2-11722, The Boeing Company, 1962.
- 3.5 Hayes, W. D., and Probstein, R. F., "Hypersonic Flow Theory," Academic Press, New York, 1959.
- 3.6 Cohen, Nathaniel B., "Boundary-Layer Similar Solutions and Correlation Equation for Laminar Heat Transfer Distribution in Equilibrium Air at Velocities up to 41,000 Feet per Second," NASA TR R-118, 1961.
- 3.7 Hansen, C. Frederick, "Approximations for the Thermodynamic and Transport Properties of High-Temperature Air," NASA TR R-50, 1959.
- 3.8 Rose, P. H., Probstein, R. F., and Adams, M. C., "Turbulent Heat Transfer Through a Highly Cooled, Partially Dissociated Boundary Layer," JAS, Dec. 1958, pp. 751-760.
- 3.9 Woodruff, L. W., "Transpiration Effects on Heat Transfer," Document No. D2-22202, The Boeing Company, 1962.

- 3.10 Regent, B., and Nobal, C. E., "High Temperature Transport Coefficients of Selected Gases - A Compilation and Review", Report No. 52, Vidya Corp., Sept. 1, 1961.
- 3.11 Hearne, L. F., Chin, J. H., and Lefferdo, J. M., "Reentry Heating and Thermal Protection of a Mars-Mission Earth-Reentry Module", AIAA Entry Technology Conference, Williamsburg & Hampton, Va., Oct. 12-14, 1964.
- 3.12 Vinokur, M., "The Distribution of Velocity, Pressure, and Laminar Heat Transfer on Blunt Bodies in Hypersonic Flow," Aerophysic Technical Note 3, IMSC 894815, 1961.
- 3.13 Vinokur, M., "Inviscid Hypersonic Flow Around Blunt Bodies," LMSD 48454, 1959.
- 3.14 Chapman, G. T., "Theoretical Laminar Convective Heat Transfer and Boundary-Layer Characteristics on Cones at Speeds to 24 KM/Sec," NASA TN D-2463, 1964.
- 3.15 Allen, J. H., Seiff, A., and Winovich, W., "Aerodynamic Heating of Conical Entry Vehicles at Speeds in Excess of Earth Parabolic Speed", NASA TR R-185, 1963.

NOTATION

C	Compressibility factor
g_c	Gravitational constant, $32.17 \text{ lb}_m\text{-ft/lb}_f\text{-sec}^2$
h	Heat transfer coefficient, $\text{lb}_m/\text{ft}^2\text{-sec}$
H	Enthalpy, Btu/lbm
I	Radiation intensity per unit volume, $\text{Btu/ft}^3\text{-sec}$
J	Energy conversion constant, $778 \text{ ft}\cdot\text{lb}_f/\text{Btu}$
Nu	Nusselt number
p	Pressure
Pr	Prandtl number
q	Heat flux rate, $\text{Btu/ft}^2\text{-sec}$
R	Radius, inches
Re_s	Local Reynolds number
r.f.	Recovery factor
s	Distance along body surface, ft
\dot{s}	Surface recession rate, in/sec
T	Temperature, $^{\circ}\text{R}$
u	Velocity, ft/sec
x	Distance along flat plate, ft
y	Distance normal to surface, ft
Z	Compressibility function

β	Radiation power law exponent
Γ	Ratio of isothermal to normal shock layer radiation
ϵ	Density ratio across shock
Δ_a	Adiabatic shock layer thickness, ft
η	Dimensionless shock layer distance
ρ	Density, lb _m /ft ³
θ	Conical half angle, radians; momentum thickness
μ	Coefficient of viscosity, lb _m /ft-sec
τ	Time, sec

SUBSCRIPTS:

a	Adiabatic
c	Cone
e	Boundary layer edge
eff	Effective nose radius
FN	Flat faced nose
L	Laminar
l	Surface length
r	Recovery
s	Shock
SN	Spherical Nose
St	Stanton number
sw	Shock layer radiation to surface
T	Turbulent; transition; total
w	Wall
∞	Free stream

o Zero mass injection; stagnation conditions

SUPERSCRIPTS:

* Reference

/ Reference; total properties; effective length

- Average

Appendix 3A

COMPARISON OF METHODS FOR EVALUATING CONVECTIVE HEAT TRANSFER

The techniques utilized in the present study for evaluating the laminar and turbulent heating are described in Section 3.2. These methods are based on well defined analyses of low speed flat plate flow. Extrapolation to high speed flow is accomplished using the "reference enthalpy" and "recovery enthalpy" to account for compressibility and frictional dissipation, respectively. Application of flat plate results to cone flow relies on boundary layer analyses which have shown that convective heating for the two situations differ by a constant factor.

Since convection is of such importance in the present study it is of interest to compare the methods of this investigation with other evaluation procedures. Accordingly, two recent reports which analyse laminar and turbulent cone heating, were selected for comparison purposes. Reference 3.14 describes the results of a detailed solution of laminar convective heating on cones at hypervelocity speeds. Exact solutions of the conical boundary layer equations for a dissociating and ionizing gas in equilibrium were used to generate heat transfer and skin friction parameters for a variety of free stream and wall conditions. Simple correlations were obtained from this information. The turbulent analysis of Reference 3.15 is identical in nature to that employed in the present study. The turbulent heat transfer relation was derived by use of Colburn's modified Reynolds analogy and the reference enthalpy method. The major difference between the two approaches lies in the selection of the incompressible skin friction law. In the following section the methods employed in this study are compared with those of References 3.14 and 3.15.

LAMINAR CONVECTIVE HEAT TRANSFER

In Reference 3.14 the heat transfer results were correlated by the equation,

$$\frac{Nu}{\sqrt{Re_w}} = A (U_{\infty})^{-B} \quad (3.53)$$

where $Nu \equiv \frac{q_s Pr'_w}{(H_T - H_w) \mu_w}$ (3.54)

$$Re_w \equiv \frac{\rho_w U_{\infty} s}{\mu_w} \quad (3.55)$$

The prime denotes that the transport properties are total properties (i.e., they include the chemical reaction terms). As a specific example the case corresponding to

$$\begin{aligned} P_e &= 1 \text{ ATM} \\ T_w &= 3000^\circ \text{K} \end{aligned} \quad (3.56)$$

will be considered. Then

$$\begin{aligned} A &= 0.810 \\ B &= 0.360 \end{aligned} \quad (3.57)$$

The relation used in the present study for predicting the laminar heat transfer is given by,

$$q = 0.575 \left(P_e^* \right)^{-2/3} \left(\frac{\rho^* \mu^* U_e}{s} \right)^{1/2} (H_T - H_w) \quad (3.58)$$

To enable this equation to be put into a form comparable with Equation 3.53 the following approximations are made:

1. $H_r = H_T$
2. At the wall conditions of interest, chemical reaction terms are negligible in determining the transport properties

Equation 3.58 can then be written in the form,

$$\frac{Nu}{\sqrt{Re_w}} = 0.575 \frac{P_w}{(P_r^*)^{2/3}} \left(\frac{\rho^* \mu^*}{P_w \mu_w} \right)^{1/2} \quad (3.59)$$

To be consistent with the solution of Reference 3.14 the properties of Hanson (Reference 3.7) are used in evaluating Equation 3.59. A comparison of Equations 3.53 and 3.59 is presented in Figure 3-25. Cone angles of 15° and 60° are treated for a range of velocities. The agreement between the methods of this study and that of Reference 3.14 is good up to the onset of ionization.

TURBULENT CONVECTIVE HEAT TRANSFER

Turbulent convection was predicted in Reference 3.15 using the equation,

$$\overline{St} = \frac{.0166}{(Re_l')^{.148}} \frac{P'}{P_e} P_{rw}^{-2/3} \quad (3.60)$$

where $\overline{St} \equiv \frac{\bar{h}}{P_e U_e} \quad (3.61)$

\bar{h} = average heat transfer coefficient for the cone surface

$$Re_l' = \frac{\rho' U_e l}{\mu'} \quad (3.62)$$

$l = \text{CONE LENGTH}$

the prime denotes evaluation at the reference enthalpy condition, where,

$$H' = .375 H_e + .175 H_f + .45 H_w \quad (3.63)$$

Any influence of the initial laminar run before transition was not included. The local heat transfer coefficient in the present study was evaluated from

$$h = .034 (P_r^*)^{-2/3} (\rho^* U_e)^{.28} \left(\frac{\mu^*}{S} \right)^{.2} \quad (3.64)$$

To be consistent, the boundary layer is assumed to be turbulent at the cone tip. This equation can be rewritten in terms of the average Stanton number,

$$\overline{St} = \frac{.0378}{(Re^*)^{0.2}} \frac{\rho^*}{\rho_e} (Pr^*)^{-2/3} \quad (3.65)$$

Equations 3.60 and 3.65 are directly comparable with the following exceptions:

1. the slight difference in the definition of the reference enthalpy
2. the Prandtl number is evaluated at different conditions

Neglecting the difference in the definition of the reference enthalpy, Equations 3.60 and 3.65 are presented in Figure 3-26. The band indicates the possible variation in the Stanton number of Equation 3.65 resulting from the spectrum of conditions at which the Prandtl number can be evaluated. The difference in slope between the two methods is attributable to the particular skin friction relations from which they were derived. The extension of flat plate results to a conical surface accounts for the discrepancy in magnitude. In Reference 3.15, cone heating was taken to be 4.7% higher than flat plate convection, while a value of 15% was used in the present study. Evaluating Equation 3.60 using the latter value yields results which are in good agreement with those of the method used in this study.

TABLE 3-1
HEAT SHIELD WEIGHT REQUIREMENTS SUMMARY

VEHICLE	V _E (ft/sec)	CORRIDOR POSITION	FLAT NOSE RADIUS AT 200 SEC. (INCHES)	SPHERICAL NOSE RADIUS AT 200 SEC. (INCHES)	CRITICAL REYNOLDS NUMBER	FOREBODY HEAT SHIELD WEIGHT (lbx10 ³)	AFTERBODY HEAT SHIELD WEIGHT (lb)
28.5° Cone	36,000	Overshoot	.386	1.108	5x10 ⁶	1.79	508
28.5° Cone	36,000	Overshoot			1x10 ⁶	1.95	
28.5° Cone	36,000	Overshoot			2x10 ⁵	2.80	
28.5° Cone	50,000	Overshoot	.808	2.167	5x10 ⁶	1.97	551
28.5° Cone	50,000	Overshoot			1x10 ⁶	2.37	
28.5° Cone	50,000	Overshoot			2x10 ⁵	3.49	
28.5° Cone	57,000	Overshoot	1.079	2.561	5x10 ⁶	2.04	578
28.5° Cone	57,000	Overshoot			1x10 ⁶	2.84	
28.5° Cone	57,000	Overshoot			2x10 ⁵	3.95	
28.5° Cone	36,000	Undershoot	.603	1.672	5x10 ⁶	.952	262
28.5° Cone	36,000	Undershoot			1x10 ⁶	1.74	
28.5° Cone	36,000	Undershoot			2x10 ⁵	1.82	
28.5° Cone	50,000	Undershoot	.896	2.355	5x10 ⁶	1.47	497
28.5° Cone	50,000	Undershoot			1x10 ⁶	2.59	
28.5° Cone	50,000	Undershoot			2x10 ⁵	2.95	
28.5° Cone	57,000	Undershoot	1.220	2.750	5x10 ⁶	1.74	578
28.5° Cone	57,000	Undershoot			1x10 ⁶	3.09	
28.5° Cone	57,000	Undershoot			2x10 ⁵	3.65	

26° Cone	36,000	Overshoot	.387	1.072	5x10 ⁶	2.05	622
26° Cone	36,000	Overshoot			1x10 ⁶	2.18	
26° Cone	36,000	Overshoot			2x10 ⁵	3.18	
26° Cone	50,000	Overshoot	.861	2.182	5x10 ⁶	2.27	652
26° Cone	50,000	Overshoot			1x10 ⁶	2.89	
26° Cone	50,000	Overshoot			2x10 ⁵	4.00	
26° Cone	57,000	Overshoot	1.357	2.702	5x10 ⁶	2.38	682
26° Cone	57,000	Overshoot			1x10 ⁶	3.51	
26° Cone	57,000	Overshoot			2x10 ⁵	4.65	
26° Cone	65,000	Overshoot	9.930	4.948	5x10 ⁶	2.48	720
26° Cone	65,000	Overshoot			1x10 ⁶	4.36	
26° Cone	65,000	Overshoot			2x10 ⁵	5.59	
26° Cone	36,000	Undershoot	.605	1.761	5x10 ⁶	1.22	345
26° Cone	36,000	Undershoot			1x10 ⁶	2.02	
26° Cone	36,000	Undershoot			2x10 ⁵	2.06	
26° Cone	50,000	Undershoot	1.107	2.531	5x10 ⁶	1.65	608
26° Cone	50,000	Undershoot			1x10 ⁶	3.27	
26° Cone	50,000	Undershoot			2x10 ⁵	3.41	
26° Cone	57,000	Undershoot	2.577	3.108	5x10 ⁶	1.95	682
26° Cone	57,000	Undershoot			1x10 ⁶	3.94	
26° Cone	57,000	Undershoot			2x10 ⁵	4.23	

TABLE 3-1 CONT.

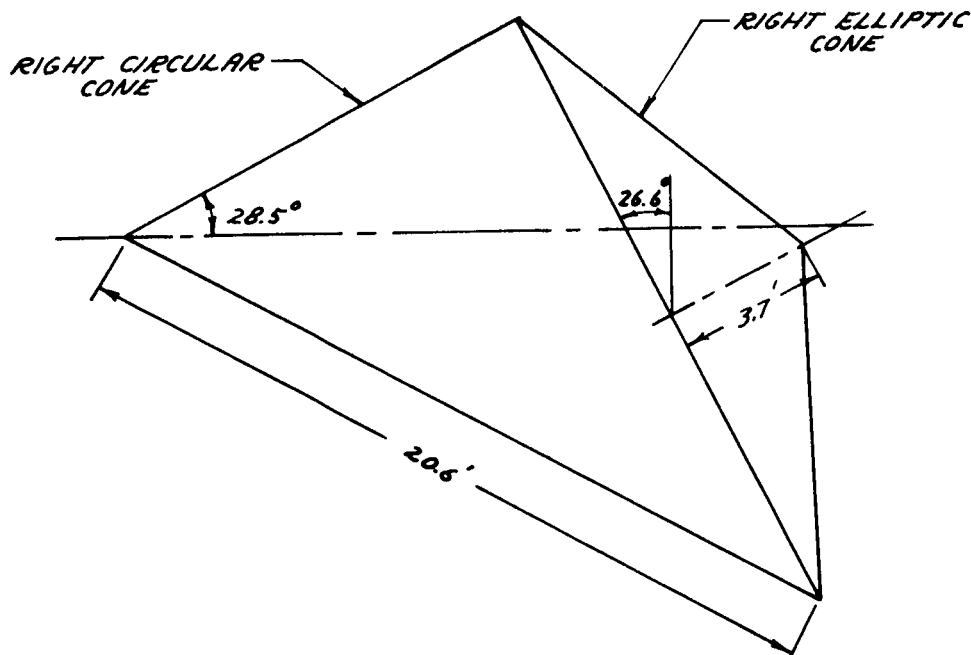
26° Cone	65,000	Undershoot	12.629	6.528	5x10 ⁶	2.30	720
26° Cone	65,000	Undershoot			1x10 ⁶	4.71	
26° Cone	65,000	Undershoot			2x10 ⁵	5.39	
26° Cone	34,784	Re _{surface} = 5x10 ⁶ (Max) at Pull-Out			5x10 ⁶	1.27	
26° Cone	34,784	Re _{surface} = 5x10 ⁶ (Max) at Pull-Out			1x10 ⁵	2.12	
26° Cone	34,784	Re _{surface} = 5x10 ⁶ (Max) at Pull-Out			2x10 ⁵	2.30	
26° Cone	49,515	Re _{surface} = 5x10 ⁶ (Max) at Pull-Out			5x10 ⁶	1.68	
26° Cone	49,515	Re _{surface} = 5x10 ⁶ (Max) at Pull-Out			1x10 ⁶	3.10	
26° Cone	49,515	Re _{surface} = 5x10 ⁶ (Max) at Pull-Out			2x10 ⁵	3.38	

TABLE 3.1 CONT.

FIGURE 3-1 **VEHICLE CHARACTERISTICS**

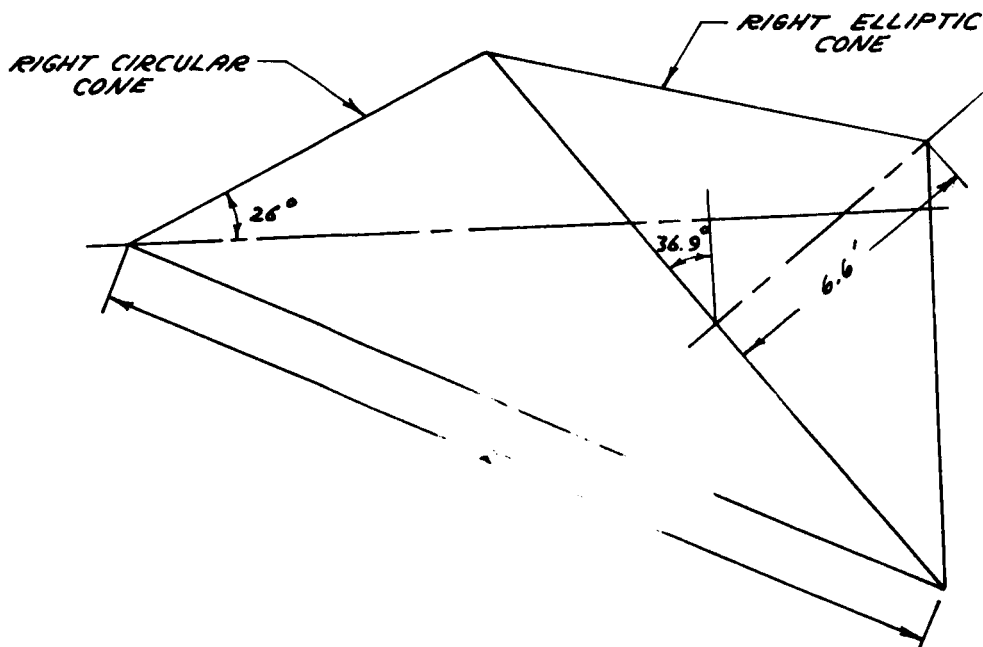
VOLUME = 1,000 FT³
WEIGHT = 10,000 LB

28.5° CONE



$L/D = 0.5$
 $W/C_D A = 122 \text{ LB/FT}^2$
FOREBODY AREA = 378 FT²
AFTERBODY AREA = 215 FT²

26° CONE



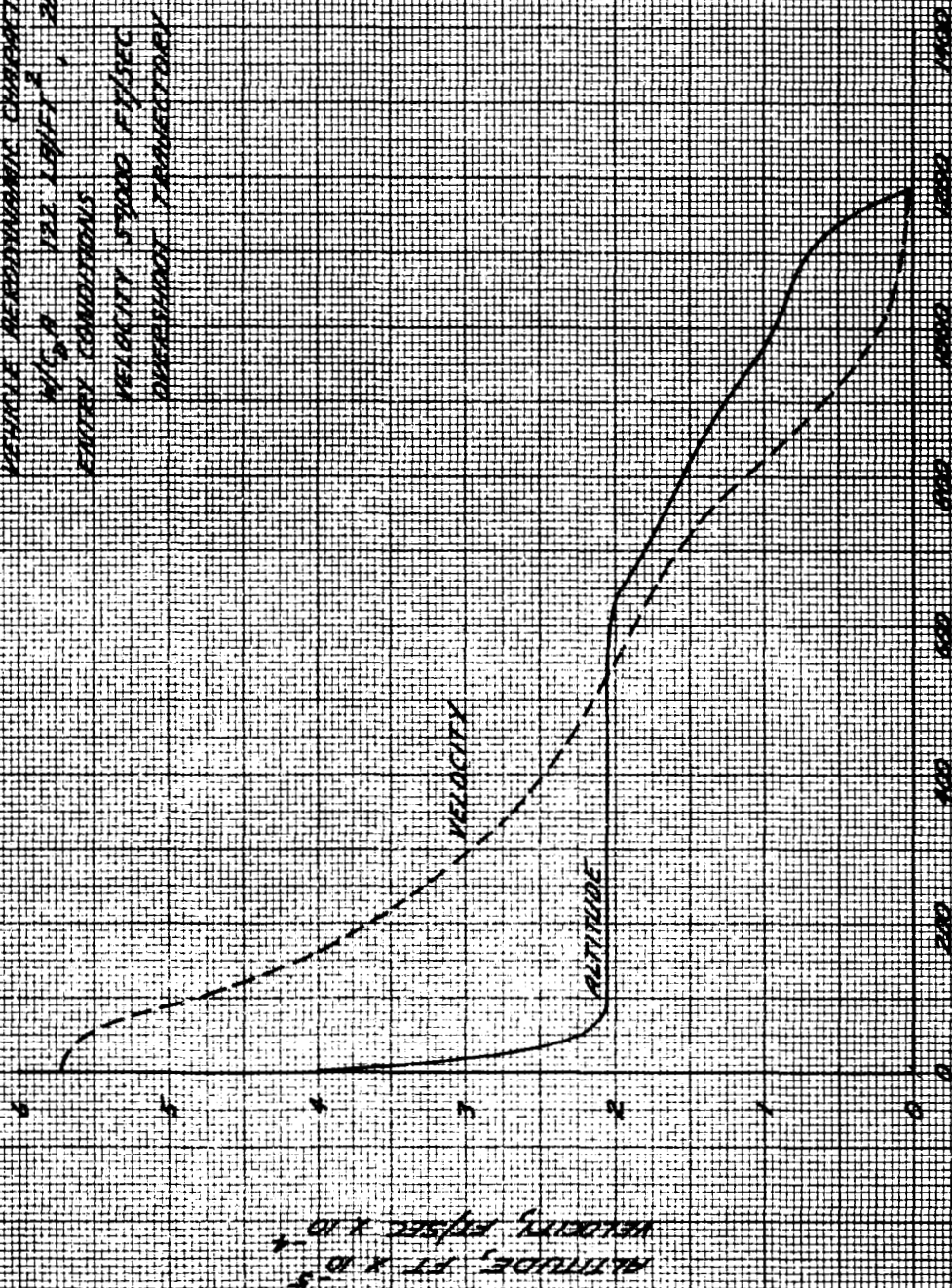
$L/D = 0.75$
 $W/C_D A = 172 \text{ LB/FT}^2$
FOREBODY AREA = 348 FT²
AFTERBODY AREA = 240 FT²

FIGURE 3-2

TYPICAL ENTRY TRAJECTORY

VEHICLE AERODYNAMIC CHARACTERISTICS
 $M_0 = 4$ 122 LIFT 2 , 28.5° CONE
 ENTRY CONDITIONS

VELOCITY 57000 FT/SEC
 OVERBURST TRAJECTORY



TIME FROM BURNOUT, SEC

FIGURE 3-3

PULL-OUT CHARACTERISTICS

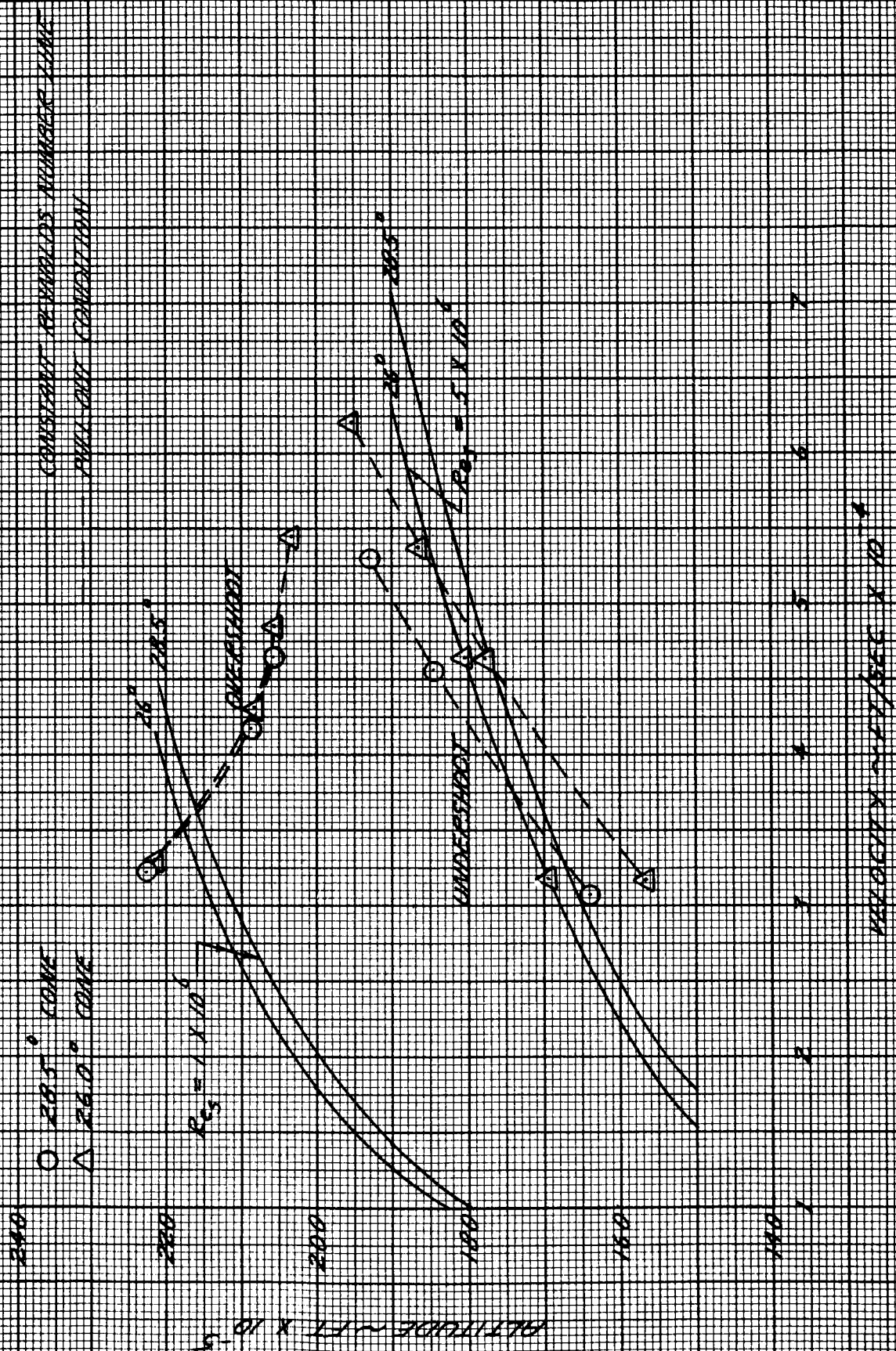


FIGURE 3-4

COLD WALL CONVECTIVE HEAT FLUX HISTORY

28.5° CONE
 $S = 5$ FT
 $R_{\text{NO}} = 5 \times 10^6$
 $V_{\text{E}} = 57000$ FT/SEC
 OVERSHOOT TRAJECTORY

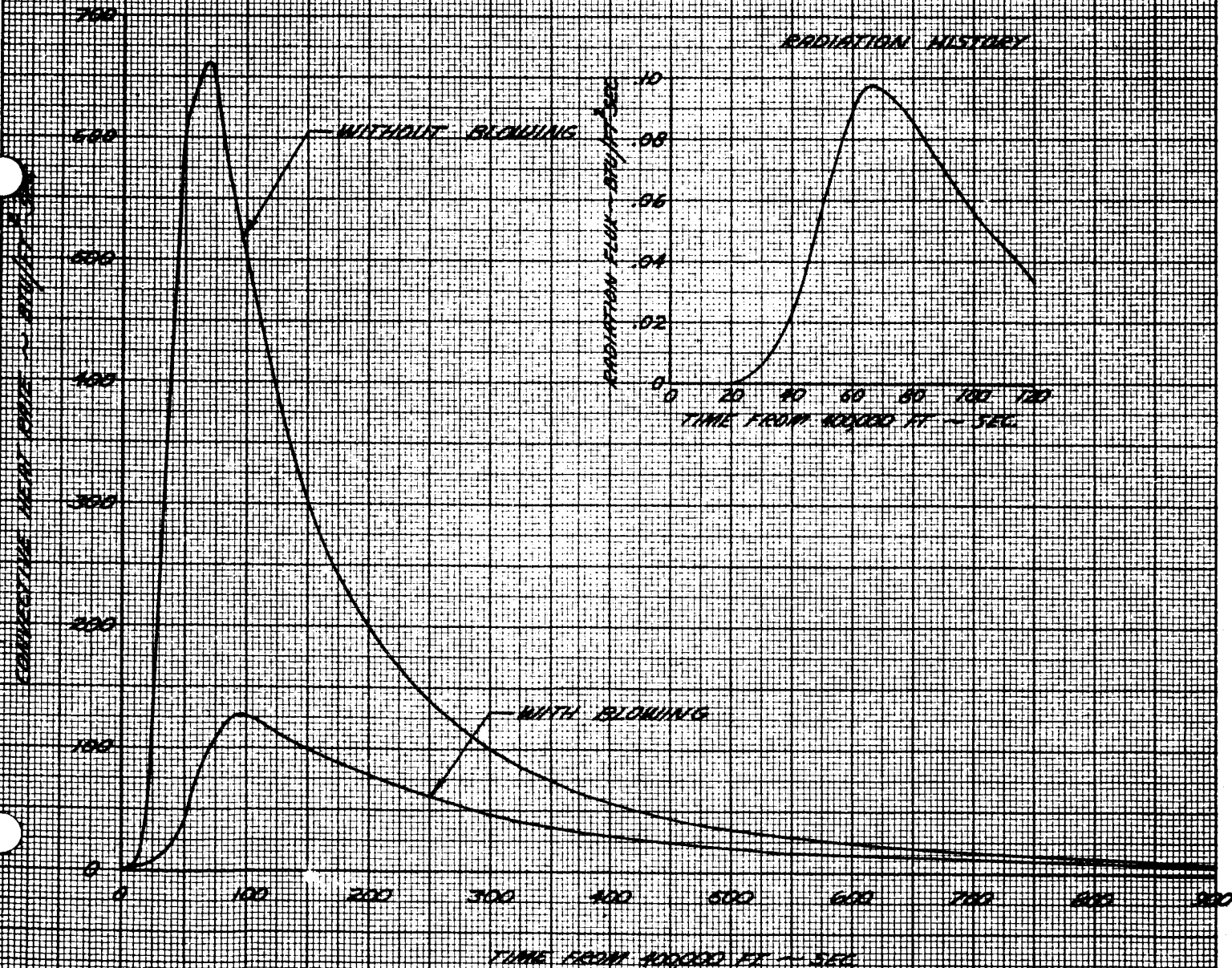
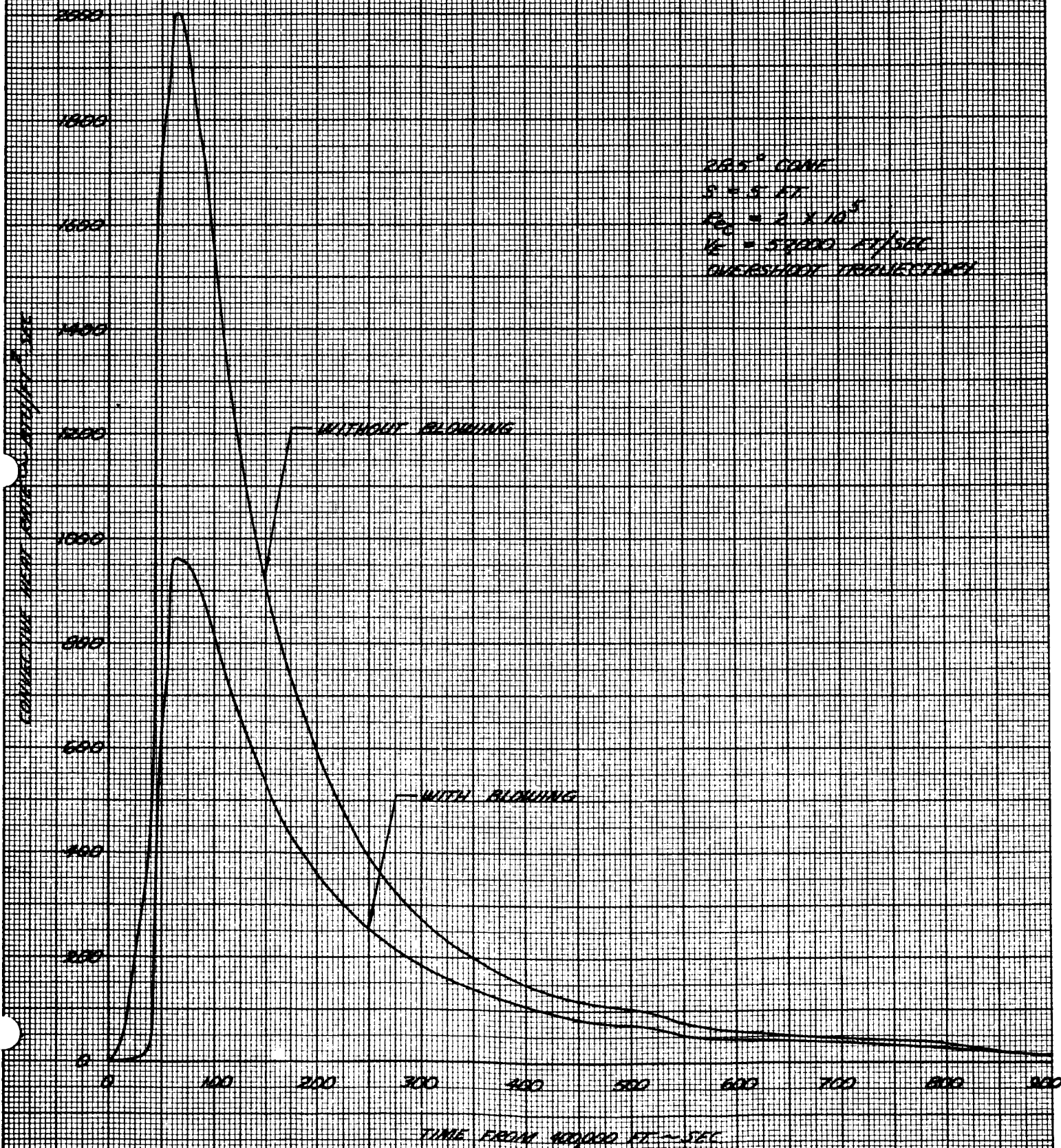


FIGURE 3-5

COLD WALL CONVECTIVE HEAT FLUX HISTORY



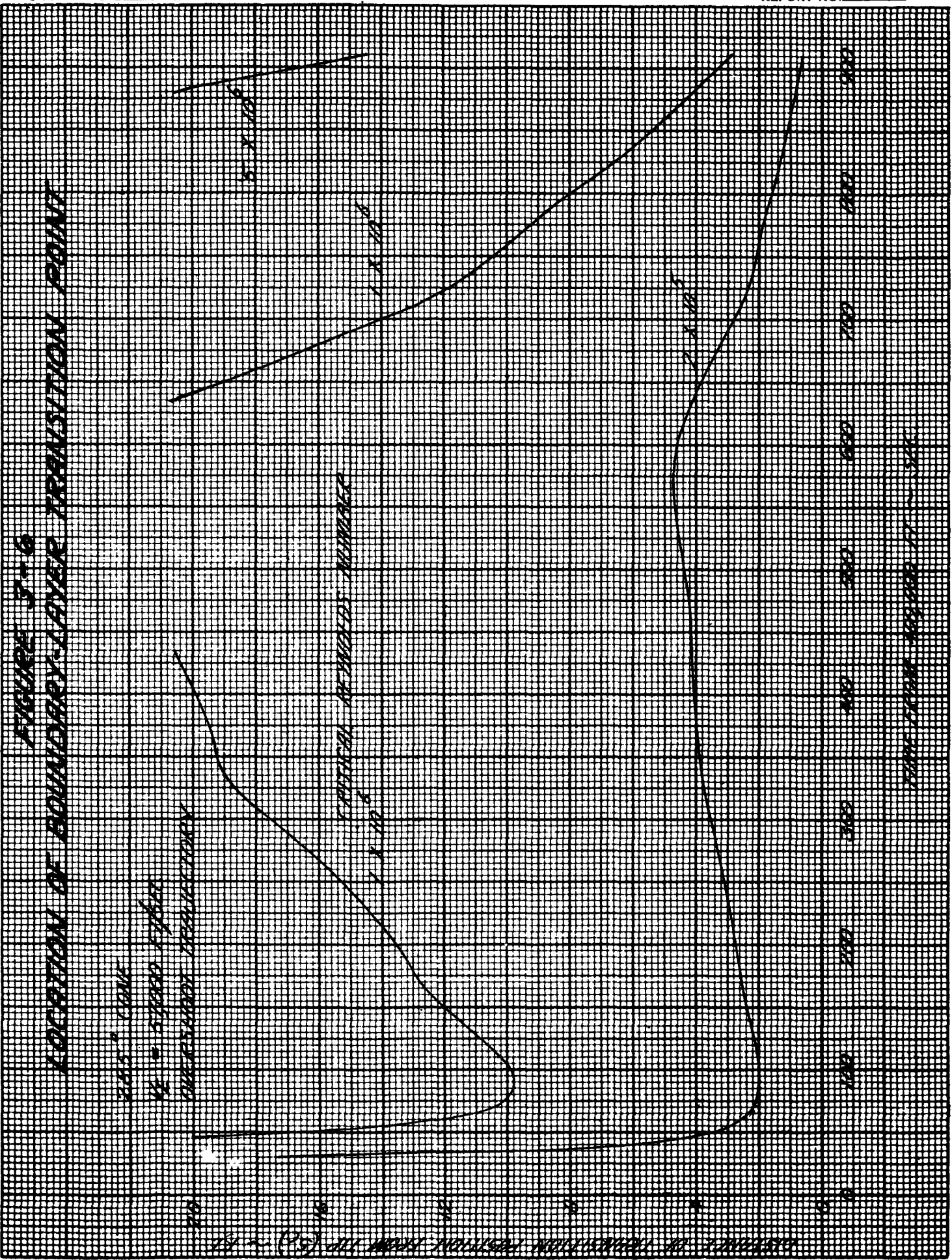


FIGURE 3-7

INFLUENCE OF CONE ANGLE ON RADIATION AT TIME OF PULLOUT

PAC 3.11
 $V_c = 65000 \text{ FT/SEC}$
 UNDERSHOOT TRAJECTORY

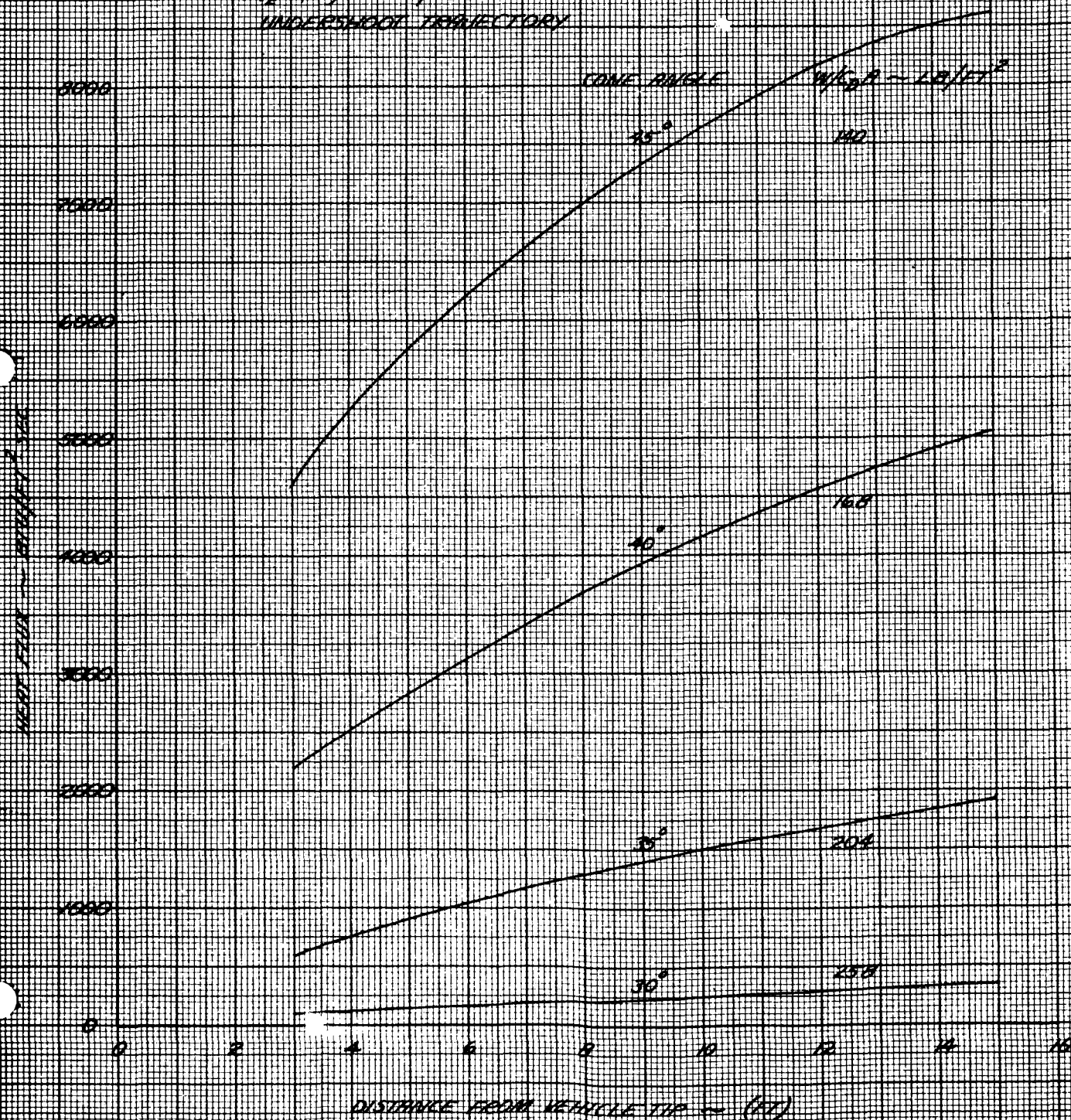


FIGURE 3-B MATERIAL DEGRADATION HISTORY

26.5° CONE
 $S = 5 \text{ FT}$
 $R_{\text{eff}} = 2 \times 10^5$
 $V_0 = 50000 \text{ FT/SEC}$
 OVERSHOOT TRAJECTORY

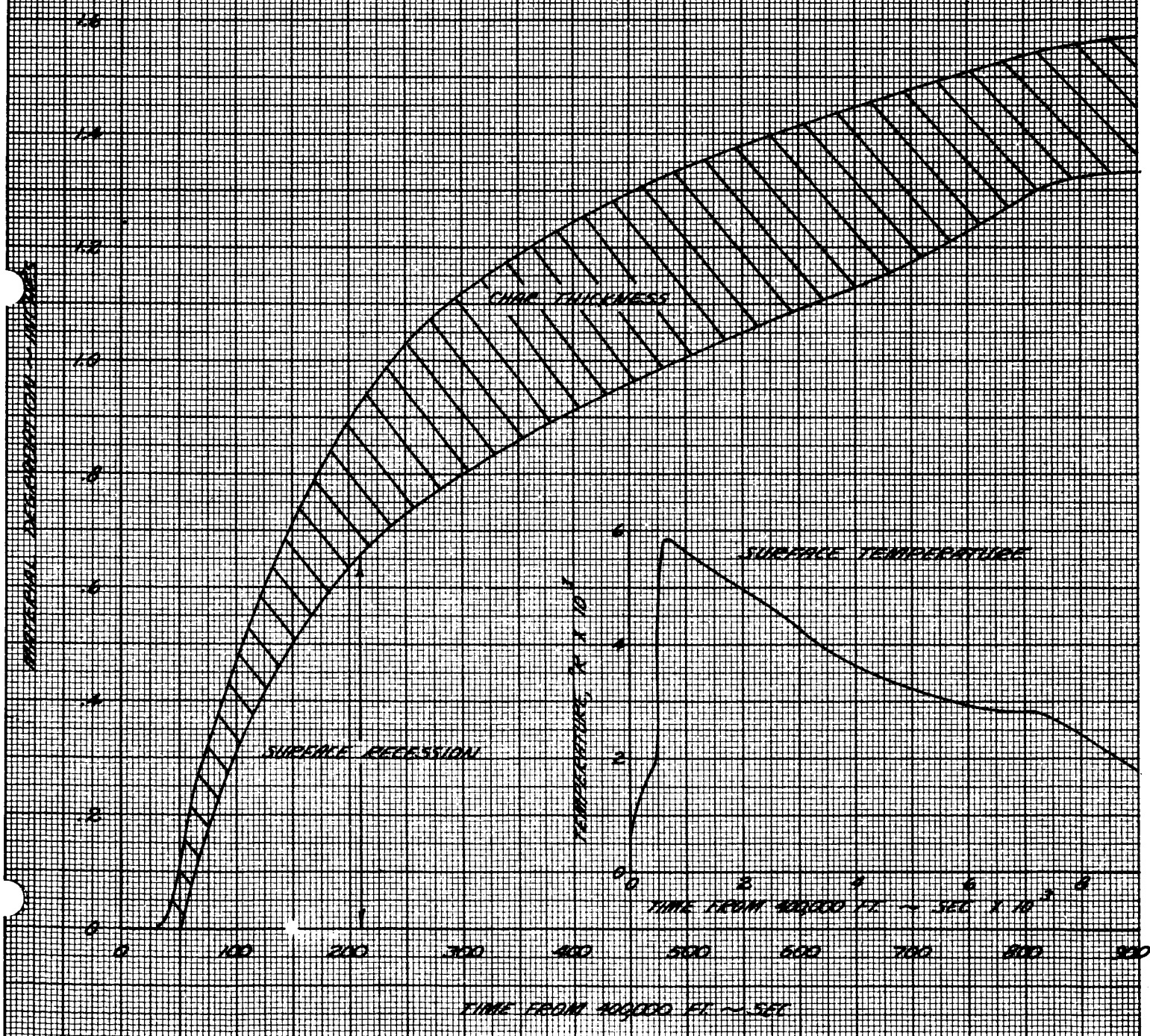
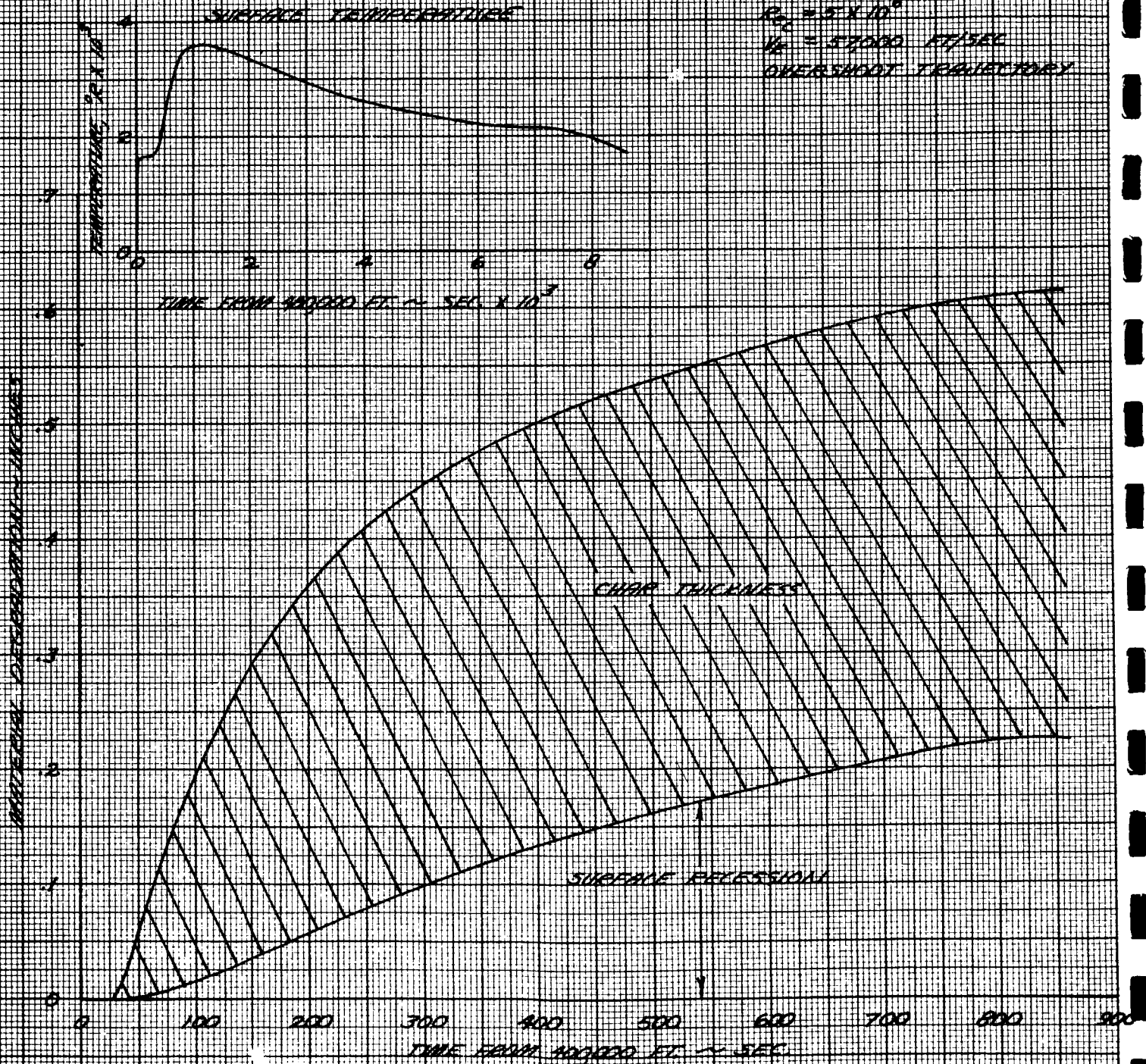


FIGURE 3-9

MATERIAL DEGRADATION HISTORY

DR.5° CONE
 $S = 5 \text{ FT.}$
 $R_0 = 5 \times 10^6$
 $V = 57,000 \text{ FT/SEC}$
 OVERSHOT TRAJECTORY



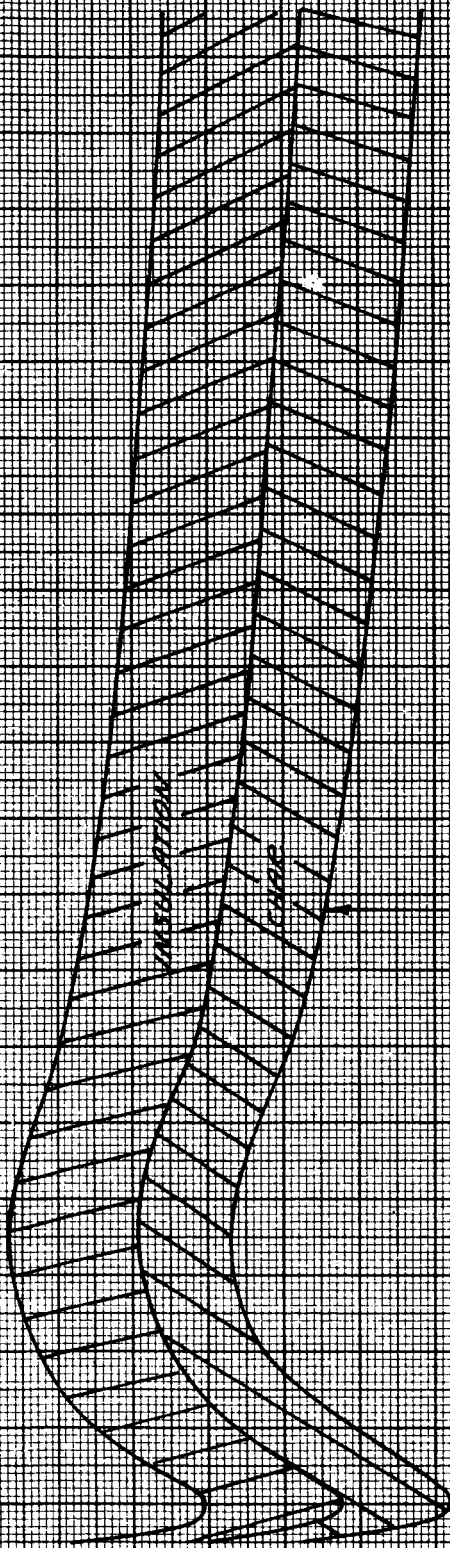
PREPARED BY
 DATE
 CHECKED BY

LOCKHEED MISSILES & SPACE COMPANY
 A GROUP DIVISION OF LOCKHEED AIRCRAFT CORPORATION

PAGE
 MODEL
 REPORT NO.

HEAT SHIELD THICKNESS DISTRIBUTION

20.5° cone
 $R_{\text{H}} = 2 \times 10^5$
 $W = 37000 \text{ lb/sec}$
 OVERSHOOT NOT INDICATED



SURFACE DISTANCE

THICKNESS - INCHES

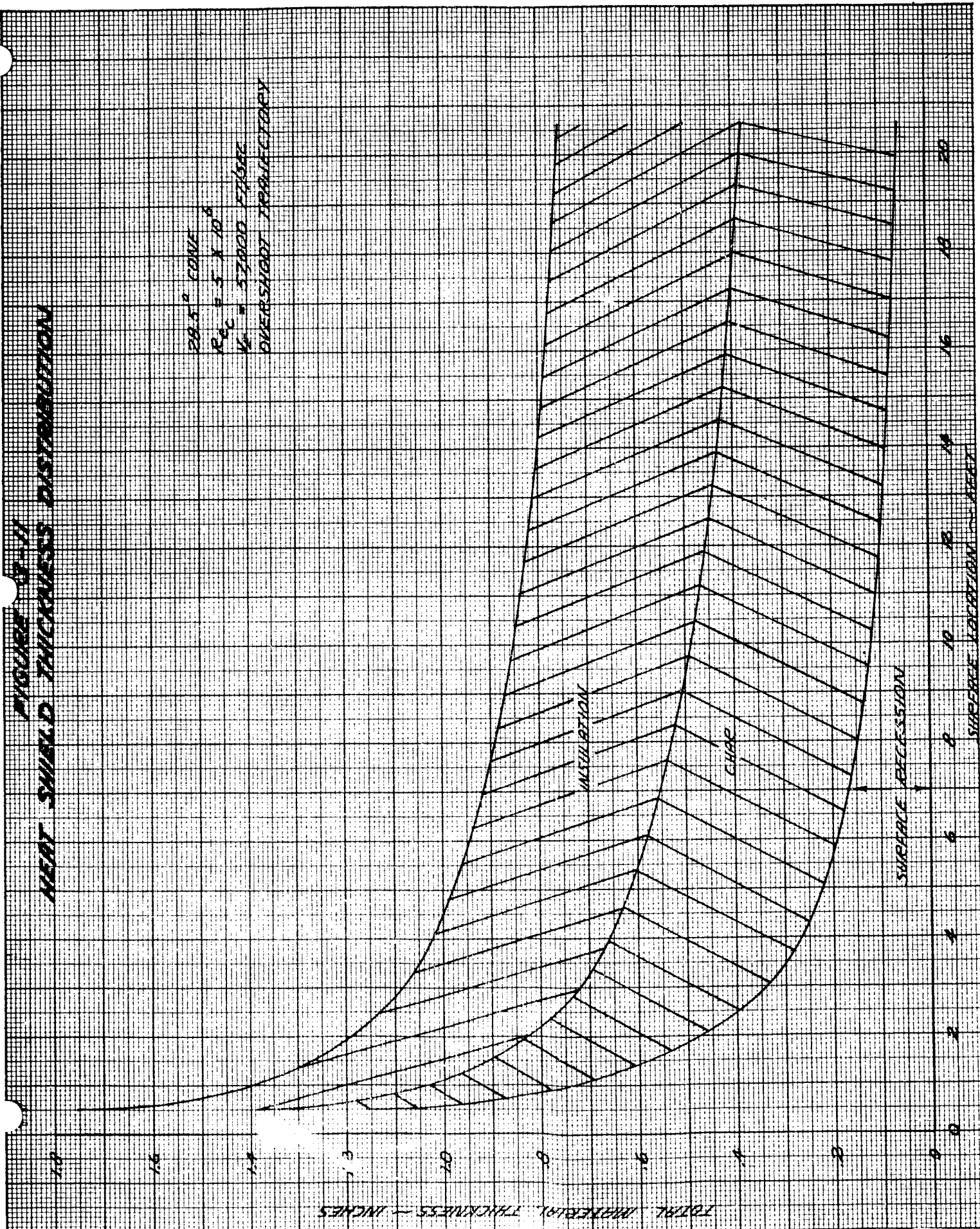
FIGURE 3-11
 HEAT SHIELD THICKNESS DISTRIBUTION

20.5" CONE
 $R_{AC} = 5.5 \times 10^{-6}$
 $V = 52000 \text{ FT/SEC}$
 OVERSHOOT TRAJECTORY

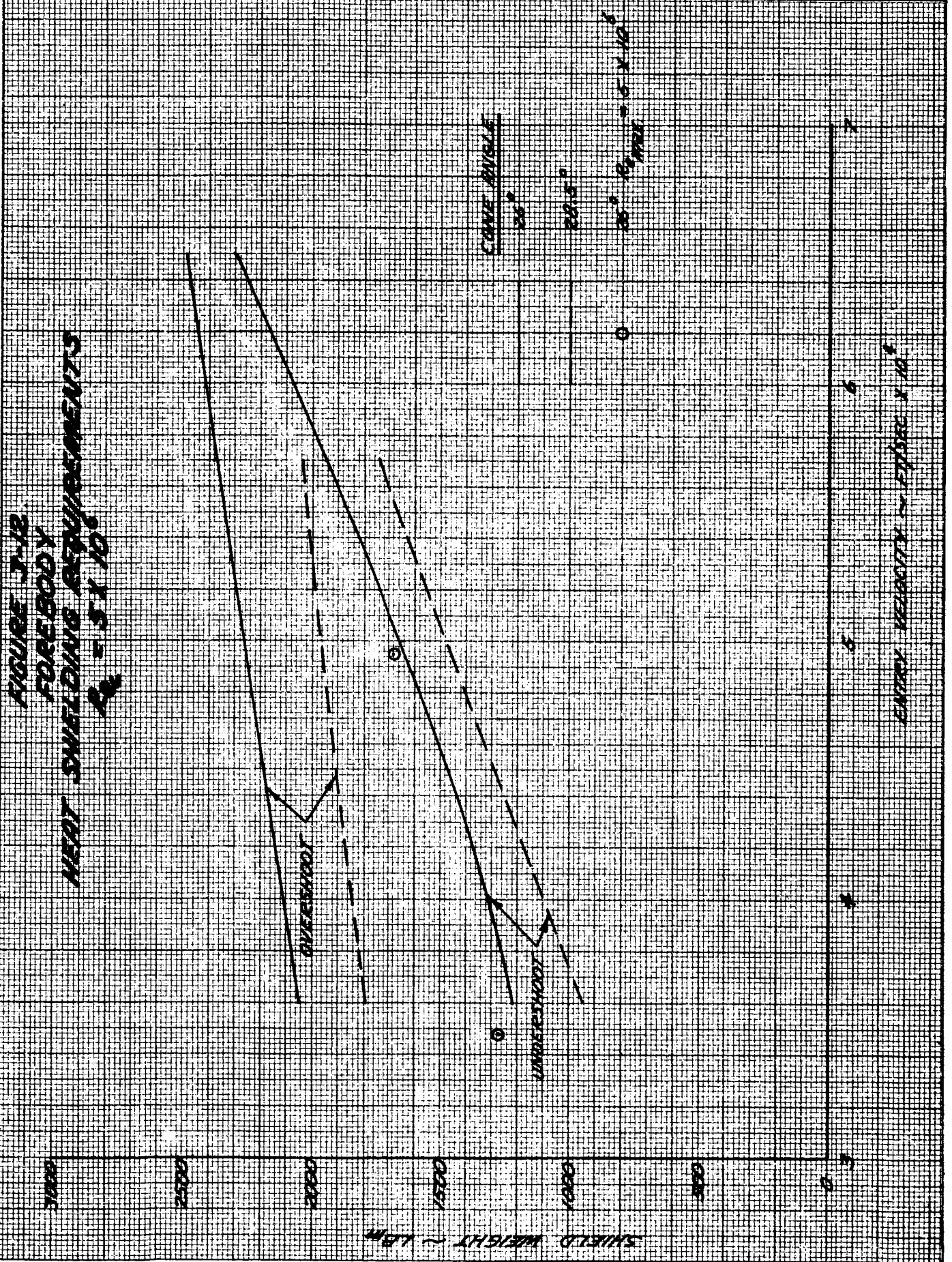
TOTAL MATERIAL THICKNESS - INCHES

SURFACE REGRESSION

SURFACE LOCATION - FEET

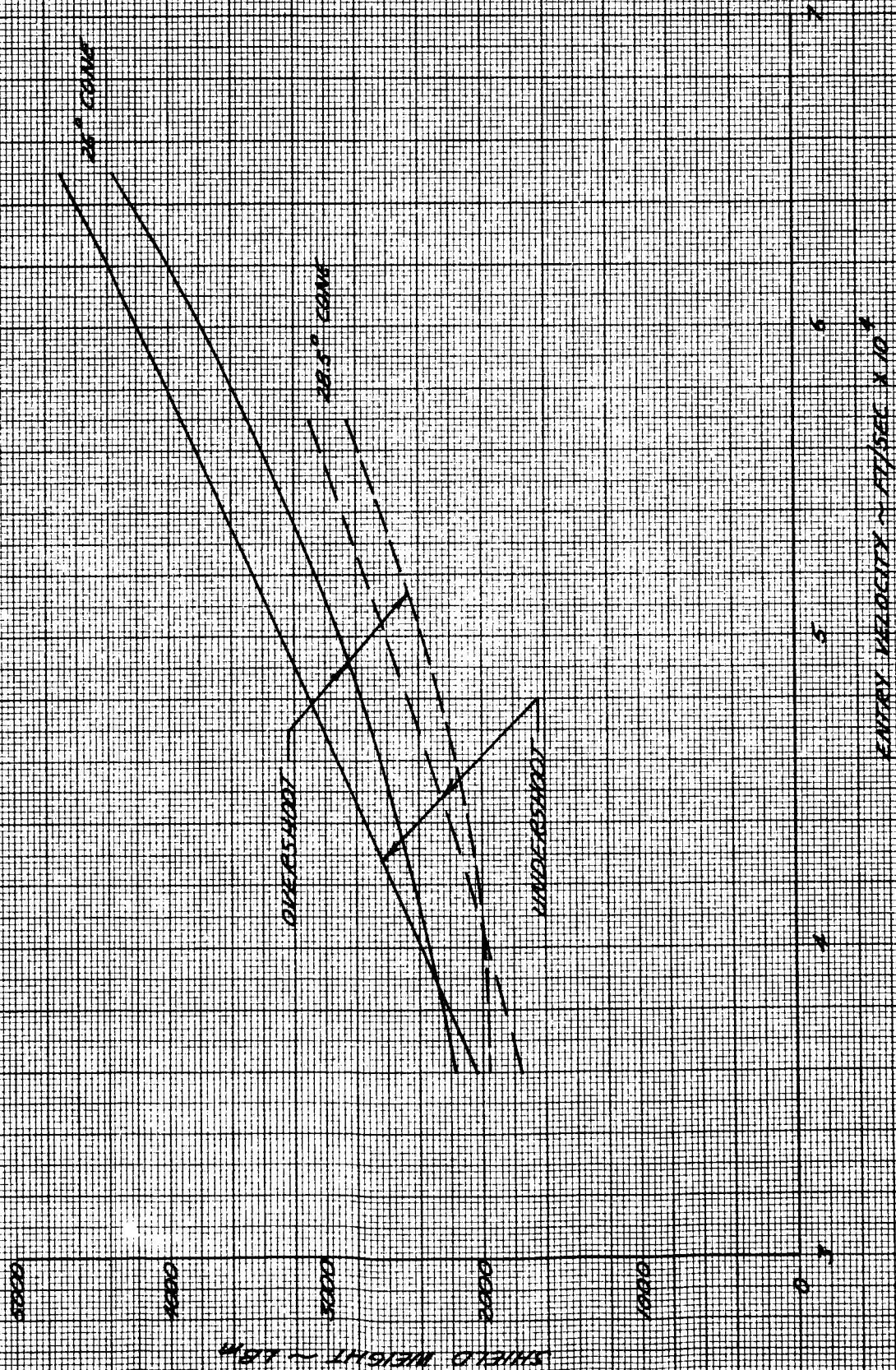


Prepared	NAME <i>sil</i>	DATE	LOCKHEED MISSILES & SPACE COMPANY A GROUP DIVISION OF LOCKHEED AIRCRAFT CORPORATION	Page	TEMP.	PERM.
Checked			TITLE			
Approved				Model		
				Report No.		



Prepared	NAME <i>sf</i>	DATE	LOCKHEED MISSILES & SPACE COMPANY A GROUP DIVISION OF LOCKHEED AIRCRAFT CORPORATION	Page	TEMP.	PERM.
Checked			TITLE		Model	
Approved					Report No.	

FIGURE 3-13
FOREBODY
HEAT SHIELDING REQUIREMENTS
 $Re = 1 \times 10^6$



Prepared	NAME <i>gil</i>	DATE	LOCKHEED MISSILES & SPACE COMPANY A GROUP DIVISION OF LOCKHEED AIRCRAFT CORPORATION	Page	TEMP.	PERM.
Checked			TITLE		Model	
Approved					Report No.	

FIGURE 3-14
FORN BODY
HEAT SHIELDING REQUIREMENTS
 $R_n = 2 \times 10^5$



Prepared	NAME <i>gil</i>	DATE	LOCKHEED MISSILES & SPACE COMPANY A GROUP DIVISION OF LOCKHEED AIRCRAFT CORPORATION	Page	TEMP.	PERM.
Checked			TITLE		Model	
Approved					Report No.	

FIGURE 3-15
INFLUENCE OF TRANSITION UNCERTAINTY ON FOREBODY
HEAT SHIELDING REQUIREMENTS

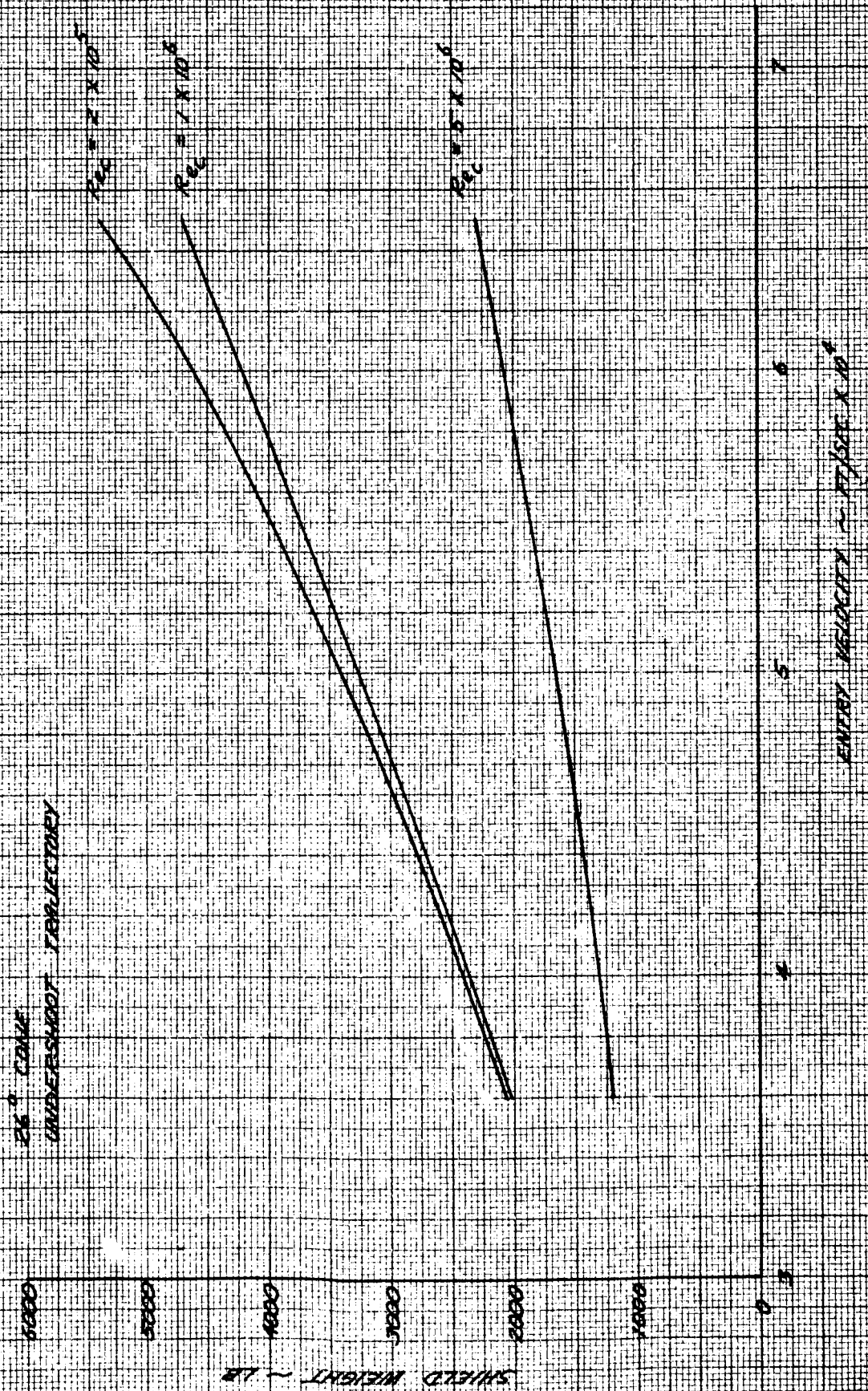


FIGURE 3-16

INFLUENCE OF CRITICAL REYNOLDS NUMBER ON FOREBODY HEAT SHIELDING REQUIREMENTS

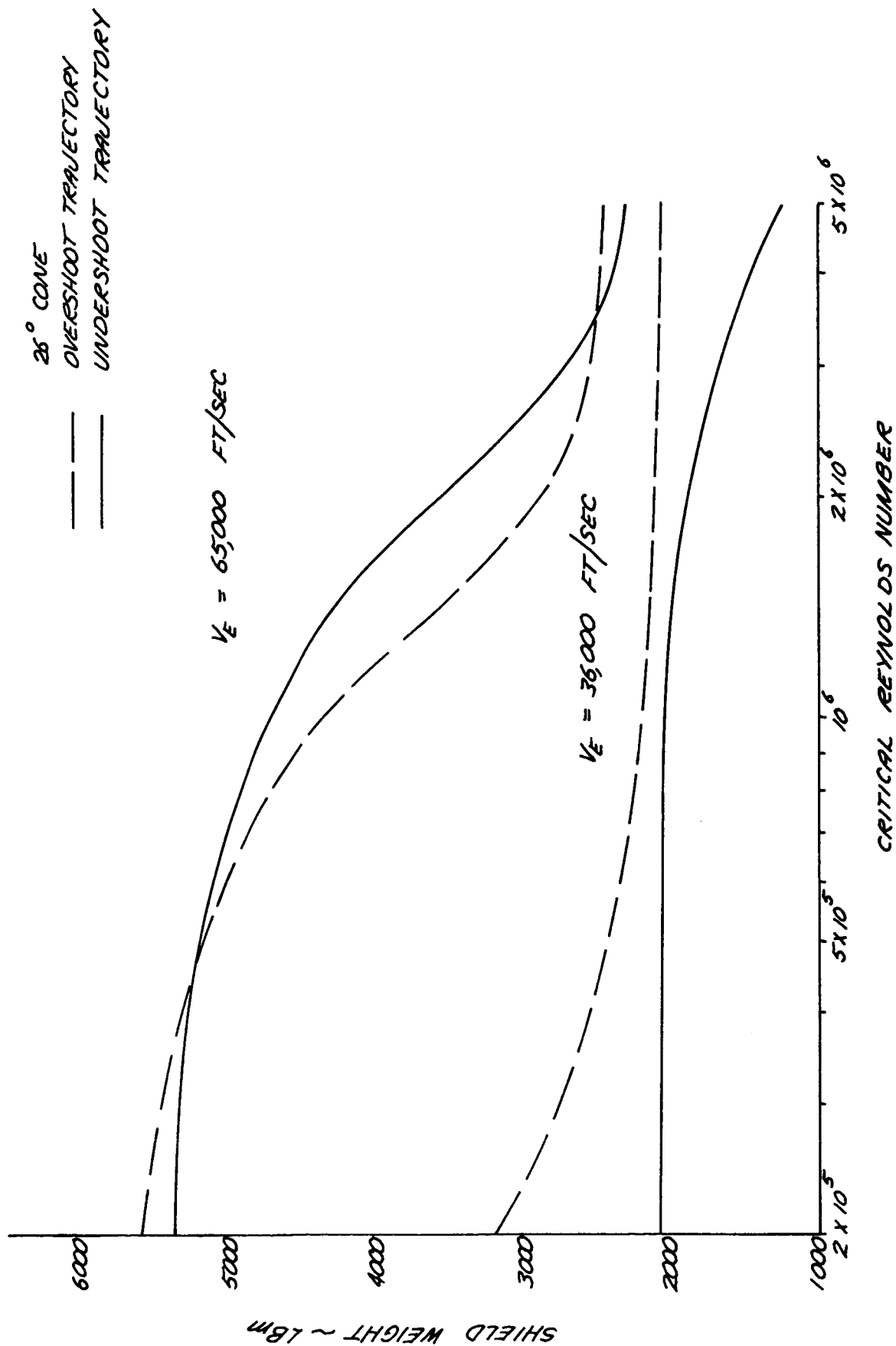


FIGURE 3-17
 COMPARISON OF SHIELDING REQUIREMENTS FOR SEVERAL
 ENTRY VEHICLE CONFIGURATIONS

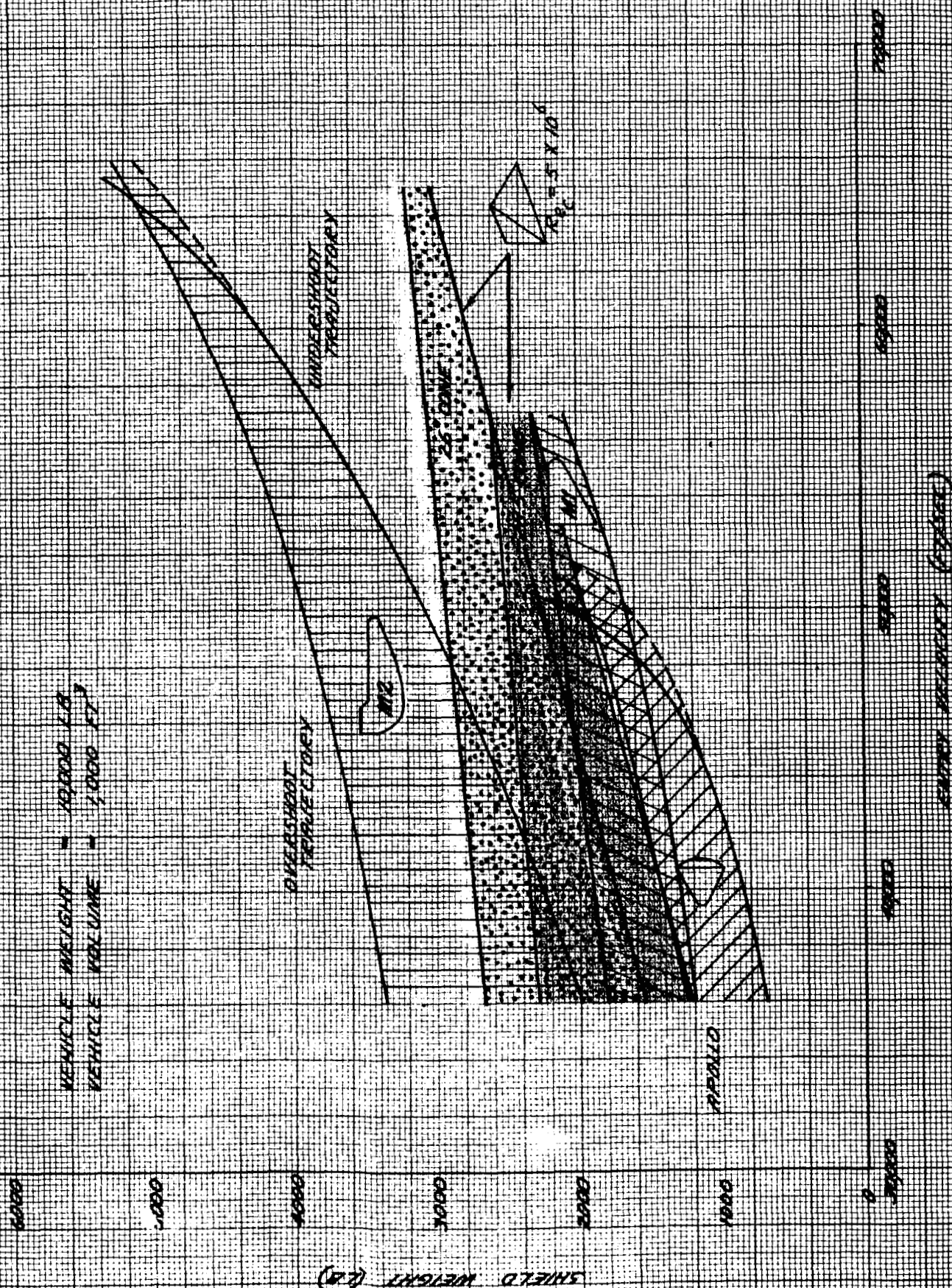


FIGURE 3-18

STAGNATION POINT HEATING HISTORY

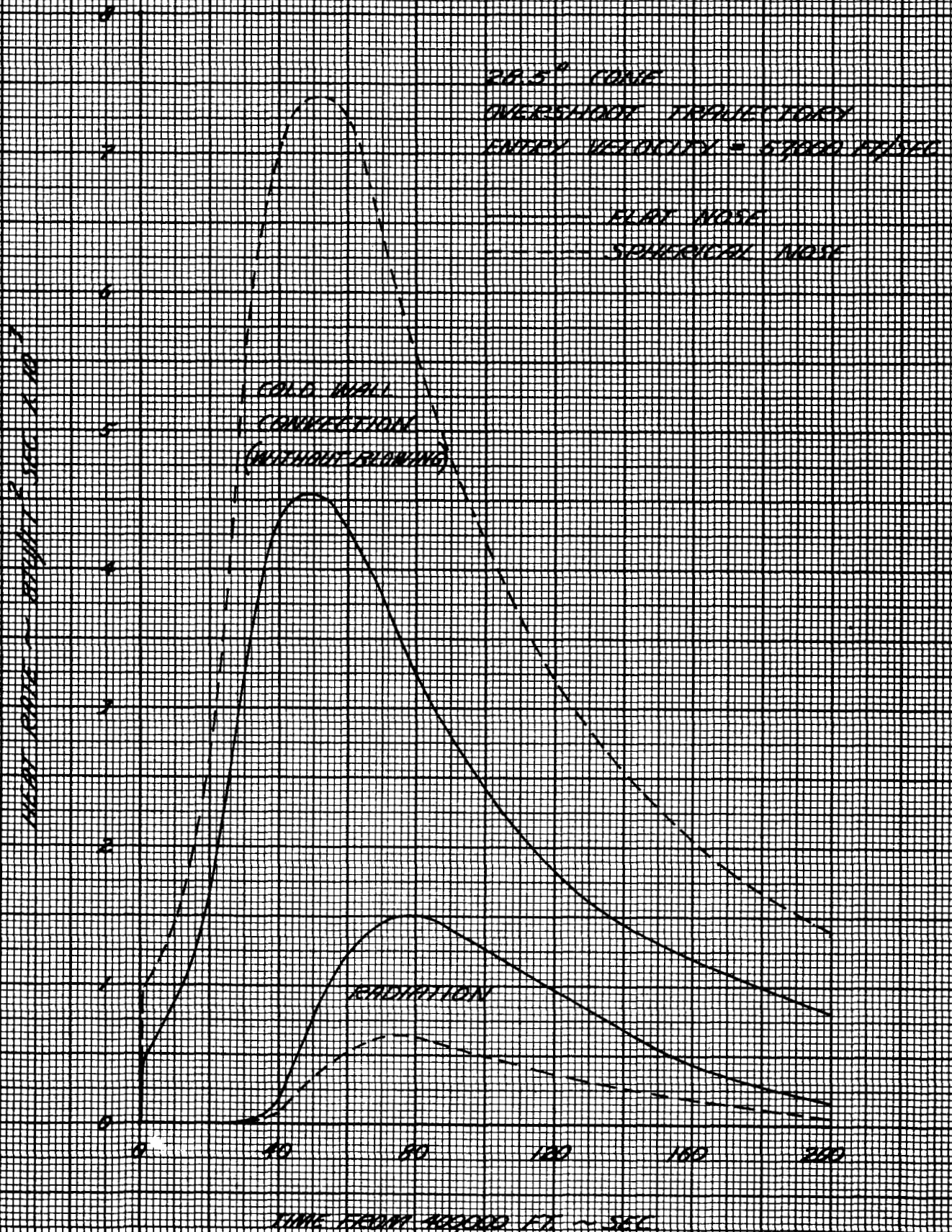
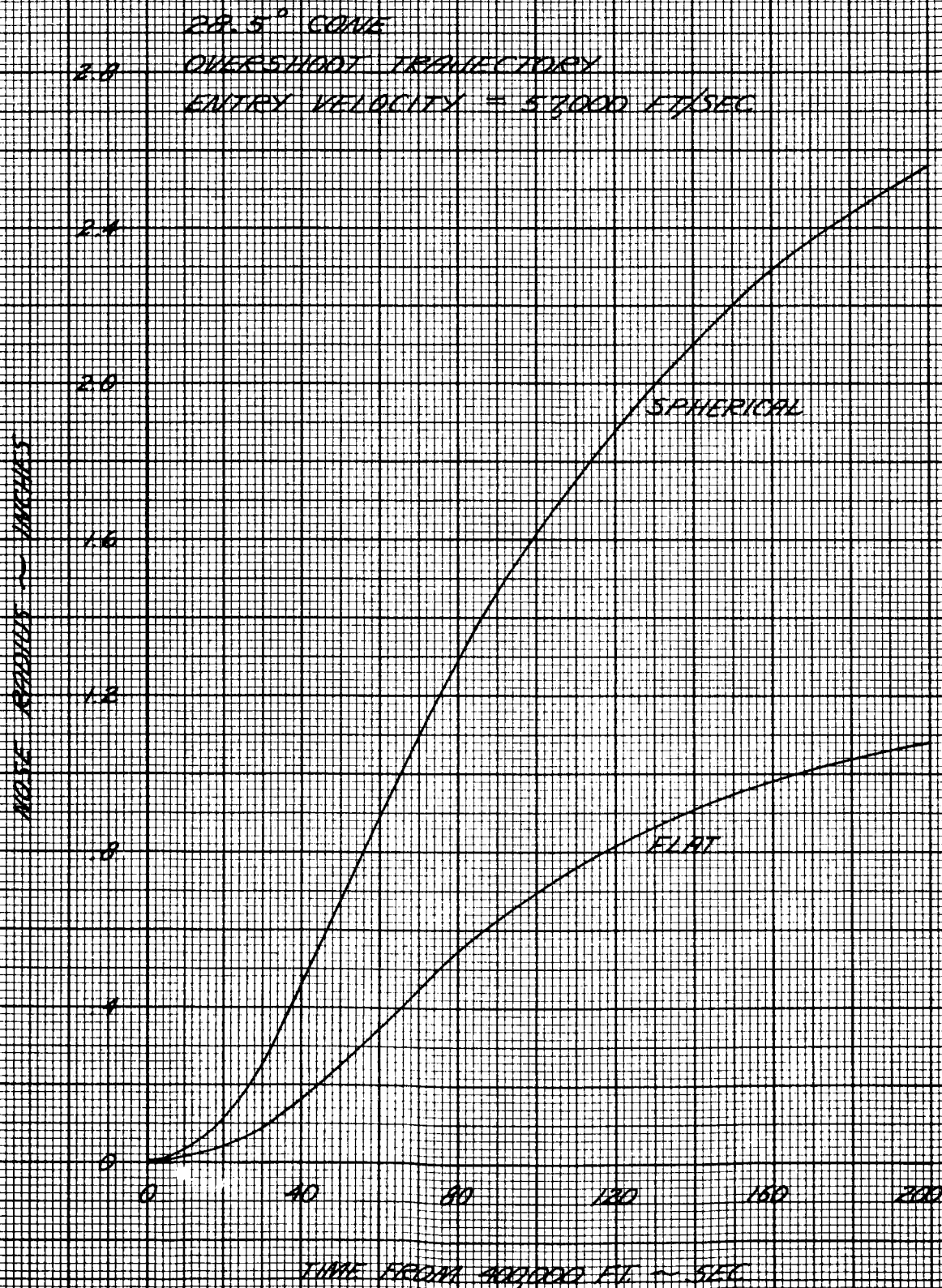


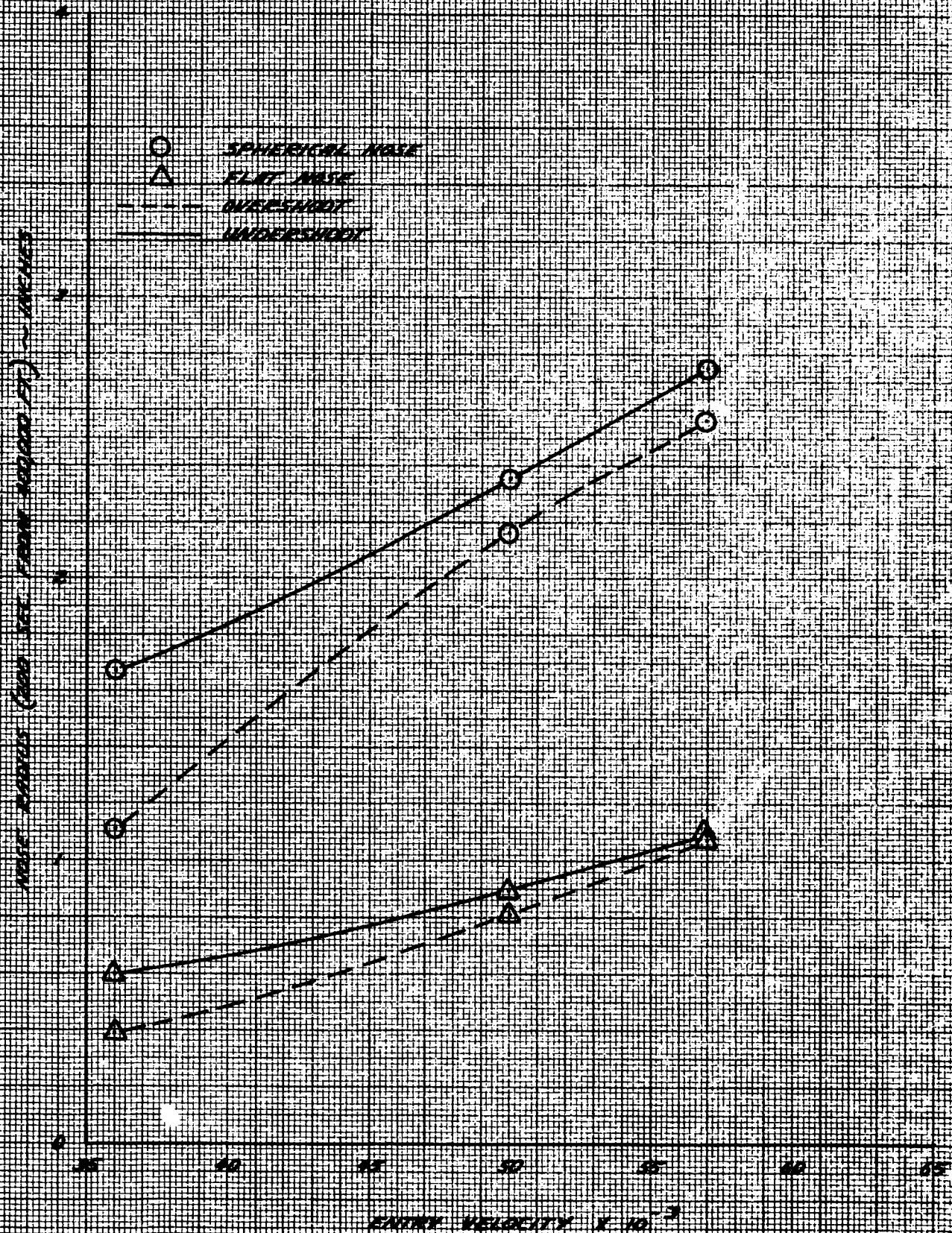
FIGURE 3-19

NOSE RADIUS HISTORY



Prepared	NAME <i>cj</i>	DATE 5-14-65	LOCKHEED MISSILES & SPACE COMPANY A GROUP DIVISION OF LOCKHEED AIRCRAFT CORPORATION	Page	TEMP.	PERM.
Checked			TITLE	Model		
Approved				Report No.		

FIGURE 3-20
INFLUENCE OF ENTRY VELOCITY ON THE NOSE
BLUNTNESS OF A 22.5° CONE



Prepared	NAME <i>ajj</i>	DATE 5-14-65	LOCKHEED MISSILES & SPACE COMPANY A GROUP DIVISION OF LOCKHEED AIRCRAFT CORPORATION	Page	TEMP.	PERM.
Checked			TITLE	Model		
Approved				Report No.		

FIGURE 3-21
INFLUENCE OF ENTRY VELOCITY ON THE NOSE
BLUNTNESS OF A 26° CONE

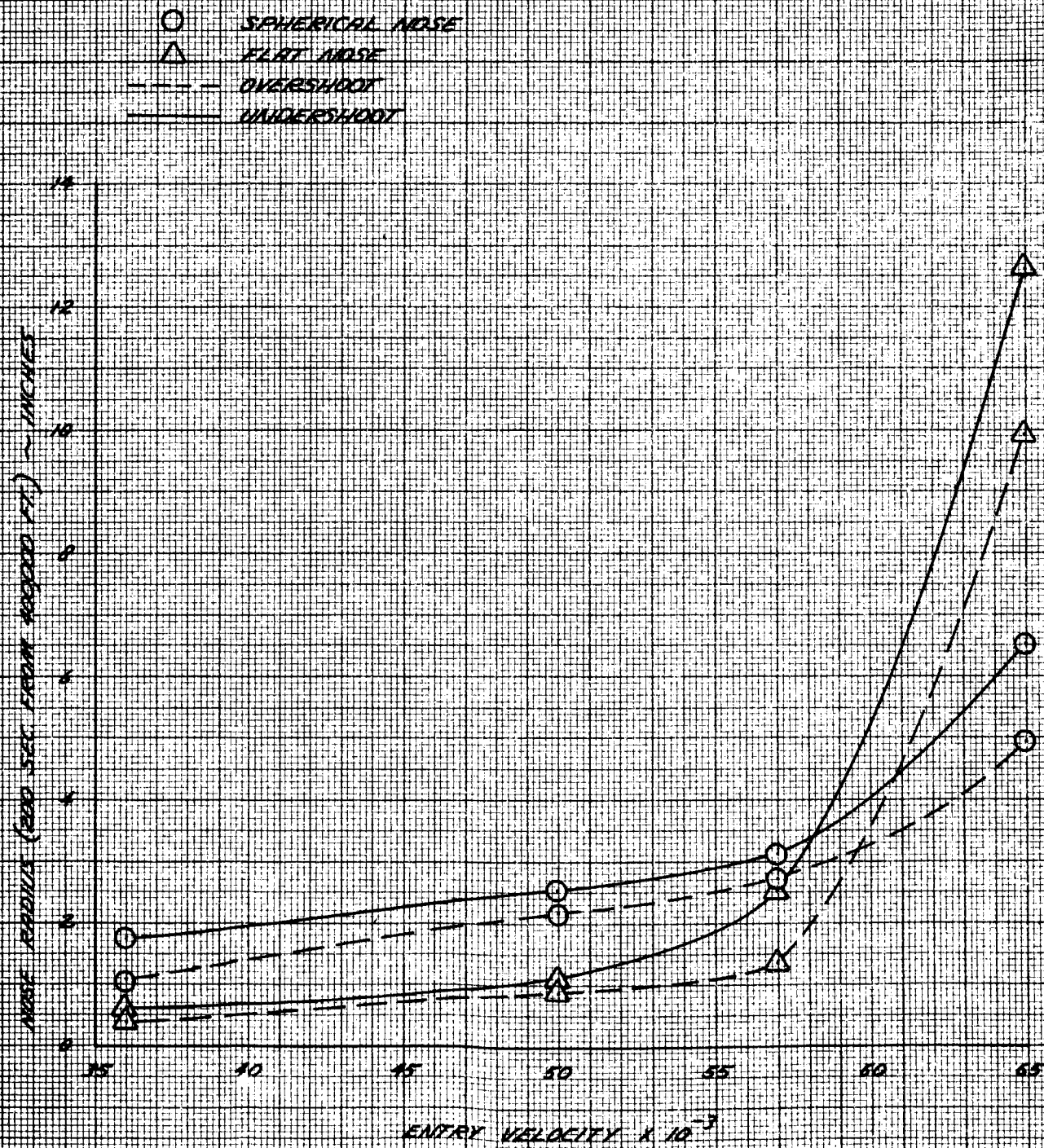
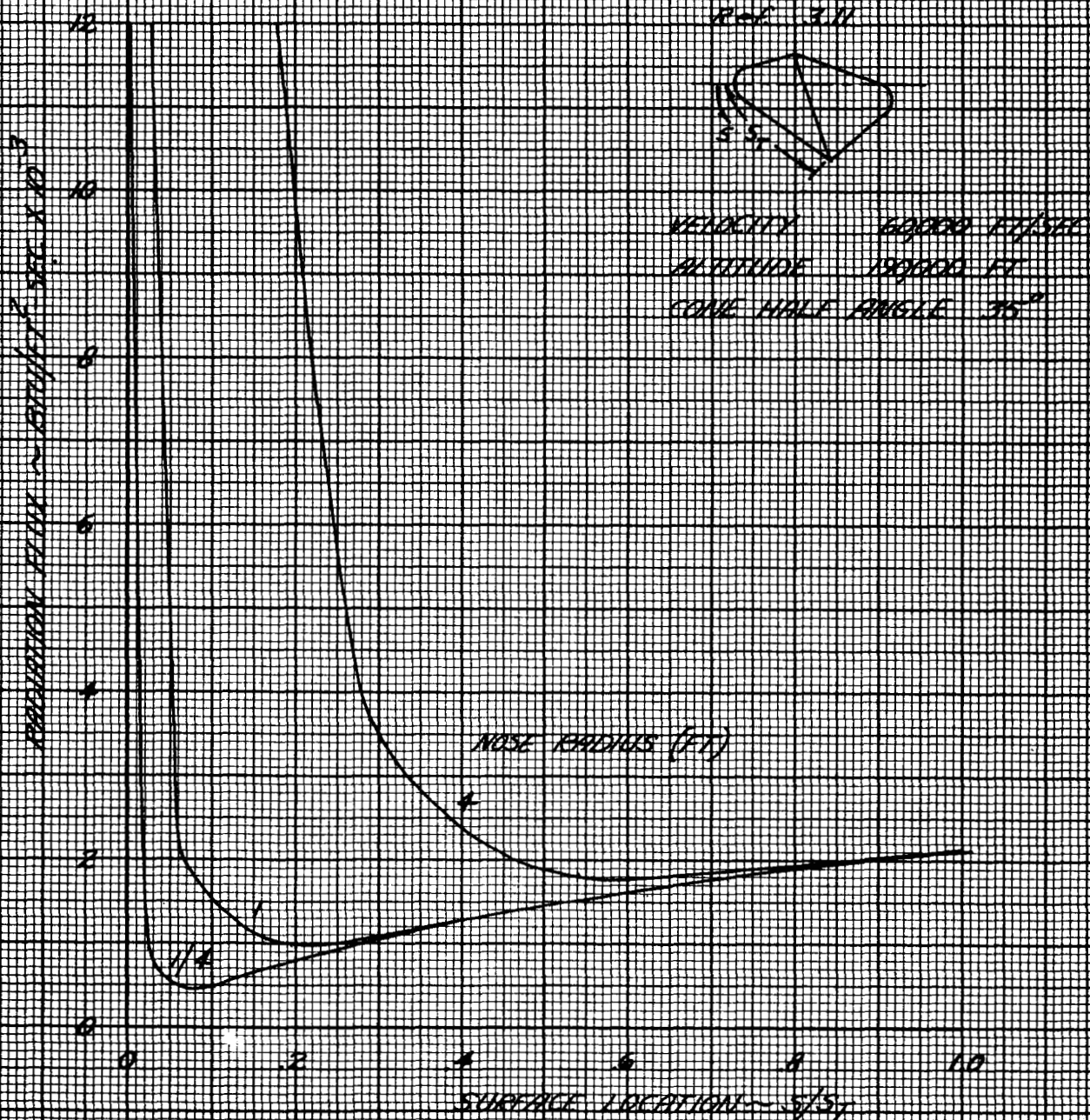


FIGURE 3-22

INFLUENCE OF NOSE RADIUS ON RADIATION
 TO A CONICAL SURFACE



Prepared	NAME <i>cjl</i>	DATE	LOCKHEED MISSILES & SPACE COMPANY A GROUP DIVISION OF LOCKHEED AIRCRAFT CORPORATION	Page	TEMP. 4-124
Checked			TITLE	Model	
Approved				Report No.	

FIGURE 3-23
LAMINAR HEAT TRANSFER DISTRIBUTION FACTOR
24.3° CONE ANGLE

$$\text{LAMINAR VORTICITY PARAMETER, } N_{VL} = \left(\frac{1}{P_{\infty} u_{\infty}} \right) \left(\frac{P_{\infty} q_{\infty} A_{\infty}}{k_{\infty}} \right)^{0.5}$$

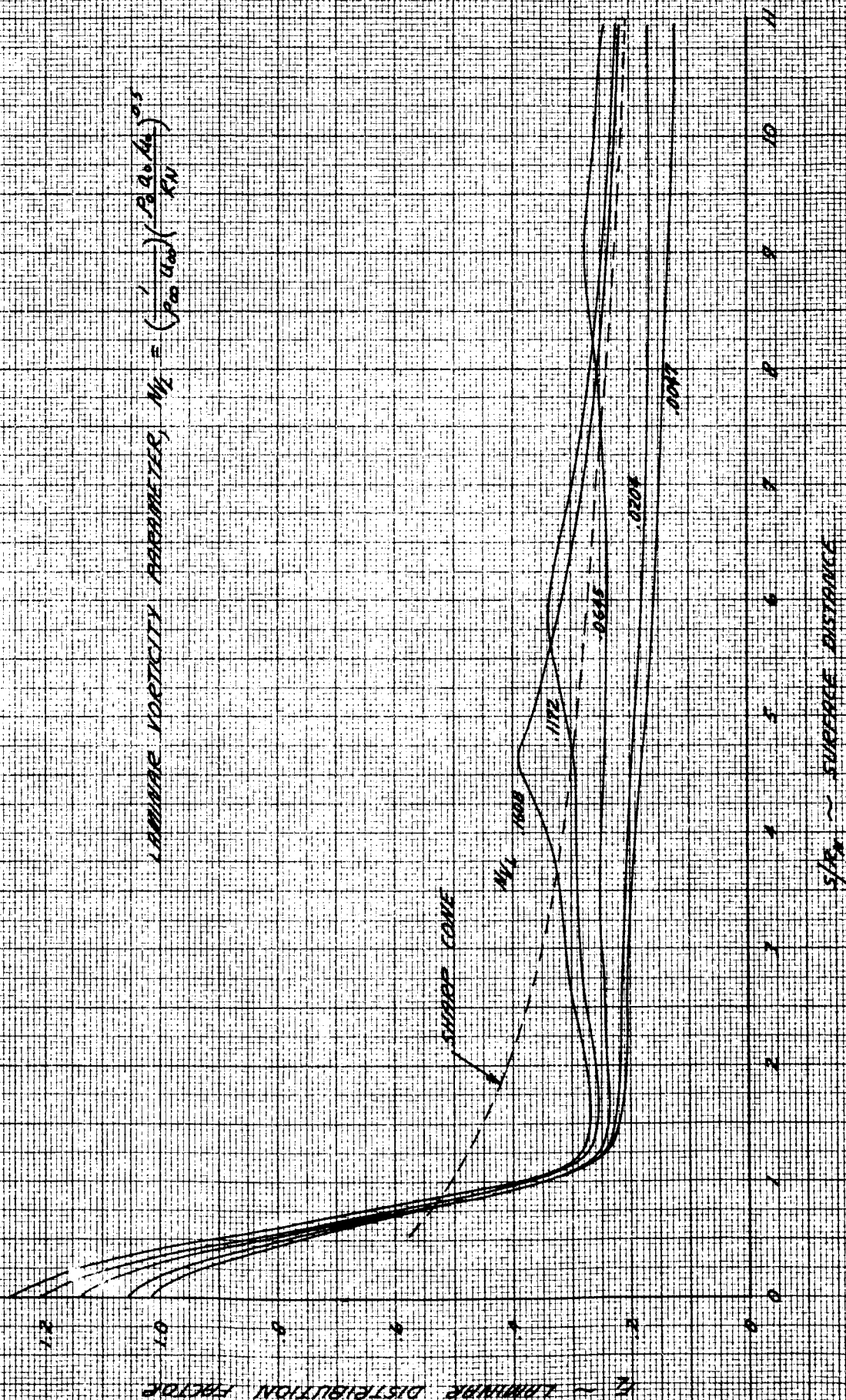
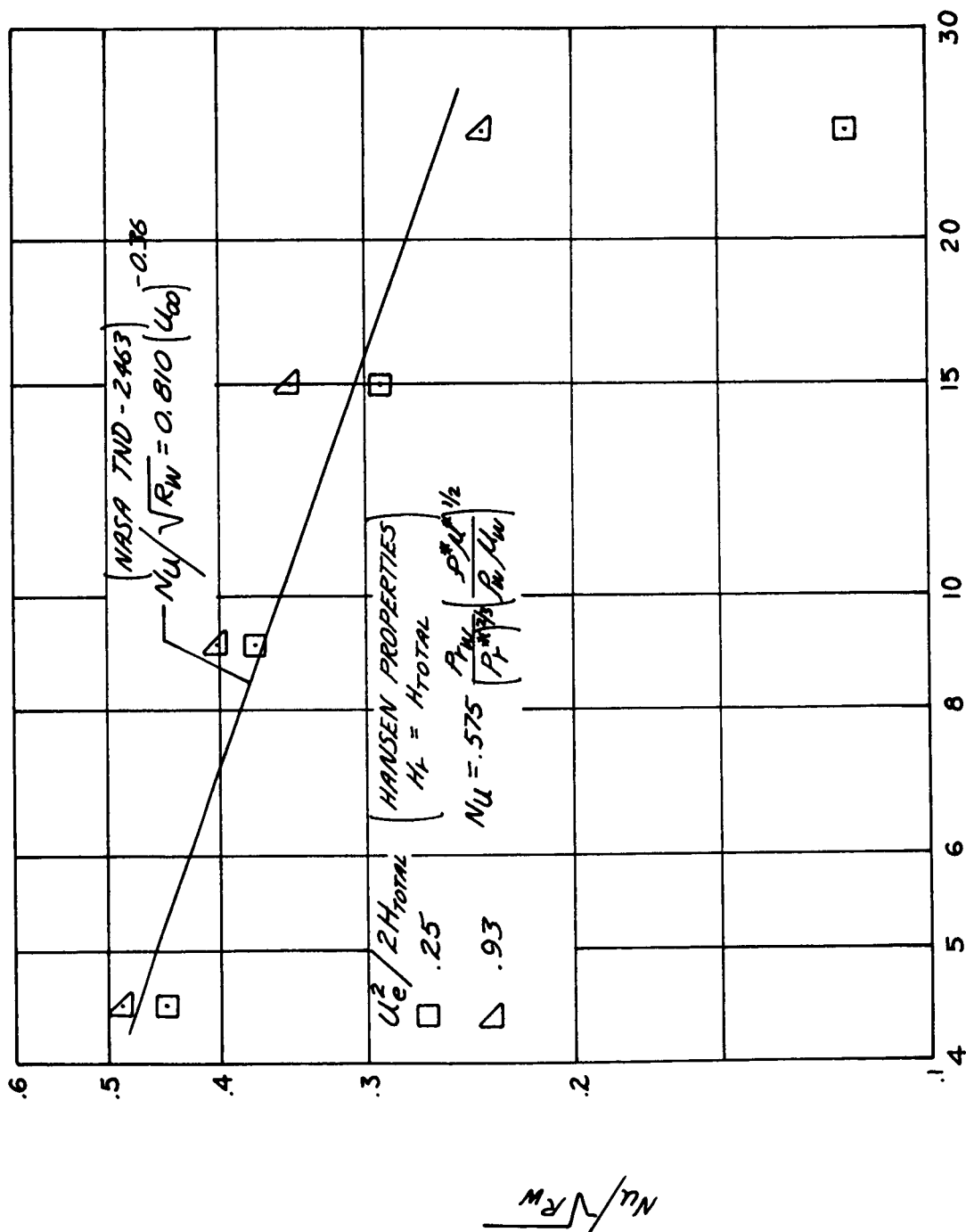
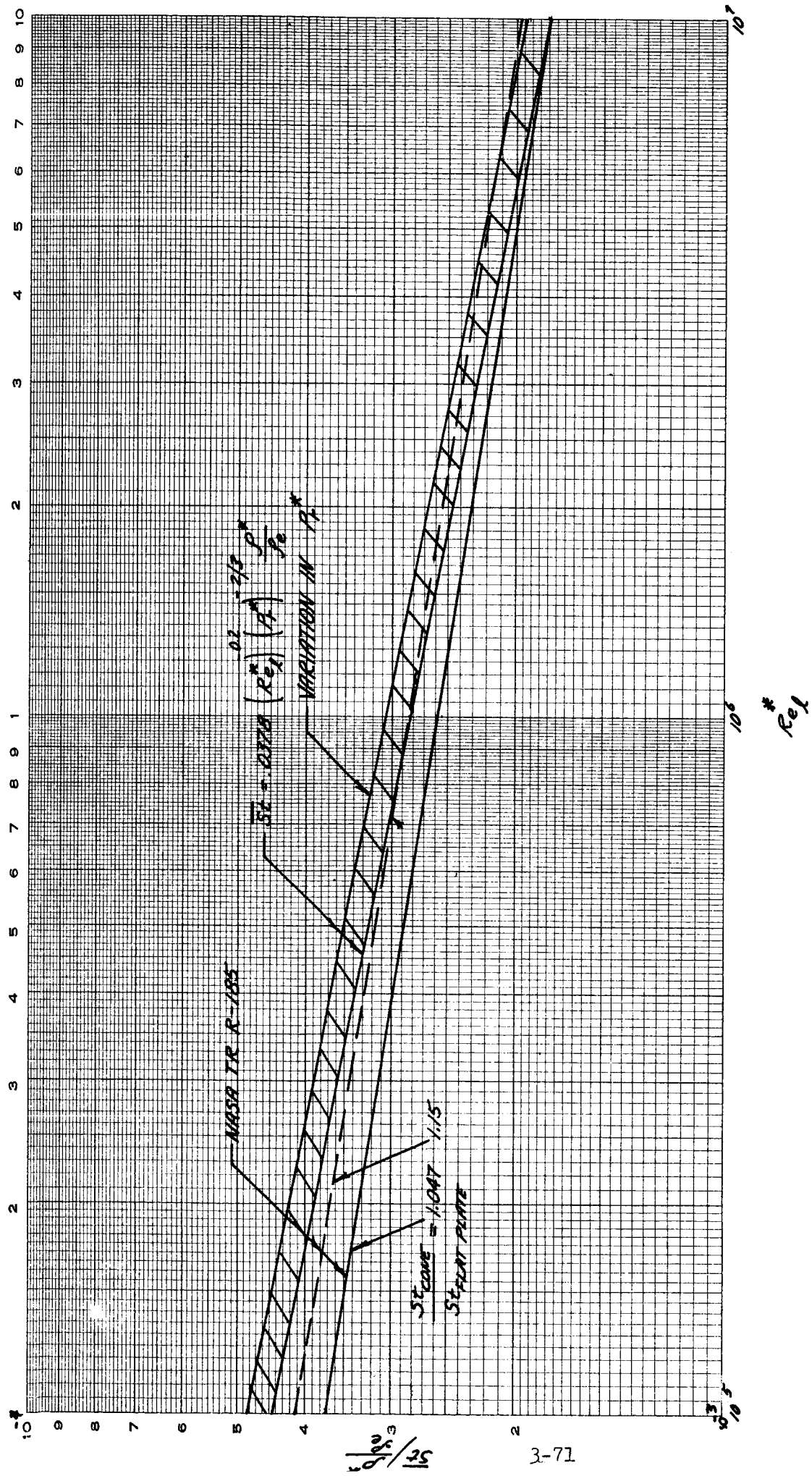


FIGURE 3-25
LAMINAR HEAT TRANSFER TO SHARP CONES



FREE-STREAM VELOCITY, U_∞ , km/sec
 $P_e = 1 \text{ ATM}$, $T_w = 3000^\circ \text{K}$

FIGURE 3-26



Section 4

CONCLUSIONS AND RECOMMENDATIONS

Thermal protection requirements for entry into the Earth's atmosphere at superorbital speeds have been examined for two lifting vehicles of the bi-conic configuration class. Behaviour of the heat shielding material has been theoretically described and performance predictions sufficient for experimental qualification of the theoretical model have been provided.

Study results have direct application in analysis of Mars mission feasibility. Furthermore, they enable identification of problems for future research.

4.1 CONCLUSIONS

During the course of the study, consideration has been given to vehicle flight mechanics, high-temperature-gas properties, heat transfer phenomena, and heat shield material behaviour. The final report of work conducted during the preceding phases of this study contains a comprehensive description of fundamental analysis procedures and basic data. In that work, shielding requirements were determined for several vehicle configurations for a broad variety of entry situations and a thorough investigation of uncertainties was conducted. During the current effort, analysis techniques have been refined, further basic data computations have been made, and two additional vehicle geometries have been treated. The new results provide further insight to the relative importance of environmental phenomena, vehicle parameters, and mission constraints on heat shielding requirements. They do not alter the previously reported conclusions.

Heat Transfer Analyses

For the slender cone configurations examined during this phase of the study, convection is by far the predominant mode of heat transfers. Radiation remains unimportant even at the maximum velocity considered, 65,000 ft/sec. Because trajectory pullout is generally achieved in the altitude range where boundary layer turbulence may occur, the predicted convective heat load is highly sensitive to the assumed transition criterion. Laminar flow prevails at an assumed critical Reynolds number of 5×10^6 whereas the boundary layer is turbulent over most of the surface regardless of entry condition for a critical Reynolds of 2×10^5 .

The extent of blunting of the initially sharp nose during entry is relatively small. Consequently, the entropy layer, which arises from bow shock curvature and which leads to reduced convection and increased radiation, is thin. This layer is rapidly entrained within the boundary layer and hence heat transfer levels over most of the forebody surface are not appreciably perturbed from sharp cone values.

Materials Performance

A theoretical model for prediction of the thermochemical performance of charring materials has been reviewed and the approximations introduced in its application have been delineated. The influence of the major assumption that pyrolysis-gas/air reactions do not occur within the boundary layer has been examined. It was shown that the assumption yields maximum ablation rates, but minimum surface temperatures. The opposite limit assumption of complete chemical equilibrium yields erosion rates about 30 percent less and surface temperatures about 20 percent greater.

The influence of environmental conditions on material behaviour has been demonstrated by exercising the theoretical model for selected test conditions. High enthalpy, low convective coefficient environments result in development

of relatively thick char layers. As the convection coefficient is increased, quasi-steady ablation conditions are approached, the rate of surface recession varies in essentially linear fashion with the convection coefficient, and the char thickness is reduced. The efficient performance of nylon phenolic is due in large measure to the high energy absorption by gaseous pyrolysis products.

Comparison of experimental data on ablation performance with the predictions substantiates the validity of the general thermochemical performance model. The two limit assumptions on the kinetics of pyrolysis-gas/air reactions yield results which bracket the data. The number of comparisons and detail of the data was not sufficient to enable positive identification of the superior kinetics model.

Vehicle Heat Shielding Requirements

Heat shielding for the two biconic configurations will comprise a significant fraction of total vehicle weight. With a conservative boundary layer transition criterion, the shield weight fraction varies from about 0.25 at an entry velocity of 36,000 ft/sec to about 0.6 at 65,000 ft/sec. When an optimistic criterion is employed, the weight fraction ranges from about 0.12 to 0.3 dependent upon entry condition.

Position within the entry corridor appreciable influences shielding requirements. Weight is generally minimized by entry in the undershoot trajectory as a consequence of the relatively short heating period. In the overshoot trajectory, shield weight varies slowly and almost linearly with entry velocity. This weak dependence is attributable to the lack of significant radiation and to the increased effectiveness of transpiration in reducing the convective heating at higher entry velocities.

Of the two vehicles considered, the higher lift (26 deg cone half angle) configuration requires the greater heat shielding. This is due primarily to

the increased entry time which results with increase in lift to drag ratio. In comparison with the vehicles previously studied, the two biconic configurations are intermediate to the Ames M1 and Ames M2 configurations. The results thus indicate that relatively blunt configurations remain attractive at high entry velocities.

4.2 RECOMMENDATIONS

General

- o Apply results of this study in preliminary analysis of and planning for a manned mission to Mars
- o Study the effects of geometry variables on overall system weight to establish optimum vehicle configurations
- o Investigate the influence of altitude maneuvering and lift modulation to establish optimum trajectories
- o Determine the influence of lift to drag ratio on mission effectiveness considering weight penalty and maneuverability benefits

Heat Transfer Analyses

- o Experimentally investigate the transition phenomena simulating flight conditions of surface roughness, mass injection, wall cooling, and local Mach number
- o Study the influence of the boundary layer on radiative heat transfer accounting for the presence of ablation products
- o Develop engineering analysis procedures for realistic evaluation of base region heat transfer considering both convection and wake

radiation

Heat Shielding Materials

- o Conduct experimental and/or theoretical program to describe kinetics of the relevant chemical reactions and to determine their importance on gross performance
- o Determine the environmental regimes where mechanical erosion of char will occur and develop suitable relations for predicting extent of such erosion